Perturbing Spanwise Modes in Turbulent Boundary Layers

A THESIS
SUBMITTED TO THE FACULTY OF THE GRADUATE SCHOOL
OF THE UNIVERSITY OF MINNESOTA
BY

Shaokai Zheng

IN PARTIAL FULFILLMENT OF THE REQUIREMENTS
FOR THE DEGREE OF
MASTER OF SCIENCE

Ellen K. Longmire, Adviser

January 2013

Acknowledgements

I had a great time working towards this thesis, and its completion, more importantly all the things I have learned about research, would not have been possible without the help of several people. First of all, I would like to thank my adviser, Dr. Ellen Longmire, for taking me as a student and keeping me on track throughout my graduate study. She helped me immensely diagnose problems, edit this thesis and prepare for the final presentation; I am truly grateful to have had the opportunity to work with her. Dr. Qi Gao and Mitch Ryan introduced me to the lab facilities in the beginning of my study; especially Mitch, he taught me how to run and maintain the water channel. Deepak Adhikari and Ankur Bordoloi helped me in learning the data processing procedures and they were always willing to discuss any questions with me. Also, I would like to thank my friends in the AEM department at University of Minnesota, Juan Valencia, Savio James, Karthik Reddy to name a few. Finally, I thank my mom for the love and all that she has done for me; I would not have come so far without her.

Last but not least, the author acknowledges the support from the National Science Foundation through grant CBET-0933341

Abstract

The objective of the current study was to manipulate the coherent vortex packets in a turbulent boundary layer at $Re_\tau = 2480$ by inserting a small scale cylinder array and to improve the understanding of the downstream flow stability issues. The height of the cylinders was $H/\delta = 0.2$ ($H^+ = 500$) with aspect ratio (AR=cylinder height/base diameter) of 4, and three cases were studied using single array of 0.2δ, 0.4δ and 0.6δ spaced cylinders. Both fixed location data and flying data were acquired at $z^+ = 296$ using PIV, and the spanwise scales of the packets and the wake-packet interactions downstream of the cylinder array were also discussed.

The non-perturbed flow was studied first and the dominant spanwise scale of the vortex packets was found to be $\sim 0.6\delta$. From the flying data, the organization of vortex packets was found to persist over a streamwise distance of $\sim 8\delta$. The averaged results of the perturbed cases showed a spanwise variation of the streamwise velocity downstream of the cylinder array, and the spanwise scales of the low speed regions were most stable for the 0.6δ spacing case. Also, distinct downwash behavior was observed directly behind each cylinder. The flying data showed frequent spanwise interactions of cylinder wakes in the 0.2δ case and the downstream structures were affected greatly by the incoming flow condition. The 0.4δ and 0.6δ cases were discussed based on the relative spanwise location of the upstream vortex packets and the cylinders and it was concluded that the organization of flow structures was most stable when the perturbation scale was the same as the dominant spanwise mode of the non-perturbed flow.

Table of Contents

List of Tables

List of Figures

Chapter 1

Introduction

1.1 Motivation

Wall-bounded turbulent boundary layers occur in many environmental and industrial applications, and many previous studies of wall-bounded turbulent flow have shown the existence of coherent vortical structures in the boundary layer that aligned roughly in the streamwise direction. Since these packets are believed to be a key self-sustaining mechanism, it may be possible to control boundary layer behavior by manipulating these coherent structures, leading to practical results such as affecting the skin friction and reducing drag for various kinds of transportation vehicles.

1.2 Previous studies

1.2.1 Vortex packets

Many previous studies of wall-bounded turbulent flow have shown that, instead of being totally chaotic, there are coherent vortical structures in the boundary layer. These vortices or eddies are often characterized as hairpin or horseshoe vortices due to their arch-like shape. The interest of these structures dates back to Theodorsen (1952) and their existence was supported by many later studies both experimentally and numerically (Head & Bandyopadhyay, 1981; Robinson, 1991a, 1991b; Adrian, Meinhart & Tomkins, 2000; Adrian & Liu, 2002; Adrian, 2007). A single hairpin vortex is usually considered as a vortex tube that extends away from the wall, curves at the top and then extends back toward the wall again. Typically, the dominant hairpins are leaning forward toward the mean flow direction. Based on this model, ejections, or ‘Q2’ events (positive wall normal velocity fluctuations $w > 0$ and negative streamwise velocity fluctuations $u < 0$), can be induced by the hairpin legs and head, consequently a slow moving region of fluid is formed through the inclined loop of the hairpin. The feature of Q2 ejection was

further confirmed by many, wherein Adrian, Meinhart & Tomkins (2000) used PIV to measure the streamwise wall-normal velocity field of a turbulent boundary layer at $Re_\theta = 6845$ and in the region below $z/\delta = 0.1,\ z^+ = 200$ (z being the distance away from wall), they found a pattern of strong second-quadrant vectors occurring on a locus inclined at roughly $45°$ to the wall which corresponds to the inclination of the hairpin vortices.

Further studies have shown that these hairpins often appear in groups aligned in the streamwise direction, referred to as 'packets', and the individual hairpins in the packet propagate with nearly equal velocities. The velocity dispersion was reported to be 7% by Adrian, Meinhart & Tomkins (2000), such that the relative spacing and arrangement of hairpins can remain coherent within a packet and last for a long time. This behavior was also observed by Tomkins & Adrian (2003), where they used PIV to look at the streamwise-spanwise plane of a turbulent boundary layer at $z/\delta = 0.045,\ z^+ = 100$ with $Re_\theta = 7705$ and they found clear patterns of roughly streamwise-aligned vortices, verified by plotting the swirling strength λ_{ci} (Zhou, 1999). These patterns lasted throughout the streamwise extent of the field which was 2.25δ. Ganapathisubramani et al. (2003) also observed groups of legs of hairpin vortices in the log layer ($z^+ = 92$ and $z^+ = 150$) coherently arranged in the streamwise direction, as they measured the streamwise-spanwise plane of a boundary layer at $Re_\tau = 1060$. These regions were also found to generate substantial Reynolds stress through Q2 events and the spatial organization into packets was seen to break down beyond the log layer ($z/\delta = 0.2$ and $z/\delta = 0.5$, or $z^+ = 198$ and $z^+ = 530$ respectively). Adrian (2007) serves as a more complete review of vortex organization in boundary layers.

While previous experimental work was limited to planar measurements, Elsinga et al. (2007) used tomographic-PIV to look at the coherent structures in a turbulent boundary layer at $Re_\tau = 818$. They looked at the logarithmic layer where asymmetric hairpin vortices were predominant, and hairpin packets containing $2 \sim 4$ streamwise-aligned vortices (over a streamwise range up to approximately 0.8δ) were found to occur frequently. They also concluded that multiple hairpin packets or vortices aligned in wall-normal direction contribute the most to the Reynolds shear stress production through Q2 events, which is the same as predicted by Adrian, Meinhart & Tomkins (2000). Another recent measurement was done by Dennis & Nickels (2011a) at $Re_\theta = 4700$, who used high speed stereoscopic-PIV coupled with Taylor's hypothesis to yield the 'quasi-instantaneous' volumetric velocity field. They found that the hairpin vortices in a packet scale with their distance from the wall. Also, for conditional averaged results based on a single swirling event, a single vortex was found to straddle a long low-speed region of fluid surrounded by high-speed regions on both sides lasting approximately 3δ, which was believed as signature of a packet. All of their analysis was based on the hairpin vortex-packet model of the boundary layer.

1.2.2 Long low momentum regions

With the vortex-packet model, a topic of increasing interest, long slow moving regions of fluid in the streamwise direction have been studied and analyzed by many investigators in this framework. These long regions of low u-momentum have been observed frequently. Jiménez (1998) first reported eddies with streamwise length of $10\delta\sim20\delta$ being present in the log region of wall-bounded flows. Kim & Adrian (1999) observed long regions of streamwise velocity fluctuation in turbulent pipe flow over a range of different Reynolds numbers and they referred to these regions as VLSM (very large scale motions).

Tomkins & Adrian (2003) studied these low-momentum regions (LMRs) at different heights in the log layer ($z^+ = 100,\ 220,\ 330$ and 440 respectively) at $Re_\tau = 426$ and $Re_\tau = 2227$ respectively, and they found that at $z^+ = 440$, the LMRs were more uniform, and fewer small scale regions were present; while at $z^+ = 100$, the continuity of the LMRs was reduced as more small scale regions were observed. At $Re_\tau = 2227$, at each height they studied throughout the log region, LMRs were found consistently associated with swirling or vortical motions aligned in the streamwise direction and three types of idealized vortex merging scenarios were proposed to explain the merging and splitting of the LMRs. These merging mechanisms were confirmed by looking at the velocity vector fields (with swirling strength) where two vortex signatures were found immediately upstream of the merging point in many examples for both high and low Reynolds number cases.

Marusic & Hutchins (2007) used PIV, hot-wire and sonic anemometry in three different facilities with $Re_\tau = 1000,\ 14000$ and 6×10^5. Based on their results recovered by Taylor's hypothesis, two-point correlation statistics at a given height were found consistent at all Reynolds numbers, and these correlation maps agreed with very large scale features in the log region, referred to as 'superstructures'. They also presented DNS data to show that these superstructures have a significant interaction with the near wall region as well, seeming to modulate the small scale events at the wall. Such conclusions were also confirmed by Hutchins & Marusic (2007). They also reported that the length of these superstructures extended over 20δ and their dimensions in length scaled with the boundary layer thickness, or they are Reynolds number dependent, such that they become increasingly large as the Reynolds number increases. A meandering behavior of these superstructures was also observed and they proposed that the spanwise meandering was to some degree restricted 'in certain internal geometries'.

Recent works done by Gao (2011) implemented tomographic-PIV to look at the turbulent channel flow at $Re_\tau = 2480,\ z^+ = 47\sim400$. In his thesis, 3D evidence of merging and breaking of the LMRs was presented using a unique measurement method referred to as flying

tomographic-PIV (FTPIV), where certain regions of fluid were tracked as they evolved downstream. The slow moving structures were reported to last over 15.5δ at maximum with a spanwise meandering within the scale of 0.12δ in some FTPIV cases. Meanwhile, Dennis & Nickels (2011b) used high speed stereoscopic-PIV combined with Taylor's hypothesis to look at three-dimensional structures in the boundary layer at $Re_\theta = 4700$. In their study, the long structures were mostly found below $z/\delta = 0.5$, or $z^+ = 1230$ (although clear patterns of elongated low speed regions were visible only at $z/\delta = 0.15$, or $z^+ = 370$) and their length was estimated as predominantly $2\sim3\delta$, corresponding to the large scale motions observed by Balakumar & Adrian (2007). Also, they further concluded that about 97% of all structures were found to be less than 7δ in length, which was interesting as it contradicted those aforementioned studies where the length of these long structures was reported to be over 20δ. They interpreted that the superstructures consisted of multiple long structures aligning in the streamwise direction and confirmed by the correlation of streamwise velocity fluctuations, being of order of 5δ and strong only over 2δ. Lee & Sung (2011) further confirmed such mechanism by performing DNS of a turbulent boundary layer of various Reynolds number in the range $Re_\theta = 570\sim2560$. They concluded that the VLSMs had a statistical streamwise coherence of the order of $\sim6\delta$ in the log layer and the linear stochastic estimation results demonstrated the coherent alignment of vortex packets in the streamwise direction that formed the VSLMs.

Although the streamwise signature and length scales of these LMRs have been studied fairly extensively, works considering the spanwise features of these structures are limited. Two aspects are of most interest, i.e. the spanwise scale of the slow structures themselves and the spanwise spacing between them. Some of the early studies are reviewed in Tomkins & Adrian (2003); they also concluded, according to their experiments, that the typical spanwise scales for these structures themselves are $0.1\delta\sim0.4\delta$ and the scales grow with distance from the wall.

Hutchins et al. (2005) studied the spanwise periodicity of these long structures at $Re_\tau = 1100$ and by looking at the Fourier modes of the spanwise trace of streamwise velocity fluctuations at $z^+ = 150$, they found that the most probable spanwise spacing of these structures was approximately 0.6δ. They also used these Fourier modes to sort their PIV data and they found that those fields showing spanwise modes within $0.5 < \lambda_y/\delta < 0.75$ contained 93% of the total energy. Elsinga et al. (2010) performed experiments in a high-Reynolds-number supersonic turbulent boundary layer at $Re_\tau = 34000$. Analysis of their instantaneous volumetric PIV fields for $0.15 < z/\delta < 0.47$ showed that the width of the slow regions varied between 0.25δ and 0.4δ while spanwise spacing between them ranged from 0.5δ and 1δ.

Gao (2011) proposed that the spanwise scales of these slow moving structures, based on aforementioned FTPIV measurements, to be $0.16\delta\sim0.2\delta$ at $z^+ = 200$ and $0.26\delta\sim0.3\delta$ at $z^+ = 400$ for $Re_\tau = 1770\sim2480$; while for fixed tomographic-PIV measurements at

$Re_\tau = 2480$, the scales were found to be 0.1δ~0.14δ at $z^+ = 200$. Also, he proposed that the spanwise spacing of these structures were larger than 0.5δ since the long slow regions rarely occurred in pairs within a single volume with spanwise scale of 0.6δ, in either fixed tomographic-PIV or FTPIV which was consistent with Elsinga et al. (2010).

1.2.3 Perturbing the boundary layer using small scale obstacles

The current investigation will focus on examining the stability of the spanwise scales of these low speed regions by inserting obstacles into a fully developed smooth wall turbulent boundary layer. Studies have shown that these small scale obstacles have profound effects on the downstream flow conditions and structures. Corke et al. (1981) studied the effects of wall parallel plates inserted in the boundary layer of $Re_\theta = 3500$ at several heights, ranging over $H/\delta = 0.1$~0.8, or $H^+ = 140$~1280. Their smoke visualization results showed an effect of the downstream structure, i.e. a lack of large scale turbulence and a redistribution of fine scales, to persist for at least 25δ. Jacobi & McKeon (2011) studied the effects of wall mounted two-dimensional bars of $H^+ = 54$, extended for about 15δ with separation of $\sim 0.4\delta$, referred to as impulse or perturbation and based on their results they suggested the ability of small perturbations to affect large downstream regions of flow with a direct impact on the vortex structure. Although various kinds of obstacles have been used to study the effects they have on the downstream structure in a boundary layer, e.g. Schofield & Logan (1988), Wark et al. (1990) and Simpson (2001), cylinders are chosen for the current investigation in order to compare with works done by Ryan (2011) and many other recent works that used cylinder as obstacle.

It is clear that the downstream structure of a wall-mounted finite cylinder is complicated, but generally they are grouped into three major parts, i.e. tip vortices generated by the shear layer present at the free end; Kármán vortices along most of the height, comparable to those generated by 2D cylinder wake; and horseshoe vortex system near the base of the cylinder. Baker (1980) studied the horseshoe vortex formed around the base of a cylinder, with $AR = 7.5$ and the Reynolds number was in the range of $4 \times 10^3 < Re_D < 9 \times 10^4$. Pressure measurements of the symmetry plane upstream of a cylinder showed that distance of horseshoe vortex from cylinder centre decreased as D/δ increased, although the position variation was not obvious with different Reynolds number. Williamson (1996) serves as a complete review of works done regarding vortex dynamics in the 2D cylinder wake.

Tomkins (2001) investigated the downstream structures of the flow over hemispheres and single cylinder with $AR < 2$ ($AR = H/D$, defined as the aspect ratio where H is the cylinder height and D is the cylinder diameter), $H/\delta = 0.05$~0.15, or $H^+ = 100$~340, fully immersed in the log region of a turbulent boundary layer of $Re_\theta = 7700$. Based on the results

he concluded that the wall-mounted elements might consistently introduce structures into a fully turbulent boundary layer and the scale of these structures might be controlled by the individual element size or the scaling between each one of them. The author also observed greater number of strong vortices downstream of the hemisphere than that of the cylinder with maximum swirling strength near the mid-height in both cases.

Park et al. (2002) studied the flow structure around a single finite circular cylinder ($AR = 6$, $H/\delta = 0.85$) embedded in a simulated atmospheric boundary layer of $Re_D = 2 \times 10^4$. They concluded that the flow structure over a finite cylinder was greatly different from that of a 2D cylinder. The approaching flow moves upward and accelerates, then separates from the cylinder circumference at the free end; the separated shear layer then descends along the central section of the wake creating a downwash. A counter-rotating vortex pair was observed near the free end at the same time. They also concluded that, in the lower wake region below half of the cylinder height, the vortices shed from both sides of the cylinder are not greatly influenced by the downwash.

Sumner et al. (2004) investigated the wake of a finite circular cylinder of small aspect ratio mounted normal to a ground plane extending across a turbulent boundary layer of $Re_D = 6 \times 10^4$. The aforementioned counter-rotating vortex pair near the free end was observed for all aspect ratios, namely $AR = 3,\ 5,\ 7$ and 9, but base vortex structure was only found for $AR = 5,\ 7$ and 9 cases. The Kármán vortex shedding was reported to be absent for $AR = 3$ and the cylinder wake was dominated by the downwash from the tip, suppressing both the horseshoe and Kármán-type vortices. Dillion-Gibbons et al. (2007) investigated interaction of a turbulent boundary layer with a wall-mounted cylinder that extended beyond the free surface. Reynolds numbers based on free stream velocity were $Re_D = 3600$ and 5400, with cylinder aspect ratio of $AR = 18.9$. The authors observed a downward motion within a distance downstream of the cylinder depending on Reynolds number, i.e. $x/D = 1$ (corresponding to $x/\delta = 5$) for $Re_D = 5400$ and $x/D = 1{\sim}1.5$ ($x/\delta = 5{\sim}7.6$) for $Re_D = 3600$.

Park & Lee (2003) studied the structures around two finite cylinders inserted in atmospheric boundary layer of $Re_D = 2 \times 10^4$. Two finite cylinders with the same aspect ratio of $AR = 6$ with $H/\delta = 0.85$ were used and gap ratio (G/D=center-to-center distance/cylinder diameter) in the range of 1.0-2.0 were investigated. The wake structure was found asymmetric when the two cylinders are in contact ($G/D = 1.0$) because the two cylinders behave as a single bluff body. When the gap ratio was increased to $G/D > 1.25$, the flow passing through the gap between the two cylinders was biased toward each cylinder alternatively and interact with the wake. At the largest gap ratio of $G/D = 2.0$, the flow exhibited a quasi-symmetric in-phase shedding pattern without direct interaction between the two inner shear layers of the wakes behind each cylinder. Since the measurement was limited to the upper half of the cylinder height, no characteristics of

base vortex was observed.

Pujals et al. (2010) studied the large scale coherent structures induced by inserting a single array of cylinders into the boundary layer at $Re_\tau = 370$. The cylinder height was $H/\delta = 0.8$ for all cases, and the gap ratio $G/D = 4$ was maintained while several cases with different cylinder diameter and spacing were examined. Based on their observations of the streamwise velocity downstream of the cylinder array, strong spanwise variations were observed. The amplitude of these variations in different cases were compared, and it was concluded that the streamwise development of the amplitude would be the same for a constant gap ratio under proper scaling, indicating that the development of the downstream flow structures were highly dependent on the gap ratio of the cylinder array.

Ryan et al. (2011) performed hot-wire measurements of flow behind a single array of wall mounted cylinders in a turbulent boundary layer. The height of the cylinders was chosen to be $H/\delta = 0.13$ $(H^+ = 150)$ such that they reached into the log layer but not beyond. The aspect ratio was $AR = 1.5$ and the Reynolds number was $Re_\tau = 1200$. Studies of single cylinder wake showed a local RMS peak value at $z^+ = 100$, which is 2/3 of the cylinder height. For the cylinder arrays with gap ratio of $G/D = 6$, wake interaction, a large mean velocity deficit at the midspacing location, was observed $12D$ (or 1δ) downstream of the cylinder array, while for $G/D = 3$, such interaction first occurred at $4D$, or 0.3δ downstream of the cylinder. Perturbations to the velocity profiles were not found to extend above the log region and the author suggested that neither tip vortex shedding nor Kármán vortex shedding played strong roles in the downstream flow evolution. However, the measurement was limited to 1.1δ downstream of the cylinder array. Following that, Ryan (2011) did experiments to look at the downstream effects of single cylinder array inserted in the boundary layer using stereoscopic-PIV (both fixed and flying, details can be found in Gao, 2011 and Ryan, 2011) and Volumetric Three-Component Velocimetry (V3V). Ryan (2011) used cylinders of $AR = 4$, $H/\delta = 0.2$, $(H^+ = 500)$, extending to the log region, and two cases of 0.2δ and 0.4δ spacing were studied. PIV measurement was taken at $H/\delta = 0.11$ $(H^+ = 296)$ and the Reynolds number was $Re_\tau = 2480$. The cylinder array produced a long-lasting effect on both mean and RMS velocity field that was stabilized with wake pairing, defined as large streamwise velocity deficit at the midspacing location. Such behavior occurred farther downstream for the larger spacing case. The low speed regions at the mid-spacing after the pairing were only slightly reduced in strength by $\sim 7\delta$ downstream of the cylinders in the 0.4δ spacing case. Also, the V3V data suggested that the effects did not extend above the log region, in consistent with the hot-wire data of Ryan et al. (2011). By looking at the instantaneous fields, the author concluded that the wake pairing of 0.4δ spacing (gap ratio $G/D = 8$) was more stable than the 0.2δ spacing $(G/D = 4)$ case. The downwash directly downstream of the cylinders was believed to

cause the split wake (defined as velocity deficit downstream of a cylinder at each side in the time averaged results) as it brings faster moving fluid toward the wall; on the contrary, there was an upwash at the mid-spacing spanwise location as it brings slower moving fluid away from the wall. The streamwise RMS velocity observed was highest at mid-spacing for the 0.4δ case, while for the 0.2δ case the highest RMS velocity pattern remained directly downstream of each cylinder. Furthermore, by computing the swirling strength λ_{ci}, it was confirmed that the low speed regions were accompanied by pairs of strong, counter rotating vortices.

1.3 Objectives and approach

Many questions have been answered for the effects a cylinder array (wall-mounted with tip extending into the log layer) have on the downstream structure in a fully turbulent layer. However, some questions remain.

Since the streamwise measurement scale was limited to 5δ downstream (Ryan 2011) of the cylinder array, it is not clear how the structures are organized further downstream. Besides, due to the quality of wall normal component of the velocity field, the scale of the downwash/upwash statistics are not obvious and no explanation was provided relating these behavior to the possible presence of vortex packets in the flow.

The instantaneous flying data was analyzed regarding the stability of the slow speed region, yet no quantitative results were given. Thus, the current investigation will repeat the 0.2δ and 0.4δ spacing cases (Ryan 2011) over longer streamwise distance up to 7.5δ downstream, and a wider spacing of 0.6δ case (gap ratio $G/D = 12$) will be investigated, following the previous conclusion that the downstream structure is more stable with bigger spacing. A Fourier analysis method will be introduced to quantitatively reveal the spacing between neighboring low speed regions downstream of the cylinder array and consequently determine the stability of the structure for each case. Post-processing will be performed to reduce error in the velocity field and experiment conditions will be improved as well. Furthermore, vortex structure identified by swirling strength as well as Reynolds stresses will be examined to provide further understanding of the downstream structure of the cylinder array using the vortex packet model. Explanations of the stability of downstream structures will be attempted. For the flying-PIV experiments, experimental procedure will be improved to acquire more organized runs of data; focus will then be given onto the low speed regions downstream of the cylinder array. Behavior of these slow moving regions will be compared with fixed data, and extra attention will be paid to explain the stability of the downstream flow structure.

Chapter 2

Experimental Apparatus and Methods

2.1 Water Channel

All experiments were conducted in a closed return water channel at University of Minnesota. The water is driven by an AC motor with adjustable input frequency in the range of $6\sim60Hz$. Before entering the working section, the water travels through a honey comb and three stainless steel screens. The working section is constructed of optical quality glass plates and is $8m$ long, $1.22m$ wide, with a free surface of $0.39m$ above the bottom wall for the current investigation. At the entrance of the working section, a stainless steel trip wire with a diameter of $3mm$ is glued on the surface of the bottom wall to stimulate the flow to turbulence. For all experiments conducted, the volume of water was maintained constant by setting the depth of water to $390mm$ at the entrance of working section when the motor was driven at $45Hz$.

A traverse system is built on top of the working section in order to track the vortical structures in the boundary layer. Two rails are laid on top of the side walls throughout the working section, as shown in Figure 2.1. A platform is installed across the working section above the rail and is used for holding the cameras. It is driven by two motors such that it can travel in the streamwise direction at speeds of up to $1m/s$ and the spanwise position can also be adjusted. An L-shaped suspension is mounted to the traverse to hold the laser sheet optics, shown in the left side of Figure 2.1. Two metal wires are installed on each side to reduce the oscillation of the suspension during traveling, especially during acceleration and deceleration of the traverse. With this optics holder, the laser sheet can travel simultaneously with the flow and the camera system. The entire traverse system is controlled through the Measurement & Automation Explorer of National Instruments.

In order to use Particle Image Velocimetry (PIV) from top of the channel, a glass interface box is installed below the traverse. The interface box has a flat, square bottom of area $0.61m^2$ and the bottom surface is submersed in the water by $15mm$. Laser Doppler Velocimetry (LDV) was used by Gao (2011) to characterize the turbulent boundary layer at various downstream

locations and water channel motor frequencies with and without the interface box. All experiments in the current investigation were conducted with the water channel motor set at $45Hz$. Table 2.1 is reproduced from Gao (2011).

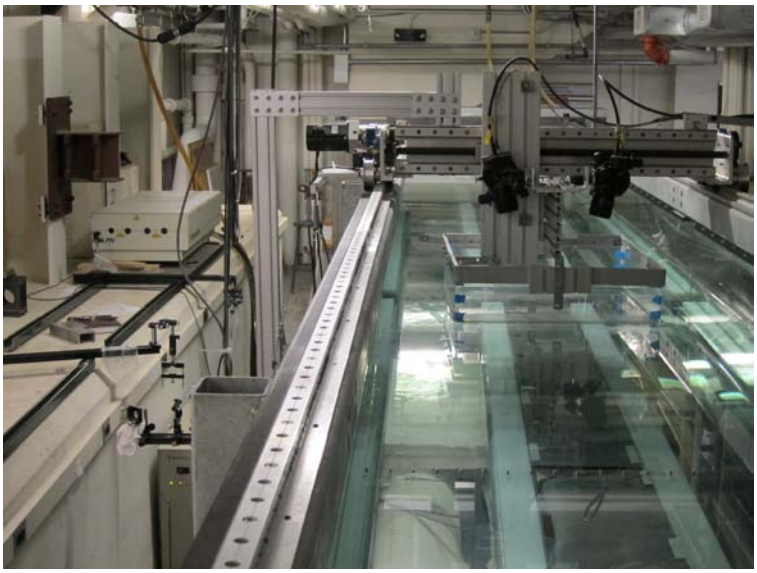

Figure 2. 1 Traverse system and experimental platform

Parameters	Symbols	With Box	Without Box
Streamwise Distance from Trip (m)	x_{trip}	6.12	6.12
Water Height (cm)	H_w	39	39
Freestream Velocity (m/s)	U_∞	0.508	0.485
Boundary Layer Thickness (mm)	δ	125.5	134.4
Skin Friction Velocity (m/s)	u_τ	0.0198	0.0180
Reynolds Number	Re_θ	6150	7050
Reynolds Number	Re_τ	2480	2410

Table 2. 1 Boundary layer parameters reproduced from Gao (2011)

2.2 Experimental Setup

A typical PIV system usually consists of several components, laser, optics, camera(s) and synchronizer. For the current investigation, a dual-head Spectra Physics Nd:YAG laser is used with output power of $370\ mJ/pulse$. A set of spherical lenses were used to make sure the laser beam diameter would not change throughout the test section. The optical layout is shown in Figure 2.2 a). One spherical lens and two cylindrical lenses were used to generate the laser sheet,

as shown in Figure 2.2 b), through the side wall of the water channel. Particles used for all experiments were silver coated hollow glass spheres manufactured by Potters Industries LLC, with a mean diameter of $16\mu m$ (diameter range of $6\sim25\mu m$). Two 12-bit TSI PowerView 4MP Plus cameras with a resolution of 2048×2048 pixels were used along with Nikon Micro-Nikkor $60mm$ lenses for particle imaging. Both cameras were equipped with a Scheimpflug adapter for quality imaging. A schematic of the experimental setup is given in Figure 2.3.

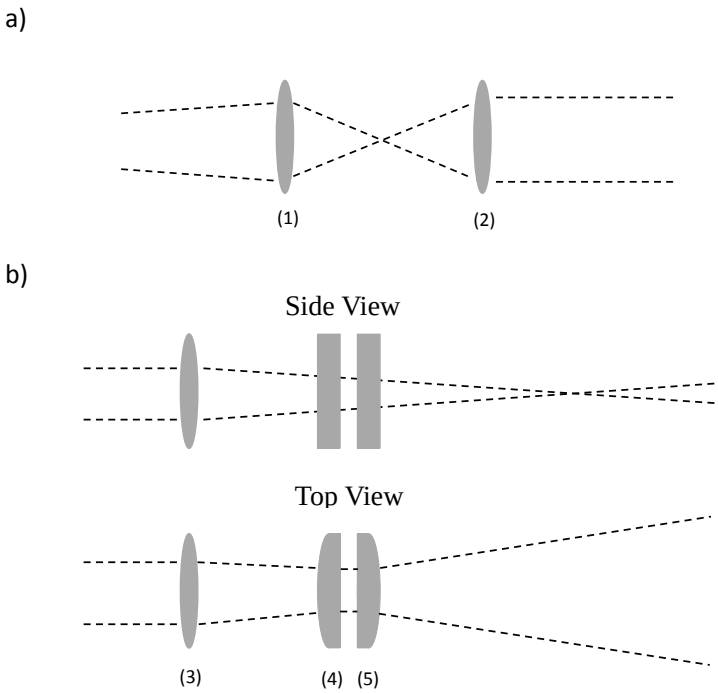

Figure 2. 2 Schematics of optic setup: a) laser beam optics, (1) and (2) spherical lenses with f=500mm; b) laser sheet optics, (3) spherical lens with f=1000mm, (4) and (5) cylindrical lenses with f=60mm.

In this study, a single spanwise array of prefabricated stainless steel smooth cylinders was used as perturbation. Each individual cylinder with height of $H = 25.4mm$ ($H^+ = 500$) and diameter of $D = 6.35mm$ (aspect ratio $AR = 4$) were mounted vertically on the bottom floor with 0.2δ, 0.4δ and 0.6δ (or $4D$, $8D$ and $12D$ respectively) spacing covering the entire span of the test section. Before each experiment, data was also collected without the cylinders. The cylinders were glued to the bottom floor of the water channel $5.88m$ downstream of the trip wire. The maximum blockage created by the cylinders (ratio of the frontal area of the cylinders to the cross-sectional area of the channel) was 1.7%. In the following discussions, the x, y and z axis are defined as the streamwise, spanwise and wall normal direction respectively, as shown in Figure 2.3.

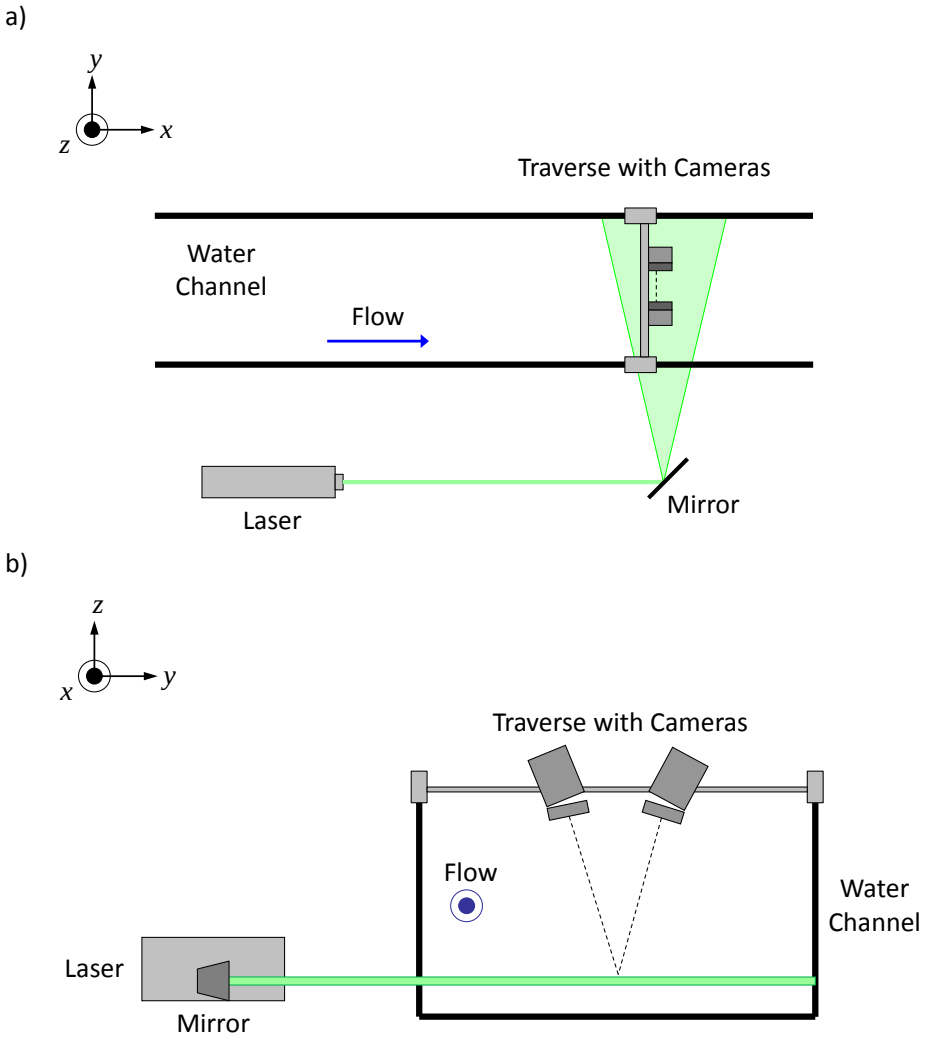

Figure 2. 3 Schematics of experimental setup (not to scale)

In current investigation, three types of experiments were conducted, namely fixed stereoscopic-PIV (SPIV), flying stereoscopic-PIV (FPIV) and fixed two side-by-side planar PIV (PPIV). For all experiments, data was taken from above the channel using the aforementioned interface box. The laser sheet at the center of the field of view (FOV) was $\sim 1mm$ thick and $15mm$ ($z^+ = 296$) above the wall. For SPIV experiments, each camera was angled approximately 20 degrees to the z axis. The FOV was approximately $1.1\delta \times 1.1\delta$. This arrangement is the same for FPIV experiments. For the PPIV experiments, two cameras were arranged side by side in the spanwise direction with minimum overlap covering a FOV of $1.1\delta \times 2.0\delta$ in x and y directions respectively, which is the same as two side-by-side 2D2C PIV system. This was arranged for the 0.6δ spacing experiment in that only two of the cylinders would show up in a SPIV set up and therefore the spanwise periodicity was poor,

which could affect the accuracy of the spanwise scale analysis discussed in the following section. Schematics of data fields captured are given in Figure 2.4 and 2.5. Note that for SPIV and PPIV, the final data field consists of five consecutive zones directly downstream of the cylinder array up to 4.6δ (referred to as zone 1 to 5 respectively along the streamwise direction) and a far field at $6.4\delta \sim 7.4\delta$ (referred to as zone 8); the size of each field in streamwise direction is 1δ except for zone 1, which ranges from $0 \sim 0.6\delta$. For FPIV, every third data field is plotted to avoid overlap, the size of each field in streamwise direction is also 1δ and the gap between two consecutive fields is $\sim 0.14\delta$.

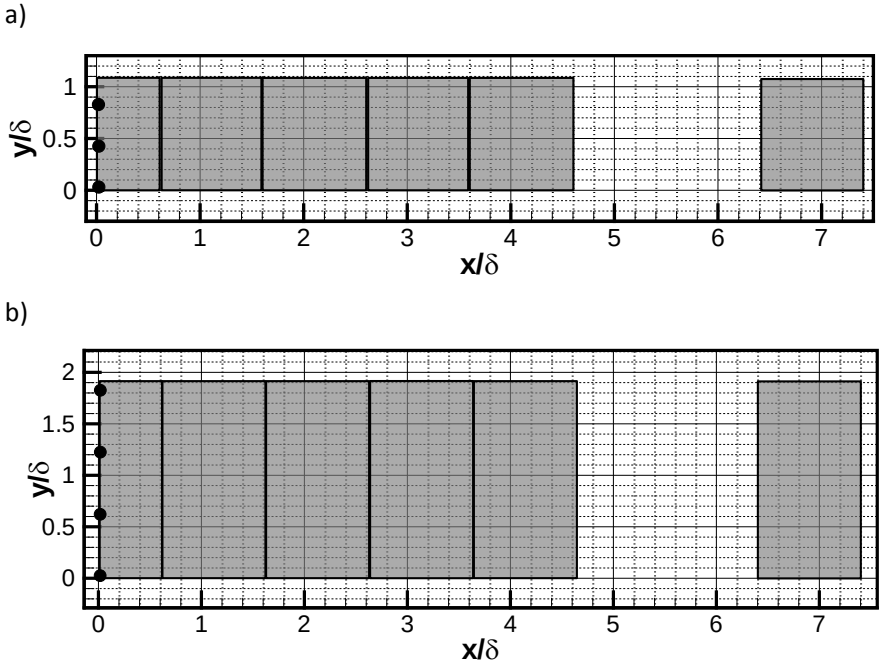

Figure 2. 4 Data field covered for a) SPIV, b) PPIV measurements, each field is distinguished by black edged boxes and referred to zone 1 ~ 5 and 8 respectively along the streamwise direction.

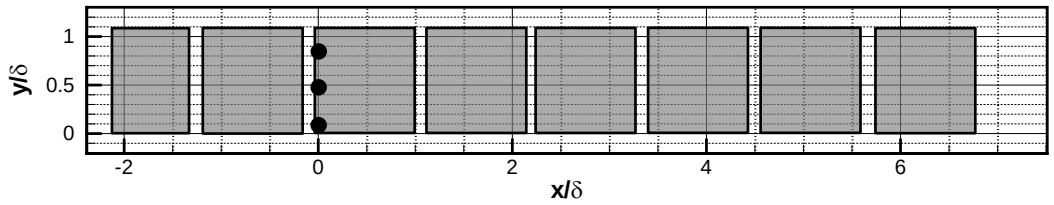

Figure 2. 5 Data field covered for FPIV measurements, each field is identified by black edged boxes. Only every third data field is plotted to avoid overlapping.

For SPIV experiments, a total of 1000 image pairs were collected at each zone with a sampling rate of $\sim 0.5Hz$. For PPIV experiments, data was taken in the same manner of that for

SPIV experiments. Note the FOV was two times bigger in the spanwise direction than that of SPIV measurements. For FPIV experiments, data was taken covering a streamwise range of $\sim 2\delta$ upstream of the cylinder and $\sim 7\delta$ downstream. The traverse speed was set based on the non-perturbed results and remained constant for all runs (the term non-perturbed is referred to as the measurement cases where no cylinders are mounted on the bottom floor). The speed selected was $0.37 m/s$ which is the mean streamwise velocity at the measurement plane $z^+ = 296$. The traverse was started far upstream to compensate for acceleration and velocity stabilization. Image pairs were captured with a sampling rate of $7.25 Hz$. An average number of 40 runs were taken for each case, as well as the non-perturbed case.

The current experimental system used two computers, one for PIV image acquisition (referred to as the acquisition computer) and the other for traverse system control (referred to as traverse computer). Two cameras are connected to the acquisition computer through a 64-bit Frame Grabber. The communication and data transmission were controlled by the acquisition computer using TSI software named Insight 3G. Two Berkeley Nucleonics BNC pulse generators were used to synchronize all components. The primary BNC box, model 500-A, was the signal source. It has four output ports labeled as T1, T2, T3 and T4; and one input port for external trigger. All ports work at the same frequency. T1 and T3 port were set to send the trigger signal to F1 and F2 of the laser respectively. T2 was connected to the input port of the slave BNC box, model 500-C, so the slave BNC box was working in external triggering mode. The slave BNC box also has four output ports (S1-4), among which S1 and S3 ports were connected to trigger the laser Q-switches Q1 and Q2 respectively. Since it was working in external triggering mode, all output ports worked at the same frequency as the input signal which is T2. The S4 port was connected to the acquisition computer to trigger the cameras. Consequently, the entire system worked at the frequency of T2.

Note that for all FPIV experiments, the primary BNC box was also working in external triggering mode. A light sensor switch was used to give a gate signal to its external port to turn the primary BNC box on. The switch was designed that a zero voltage output would be given when the surrounding was lit and a high voltage given in dark. The sensing switch was mounted to the side wall of the water channel and a LED flashlight was mounted on the traverse platform to complete the process. The experiments were conducted in a dark room so the switch would give a high voltage at the beginning. When the traverse reached certain x-location with the LED flashlight, the sensing switch was triggered to give a voltage drop and that drop triggered the primary BNC box. Rest of the process remained the same as stated before. The traverse system was working independently and commands were given through the traverse computer manually.

Specific timing setup involves several parts. The laser was receiving triggers from T1 and T3 for F1 and F2 respectively while Q1 and Q2 were triggered by S1 and S2 respectively. The

time interval between F1 and Q1, as well as F2 and Q2, was the Q-switch delay, referred to as t_d. The output power of the laser is a function of this t_d and it was set to be $180\mu s$ for maximum output. The Δt was the time difference between two laser pulses and was the time interval for the particle displacements to be tracked. For SPIV and PPIV experiments, the time difference Δt was chosen to be $800\mu s$ and for FPIV experiments, this value was $1800\mu s$. Exposure time for cameras was set in Insight 3G. The first exposure lasted $300\mu s$. The second exposure started right after the first one and ended before the next period. Details of the synchronization are presented in Figure 2.6.

2.3 Calibration

The calibration plate used was a dual plane target with alignment mirror on the side as shown in Figure 2.7. The side mirror was used to ensure that the laser sheet was perfectly parallel to the surface. Since the mirror was mounted perpendicular to the target surface, the laser sheet would be reflected backward superposing the original sheet if it were parallel to the surface of the target. Same procedure was also checked at 7δ downstream to make sure that the laser sheet was consistent throughout the entire measurement area. Note that, for PPIV experiments, two cameras were arranged as two independent 2D2C planar PIV systems, so one calibration image was taken for each camera.

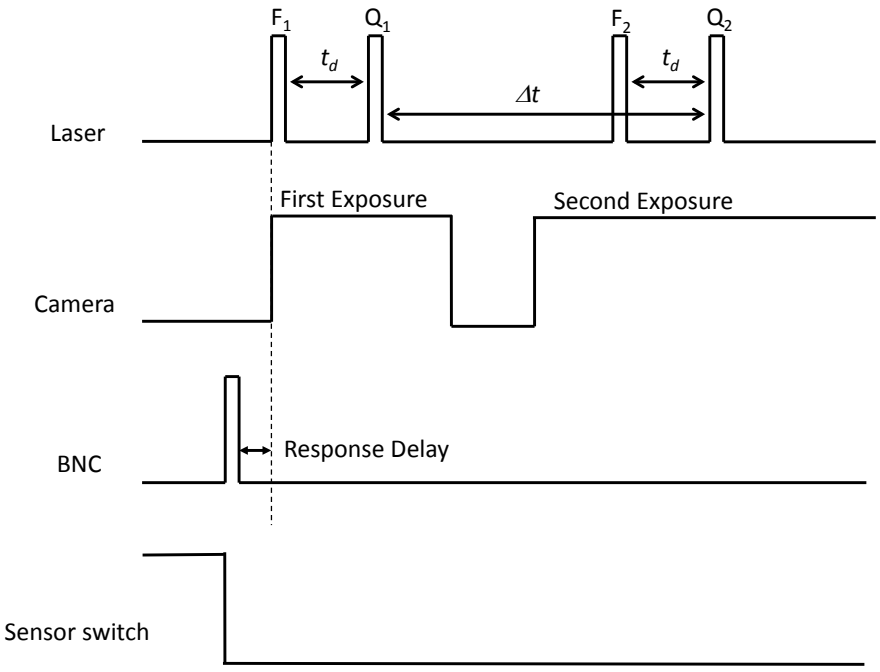

Figure 2. 6 Timing diagram for synchronization

Figure 2. 7 Dual plane calibration target

To reduce error in the data processing, special cares were given to the calibration procedure. Base on previous study, it was known that there was an interaction between the interface box and the free surface, such that the box would be tilted with the water running. Therefore, for the SPIV experiments, calibration image was taken with the water channel running at the same speed as during the experiments. Then, by using the DaVis software by LaVision, self calibration was also performed. The method was explained in detail by Wieneke (2005). For the FPIV experiments however, as the interface box was travelling, its interaction with the free surface was different than the fixed case. Since the box was controlled to travel at the speed of the mean streamwise velocity of the measurement plane, difference between the mean velocity and the free surface velocity was calculated, which was $0.138m/s$. Then, the water channel was running at $0.138m/s$ ($\sim 13Hz$) while the calibration plate image was taken for FPIV data sets. Self calibration was then performed using non-perturbed FPIV data. For PPIV experiments however, no self calibration was performed, because the calibration image for each camera was independent.

Note that there were compatibility issues between the acquisition software and the processing software so the calibration plate was rotated 45° when the calibration images were taken. Due to the size of the plate there were small gaps in the four corners of the calibration image and therefore the mapping function might have bigger errors in these areas.

2.4 Data Processing

For all SPIV and PPIV data sets, an interrogation window size of 32×32 pixels was used, with an overlap of 50%. Each resulting vector had a resolution of $l = 1.1mm$, $l^+ = 21$. For FPIV data sets, interrogation window size was chosen to be 64×64 pixels, with 50% overlap. The corresponding resolution was consequently $l = 2.3mm$, $l^+ = 45$. All vector field calculation was done in DaVis 7.4. To improve the data quality, several processes were required. First of all, the original particle image was enhanced using two options in DaVis, i.e. subtract sliding background and particle intensity normalization. The sliding background subtraction was

done to prevent intensity fluctuations in the background. It works like a high pass filter such that the large scale intensity fluctuations in the background may be filtered out while the small scale intensity fluctuations of the particle signal will pass through. The particle intensity normalization option performs a local particle intensity correction. As a result, homogeneous particle intensities were obtained which was helpful since the particle diameter was in the range of $6\sim25\mu m$ and their intensity was consequently inhomogeneous in the original image. Figure 2.8 gives an example for each operation where the original image is on top and the processed image at bottom.

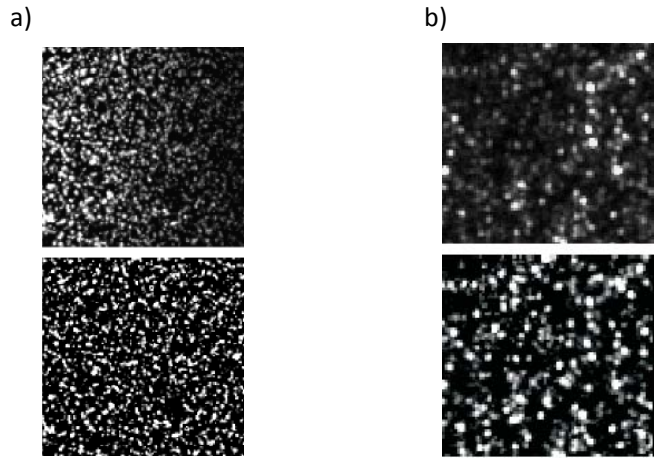

Figure 2. 8 Example for image preprocessing with original image on top and processed image at bottom: a) sliding background subtraction filter; b) particle intensity normalization

The median filter in DaVis was also used for all data processing. The median filter computes a median vector from the eight neighboring vectors and compares the middle vector with this median vector ± n*deviation of the neighboring vectors. The center vector is then rejected when it is outside the allowed range of the median vector ± n*deviation of the neighbor vectors. The factor n was chosen for each experiment by checking the bad vectors in each instantaneous vector field, but generally it was around $2.5\sim3$. All SPIV and PPIV data fields were output after processing and a filtering code (written in *MATLAB*) was applied to the data files eliminating those remaining bad vectors (usually along the edges) using the 3σ criterion, such that any vector lying outside the range of mean $\pm3\sigma$ was thrown away and was not counted toward the statistics. This was done for all three velocity components respectively. A PDF (probability density function) distribution of the streamwise velocity from non-perturbed case before and after this process is shown in Figure 2.9. The left one is the original PDF over 1000 fields and right one is the filtered result. Note the velocity is normalized by the free stream velocity U_∞. It is clear that in the left plot, some points are present far left of the main distribution, referred to as the outliers and in the right plot they are filtered out. After the filtering,

the statistical results, i.e. mean velocity and the standard deviation for all three components were returned to DaVis to set the limit for a global filtering operation. Those outlying data points were removed and interpolated. Finally, all fields were averaged to get the averaged and RMS velocity field. For the FPIV data, no such process was performed since they were all instantaneous fields.

Further, Gao (2011) examined the bottom floor of the water channel, and variations between the floor and the traverse was measured at different streamwise/spanwise locations. These variations are typically small but to the wall-normal component of the velocity field, they are big enough to introduce unphysical variations within a field of view. Since the laser sheet was calibrated carefully to be parallel with the traverse and the cameras are focused on the laser sheet. That is to say, the measurement plane is not at the same height due to the variation of the floor. Therefore, a rotation was performed on the final data based on the variations measured at the location of calibration to compensate the variation of wall-normal velocity introduced by the floor variations.

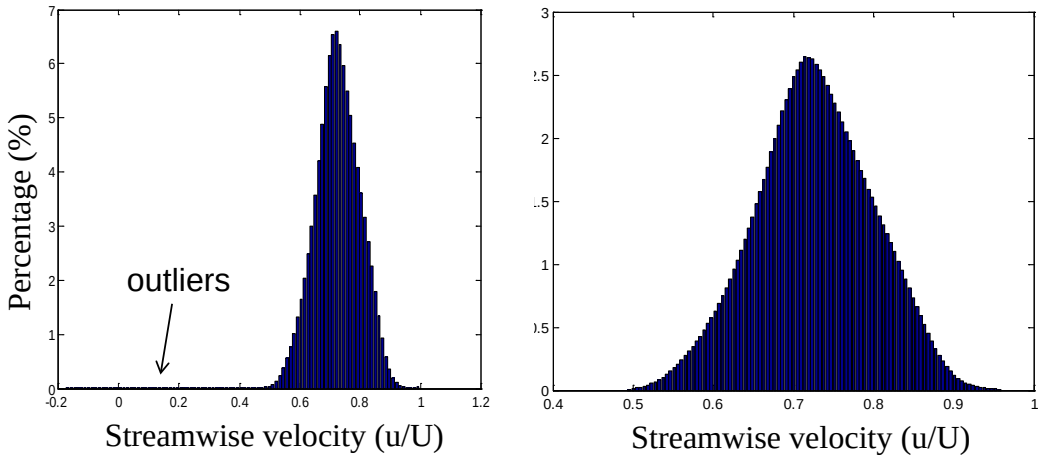

Figure 2. 9 Normalized streamwise velocity distribution before (left) and after filtering (right)

2.5 Fourier method for spanwise mode

For all data fields, the 2D swirling strength λ_{ci} was computed to identify vortical structures. It is defined as the imaginary part of the complex eigenvalues of the 2D velocity gradient tensor and is signed by the ω_z-vorticity. Also, the Reynolds stress was computed as uw, since we were most interested in the vortex packet signature which was believed to be associated with strong Q2 events, as discussed in the introduction. By looking at these two quantities of the flow field, the boundary layer structure can be analyzed and compared with previous works, and the wake structure of the cylinders can be better understood.

Another major effort in this paper is to quantitatively identify the spanwise spacing of the

long low momentum regions frequently reported in the log region of the boundary layer. The method was developed in $MATLAB$ using Fourier analysis and the following description in this section is based on non-perturbed SPIV data set unless stated otherwise. For each data field, the instantaneous streamwise velocity at certain x location was extracted together with the spanwise coordinates, as shown in Figure 2.10. Due to the resolution, there is always a maximum wave number that is resolvable. The wave number k is defined by $k = 2\pi/\lambda$, where λ is the wave length. So k_{max} is defined when λ is equal to the grid size $\Delta y \approx 1.1mm$ (the exact value is calculated for each data set). Based on the Nyquist-Shannon sampling theorem, only components smaller than $k_{max}/2 \approx 2800m^{-1}$ (also referred to as Nyquist limit) can be completely recovered, any components beyond that limit would contribute to the aliasing. Therefore, the fluctuation curve needs to be filtered before using FFT (Fast Fourier Transform) to find its dominant component. A low-pass filter was implemented here to eliminate higher wave number components. The curve of streamwise velocity fluctuation after the filtering is given in Figure 2.11.

By comparing Figure 2.10 b) and Figure 2.11, we can see that the original shape of the fluctuation curve is well preserved, although in some cases, the shortest wavelength fluctuations are slightly flattened due to the low pass filter. This is expected since the wavelength components within the transition band will suffer from the attenuation. To minimize this effect, the transition bandwidth is set to $10m^{-1}$, i.e. from $2790m^{-1}$ to $2800m^{-1}$; therefore, only fluctuations with $\lambda \leq 0.01\delta$ will likely be affected. This explains the minor difference between the unfiltered and filtered fluctuation curves.

a) b)

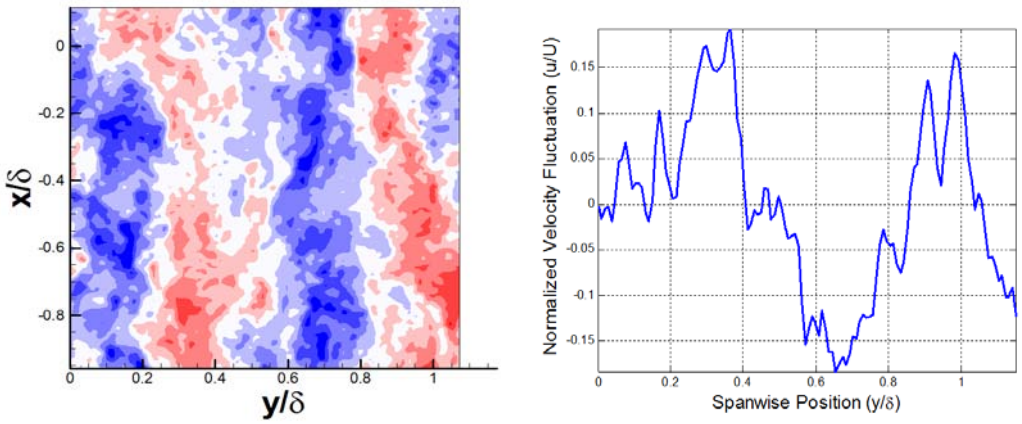

Figure 2. 10 a) Instantaneous streamwise velocity field; b) Streamwise velocity fluctuation.

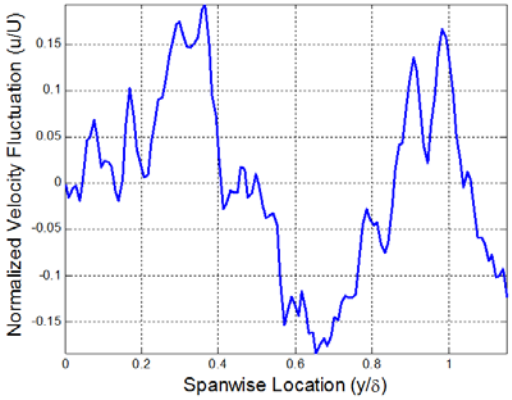

Figure 2. 11 Filtered streamwise velocity fluctuation

After the filtering, Fourier transform was applied to the fluctuation curve transforming it to the wave number domain. Since we are interested in the most dominant wave number (dominant spanwise spacing in wavelength domain), the component of maximum amplitude in the wave number domain (for each streamwise location in each field) is picked and then transformed back into the wavelength domain where the dominant wavelengths are grouped into bins to show the distribution, as shown in Figure 2.12.

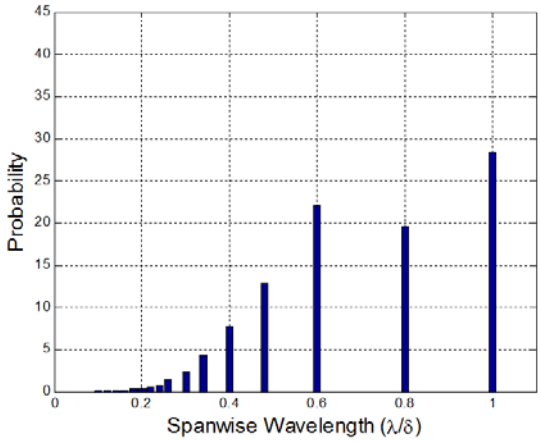

Figure 2. 12 Spanwise scale distribution using just Fourier transform

By looking at Figure 2.12 we can tell that it is not physical in that the distribution should be somewhat continuous and a close examination of the instantaneous fields reveals that the dominant spanwise scale should be $\sim 0.6\delta$. If we looked back, it is easy to find that there are two more issues to be addressed concerning the Fourier transform. The first one is that, due to the limited span of the FOV, there is a longest wavelength that can be resolved, consequently, a smallest wave number, be referred to as k_{min} (the value of k_{min} is typically $\sim 44m^{-1}$ for SPIV and $\sim 26m^{-1}$ for PPIV). This is obviously bigger than zero, so the wave number

components between 0 and k_{min} are not physical. The second issue lies in the figure. Note that even though the bins in the plot are evenly spaced, the resolution is getting poorer toward the longest wavelength. The reason is that in the wave number domain, the wave number axis is evenly spaced; but that corresponded to unevenly spaced real domain intervals. The closer it is to the origin at wave number domain, the poorer resolution is expected in the wavelength domain; this explains the huge gaps in Figure 2.12.

For the first issue, it is natural to cut the wave number components between 0 and k_{min}, meaning that to set the amplitude of those components to be 0, so that when the dominant component is picked, those components are guaranteed not to be chosen. Figure 2.13 gives the spectrum of non-perturbed SPIV and PPIV data set averaged over 1000 fields. The small wave number components are cut off, yet remind that the value of k_{min} is different for SPIV and PPIV, as mentioned previously.

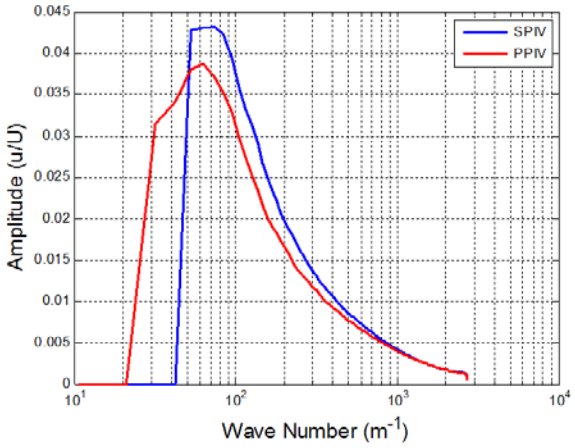

Figure 2. 13 Averaged spectrum of non-perturbed SPIV and PPIV data set

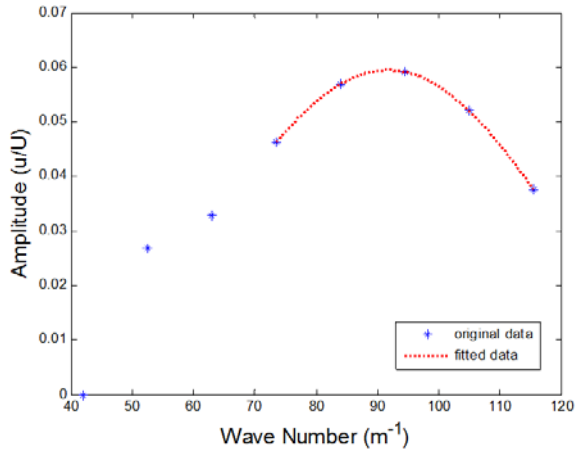

Figure 2. 14 Polynomial fit to find the exact maximum (showing only part of the spectrum)

To deal with the second issue, a curve fit in the wave number domain was performed. After we extracted the dominant amplitude component with the corresponding wave number, two data points before that and two after that were picked as well. Then these five data points were used for a polynomial curve fit (as shown in Figure 2.14) to find the wave number corresponding to the real maximum. In the case of Figure 2.14, the original maximum is $\sim 94.5m^{-1}$ and the fitted maximum is $\sim 91.8m^{-1}$; thus the dominant wave number component is better resolved and a more continuous distribution of spanwise scale is expected.

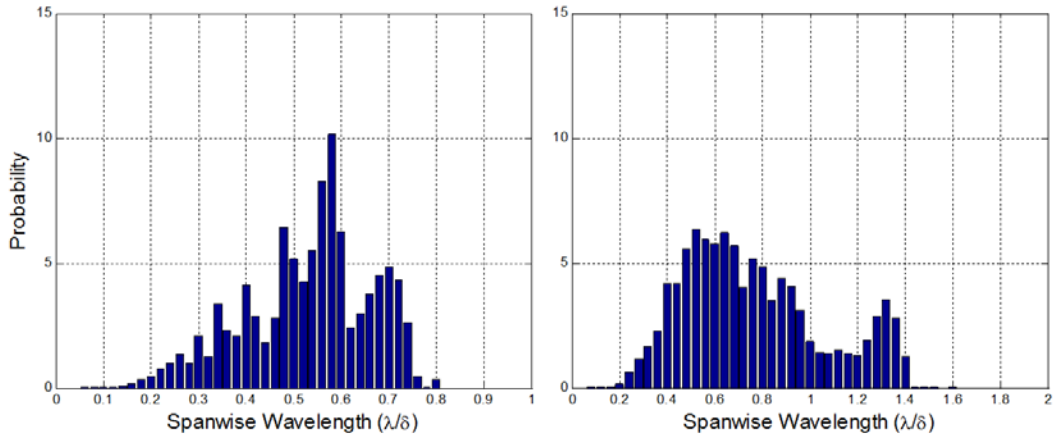

Figure 2. 15 Distribution of dominant spanwise scale of SPIV (left) and PPIV (right) using small bin size

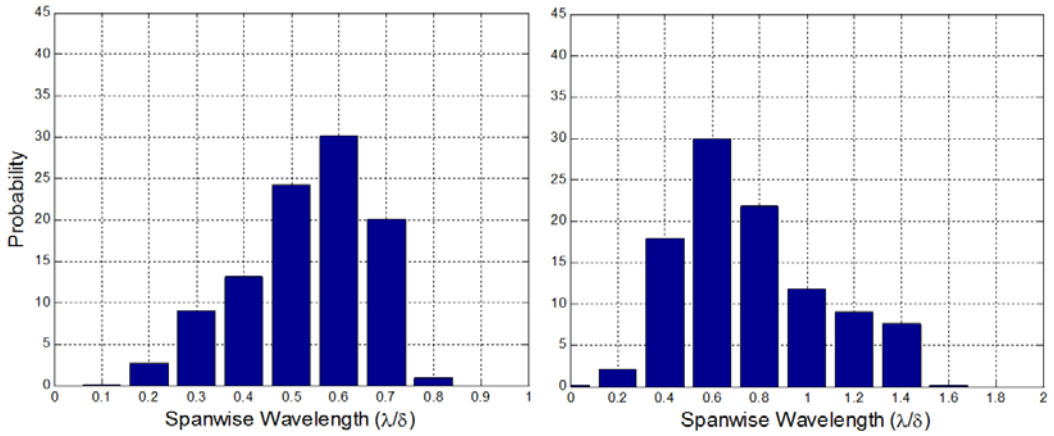

Figure 2. 16 Distribution of dominant spanwise scale of SPIV (left) and PPIV (right) using bin size of 1/10 of span

Figure 2.15 gives the spanwise scale distribution of both non-perturbed SPIV and PPIV data after implementing both the wave number cut off and the curve fitting. It is more continuous than that in Figure 2.12; however, the spikes and pits seen in Figure 2.15 (left) and the spike at $\sim 1.3\delta$ in Figure 2.15 (right) are not physical. This suggests that the curve fitting helps to recover the

real distribution, but due to the original resolution, some unphysical distribution will remain if the bin width is sufficiently small. In order to compensate the poor resolution toward the longest wavelength, we chose $1/10$ of the total span as the bin size to show the trend of the distribution without losing useful information. Final results are given in Figure 2.16. Under the chosen bin size for each case, smaller wavelength components are also grouped together so that the resolution will be the same throughout the span. Now the distribution is more physical in that the dominant mode is $\sim 0.6\delta$ while the smaller and bigger wavelength components are both decaying naturally without secondary peak.

2.6 Experimental Uncertainty

Measurement uncertainty can be introduced in several ways. Gao (2011) reported $\sim 2\%$ error of the traverse speed. This can be critical in that the particle images were taken through the interface box which was connected to the traverse, so that the tilting angle of the box could be different if the traverse speed changed during experiment. In previous experiments done in this water channel, significant error of the wall-normal velocity component was observed, especially for FPIV data. For the current investigation, two improvements have been made to prevent that. First, the rails that the traverse ran on were cleaned and lubricated, as well as the motor shafts for the traverse system. Secondly, the connection between the interface box and the traverse was reinforced so the vibration was greatly reduced. Also, upstream flow condition itself can introduce significant amount of error into the data; so extra care was taken towards the honey comb, the screens and the floor condition in order to ensure spanwise uniformity in the non-perturbed flow.

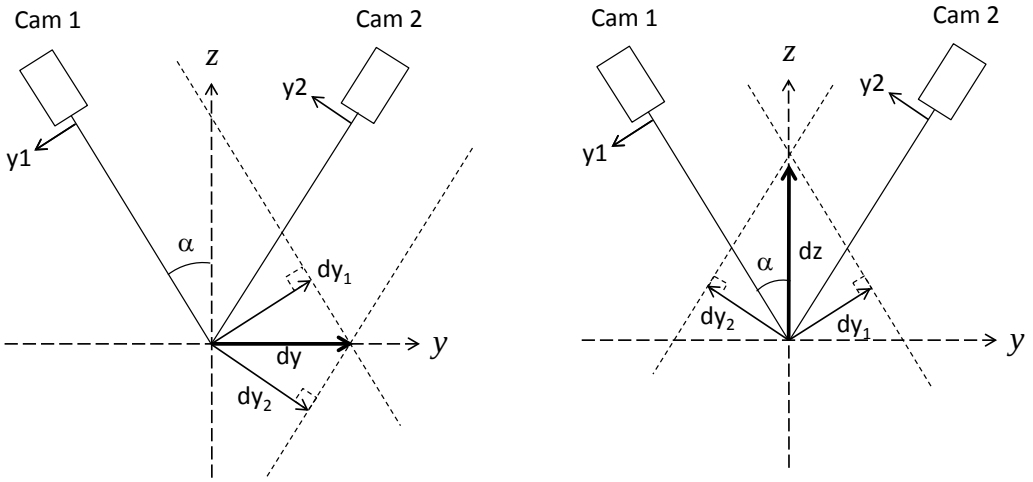

Figure 2. 17 Geometry for current SPIV set up

Another part of uncertainty comes from the reconstruction of the vector fields and is determined by the reconstruction method based on the geometry of the PIV set up. Prasad (2000) gives an overview of different Stereoscopic PIV systems and equations used to calculate the 3-component vector field using two 2-component fields. In all figures and equations the real displacement (dx, dy and dz) are linear functions of the displacements seen by camera 1 (dx_1, dy_1) and those seen by camera 2 (dx_2, dy_2). The geometry for current SPIV setup is given in Figure 2.17 and the corresponding reconstruction method is given by Equation (1) and (2),

$$\begin{cases} \mathrm{d}y_1 = -\mathrm{d}y * cos\alpha - \mathrm{d}z * sin\alpha \\ \mathrm{d}y_2 = -\mathrm{d}y * cos\alpha + \mathrm{d}z * sin\alpha \\ \mathrm{d}x_1 = \mathrm{d}x; \quad \mathrm{d}x_2 = \mathrm{d}x \end{cases} \tag{1}$$

$$\begin{cases} \mathrm{d}x = \frac{\mathrm{d}x_1 + \mathrm{d}x_2}{2} \\ \mathrm{d}y = \frac{-\mathrm{d}y_1 - \mathrm{d}y_2}{2*cos\alpha} = \frac{-\mathrm{d}y_1 - \mathrm{d}y_2}{\sqrt{3}} \\ \mathrm{d}z = \frac{-\mathrm{d}y_1 + \mathrm{d}y_2}{2*sin\alpha} = -\mathrm{d}y_1 + \mathrm{d}y_2 \end{cases} \Rightarrow \begin{cases} \sigma_{dx} = \frac{\sigma_0}{\sqrt{2}} \\ \sigma_{dy} = \frac{\sqrt{2}}{\sqrt{3}}\sigma_0 \\ \sigma_{dz} = \sqrt{2}\sigma_0 \end{cases} \tag{2}$$

where α is the angle between the camera and the z axis and it is $\sim 30^{\circ}$ for the current setup. For this setup, dx can be measured by each camera independently so it is expected that σ_{dx} is the smallest. Ideally, if we had $\alpha = 45^{\circ}$, it can be shown that $\sigma_{dx} = \sigma_{dz} = \sigma_0$ (Doorne, 2003); however, in this case the angle α is limited by the experimental platform so it is expected that we have a bigger σ_{dz}. As the reconstruction uncertainty σ_0 for 2C PIV is typically $0.1px$ (Westerweel et al. 1997), based on the rule of uncertainty propagation, we find $\sigma_{dx} = 0.07px$, $\sigma_{dy} = 0.08px$, and $\sigma_{dz} = 0.14px$ for a given instantaneous vector. For reference, the averaged particle displacement between two frames is $\sim 8px$ for $U = 0.37m/s$ at measurement height, referred to as P_U. After normalization, we have the relative correlation error as $\sigma_{dx} = 0.0088P_U$, $\sigma_{dy} = 0.01P_U$ and $\sigma_{dz} = 0.0175P_U$ respectively.

To further evaluate the accuracy of the current study, the statistical uncertainties of mean velocity and RMS velocity are calculated. Equation (3) is used to calculate the uncertainty in mean velocity for streamwise, spanwise and wall normal component respectively.

$$\sigma_{U,V,W} = \pm \frac{1.96S}{\sqrt{N}} \tag{3}$$

S is the standard deviation and the independent measurement number N is estimated to be $N = 1000$. The final estimated uncertainty of mean velocity is $\sigma_U = \pm 0.0063U$, $\sigma_V =$

$\pm 0.0041U$, and $\sigma_W = \pm 0.0074U$ for a 95% confidence interval, where $U = 0.37m/s$ is the streamwise mean velocity at measurement height.

For the RMS velocity, uncertainties are estimated using

$$\frac{(N-1)S^2}{\chi^2_{\nu,\alpha/2}} \leq \sigma^2{}_{u,v,w} \leq \frac{(N-1)S^2}{\chi^2_{\nu,1-\alpha/2}} \tag{4}$$

where S is the standard deviation, N is the number of measurements i.e. $N = 1000$; χ^2 denotes the Chi-Squared distribution, ν is the number of degrees of freedom ($\nu = N - 1 = 999$) and α is the level of significance ($\alpha = 0.025$ for a 95% confidence interval). By calculating the mean and the estimated interval for standard deviation, the mean statistics of RMS velocity can be summarized as $U_{RMS}/U = 0.1016 \pm 0.0046$, $V_{RMS}/U = 0.0657 \pm 0.0030$ and $W_{RMS}/U = 0.1197 \pm 0.0055$.

That the w-component has the largest uncertainty both in mean and RMS velocity is not surprising, since it is the component calculated using the in-plane components. Experiments of the non-perturbed case showed an improvement of data quality compared with Ryan (2011) and free stream velocity statistics were compared with DNS data. These results will be discussed in the following chapter.

Chapter 3

Results and Discussion: Averaged Results

In this chapter, the averaged results are discussed. All data sets used are listed in Table 3.1; each set consists of 1000 image pairs. First of all, the mean flow statistics of non-perturbed and perturbed cases will be presented to show the measurement quality and the pattern of the downstream structure; then the spanwise scales of each data set will be discussed in terms of the stability of low momentum regions observed downstream of the cylinder array. The freestream velocity U_∞ and the boundary layer thickness δ are used for normalization throughout the rest of the following discussion.

	Data set name	Cylinder spacing	Measurement type
Fixed	NOCS	∞ (no cylinder)	SPIV
	NOCP	∞ (no cylinder)	PPIV
	S4D	0.2δ	SPIV
	S8D	0.4δ	SPIV
	S12D	0.6δ	SPIV
	P12D	0.6δ	PPIV
Flying	FNOC	∞ (no cylinder)	FPIV
	F4D	0.2δ	FPIV
	F8D	0.4δ	FPIV
	F12D	0.6δ	FPIV

Table 3. 1 List of data sets used in current study

3.1 Non-perturbed flow

In this part the mean flow statistics are presented using the NOCS and NOCP data sets.

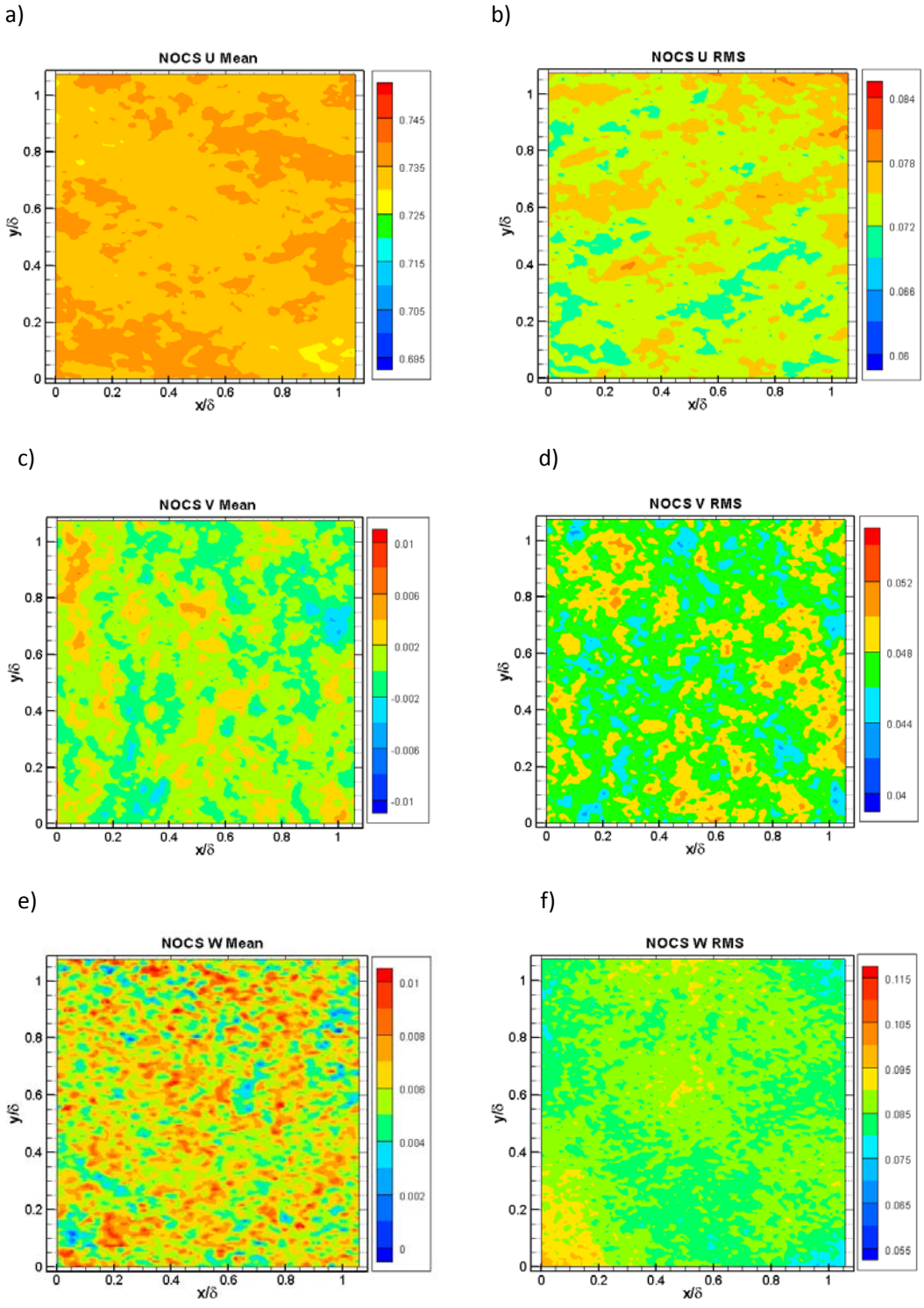

Figure 3. 1 Mean and RMS velocity contour maps for NOCS

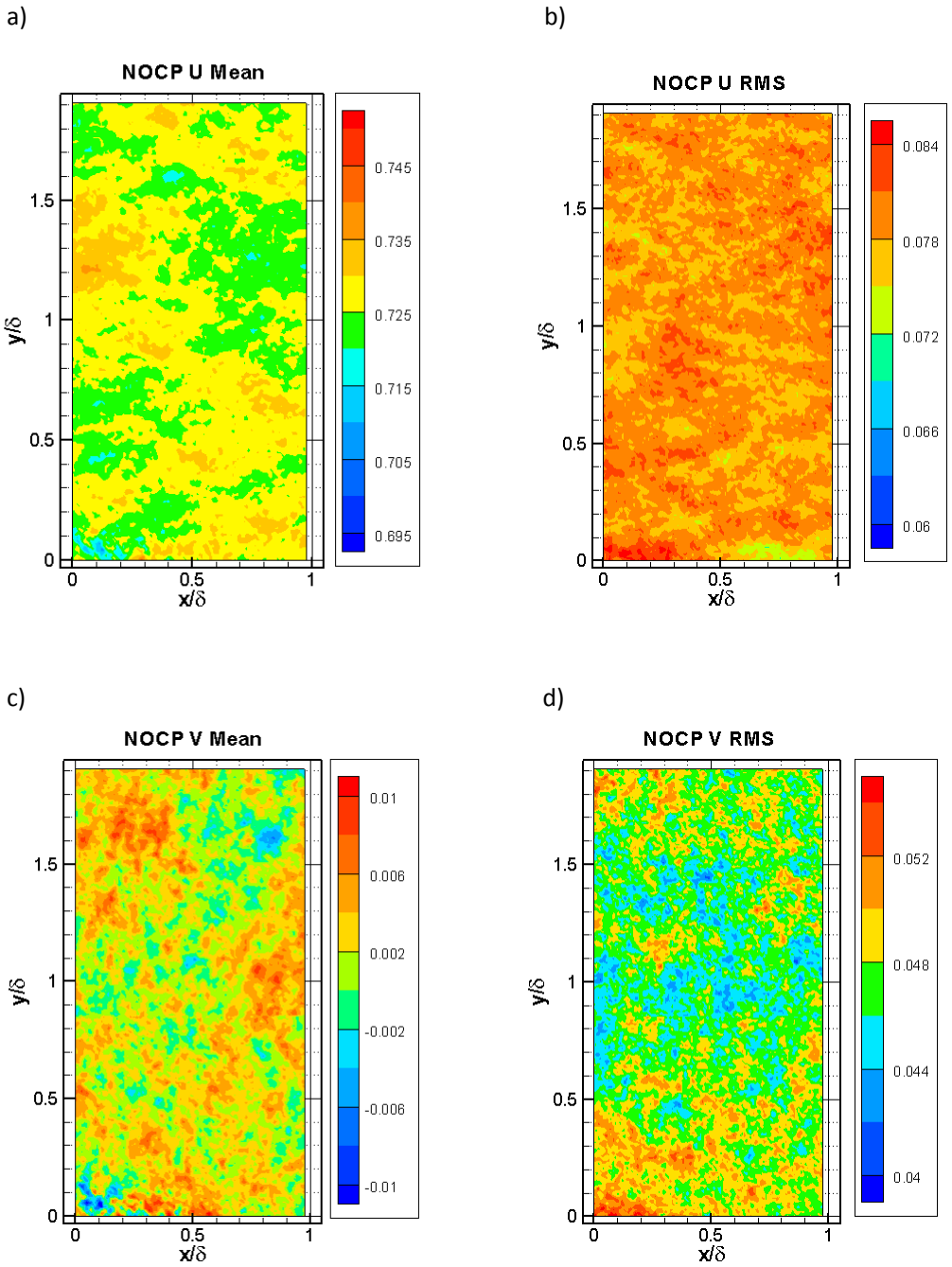

Figure 3. 2 Mean and RMS velocity contour maps for NOCP

Mean velocity and RMS velocity contour maps for NOCS are shown in Figure 3.1, and those for NOCP are given in Figure 3.2. From the mean velocity contour maps, we can see a variation of $\sim 1.5\%$, $\sim 0.8\%$ and $\sim 1\%$ in U, V and W components respectively for the NOCS case. These values are typically bigger than the estimated uncertainty calculated in Chapter 2 using $N = 1000$, especially the streamwise component. This is due to the existence of the long lasting low-momentum regions (LMRs) such that it is captured in two or more consecutive images making the velocity fields correlated, so the actual number of independent measurement N would be less than 1000. Since the LMRs are aligned in the streamwise direction the strongest correlation and consequently the biggest difference is expected in this direction, as demonstrated in this case. For NOCP case, the variation in U and V component is $\sim 2\%$ and $\sim 1.2\%$ respectively, this is greater than that of the stereo case in that the in-plane velocity components are calculated using one camera, so a bigger reconstruction uncertainty, namely $0.1px$, is expected, leading to a higher uncertainty level in velocity.

For the RMS figures, one thing to notice is the corners of wall normal component of RMS velocity contour for NOCS where the largest deviation is observed. This might be caused by the incompatibility of the calibration plate and processing software (see Chapter 2). Also, since the wall normal component is most sensitive and calculated from the in-plane components, the error is accumulated and observed in Figure 3.1 f).

		Current study		DNS
		NOCS	NOCP	
Reynolds number (Re_τ)		2480	2480	2003
Measurement height (z^+)		296	296	294
Mean velocity (Normalized by U_∞)	U/U_∞	72.48%	72.63%	69.31%
	V/U_∞	0.19%	0.23%	--
	W/U_∞	0.61%	--	--
Mean RMS velocity (Normalized by U_∞)	U_{RMS}/U_∞	7.39%	7.87%	8.27%
	V_{RMS}/U_∞	4.74%	4.77%	4.42%
	W_{RMS}/U_∞	8.57%	--	5.38%

Table 3. 2 Mean and RMS statistics compared with DNS data (Hoyas and Jimenez, 2006)

From Figure 3.2 it is observed that the bottom left corner in each of the figures has the biggest deviation from the mean value and it is most obvious in the RMS fields. This might be

caused by the laser sheet in that the sheet is slightly directed towards the downstream direction to avoid blockage and the bottom left corner is close to both the sheet optics and the edge of the sheet, so the laser intensity in that area is weaker than the rest of the field. Consequently, a bigger calculation error is observed. Also, the laser sheet is fully focused at $y/\delta\sim1$ so the thickness is maximized at the top and bottom edge, which might introduce some error in the particle correlation process.

From Table 3.2 it is observed that the wall normal component of RMS bears the most difference when compared with DNS data of turbulent channel flow. This is not surprising considering uncertainty discussion in Chapter 2.

3.2 Perturbed flow

In this section, the mean flow structure will be discussed using the perturbed cases, i.e. with cylinder array mounted on the channel floor at $x/\delta = 0$. Three cases of cylinder spacing of 0.2δ, 0.4δ and 0.6δ respectively are studied. Note that for the 0.6δ spacing case, P12D is used for streamwise and spanwise velocity component discussion and S12D is used just for wall normal component discussion.

The contour maps for streamwise velocity are given in Figure 3.3 for all three cases (0.2δ, 0.4δ and 0.6δ). These figures show a clear pattern of splitting and/or merging signatures of the cylinder wake, i.e. two neighboring cylinder wake merge into one low speed region in the mid-spacing location. The word "split" and "merge" used for the averaged fields are limited to the description of the patterns of low speed regions observed downstream of the cylinders, whether there are actual splitting or merging signatures are not clear as yet and will be examined using the flying data.

For the 0.2δ spacing case, the merging of cylinder wake happens within $x/\delta\sim0.5$ downstream of the cylinder array and new LMRs are formed in the mid-spacing location after the merging with a spanwise spacing of 0.2δ. These LMRs stay stabilized and last up to $x/\delta\sim2$ before they disappear. Within this region ($x/\delta = 0.6\sim2$) these new LMRs remain coherent and stay parallel to each other, suggesting no strong spanwise interactions. At $x/\delta\sim2$, there seems to be a weak secondary merging observed at $y/\delta\sim0.5$, and the reformed LMR last until $\sim4\delta$ downstream. This suggests the existence of some weak spanwise interactions occur around $x/\delta\sim2$. Also, the streamwise velocity of the entire field keeps increasing after $x/\delta\sim2$ and goes up to $0.68U_\infty$ in the far field ($x/\delta\sim7$), which is smaller than the non-perturbed case ($0.73U_\infty$) but no pattern can be observed, suggesting that the perturbation scale introduced by the cylinders is no longer correlated with the cylinder location.

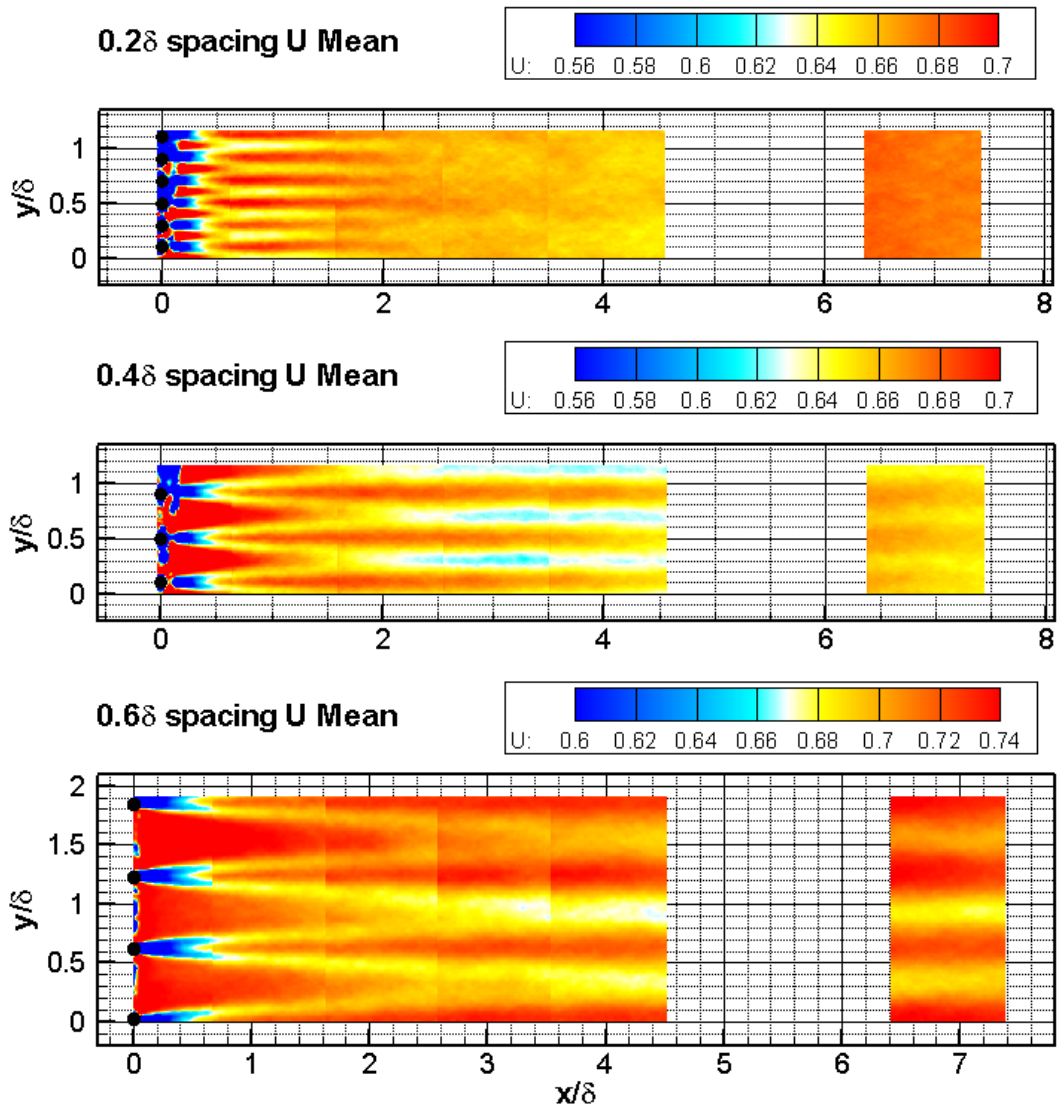

Figure 3. 3 Averaged streamwise velocity downstream of the cylinder array with 0.2δ, 0.4δ and 0.6δ spacing respectively.

For the 0.4δ spacing case, it is easily observed in the first place that the merging of the cylinder wake happens further downstream, namely $x/\delta\sim2$. Each wake structure is merged with the neighboring wake and then settles at mid-spacing location where they maintain organized until the far field up to $\sim7\delta$ downstream. No secondary pairing is observed in this case indicating that the organization of these LMRs is more stable compare to the 0.2δ spacing case. In the far field, a pattern of small spanwise variation can still be observed and the long lasting organization suggest that there is no strong spanwise interaction between the low speed regions after the merging, therefore it can be concluded that the wake structures in this case is more stable. This is consistent with Ortiz-Dueńas et al. (2011) where wakes of the 0.4δ spacing cylinder array lasted beyond the measurement field up to $\sim4.5\delta$ downstream.

For the 0.6δ spacing case, the merging of wake structures happens further downstream at $x/\delta\sim3$, forming new LMRs in the mid-spacing location. These new LMRs last until the far field up to $\sim7\delta$ downstream and maintain a stronger spanwise variation. The spacing between these LMRs are $\sim0.6\delta$ which is the same as the perturbation scale introduced by the cylinder array. That is to say, the perturbation is well sustained by the cylinder wakes as they move downstream. Therefore, we can predict that the flow structure downstream of the cylinder array is most stable in the 0.6δ spacing case.

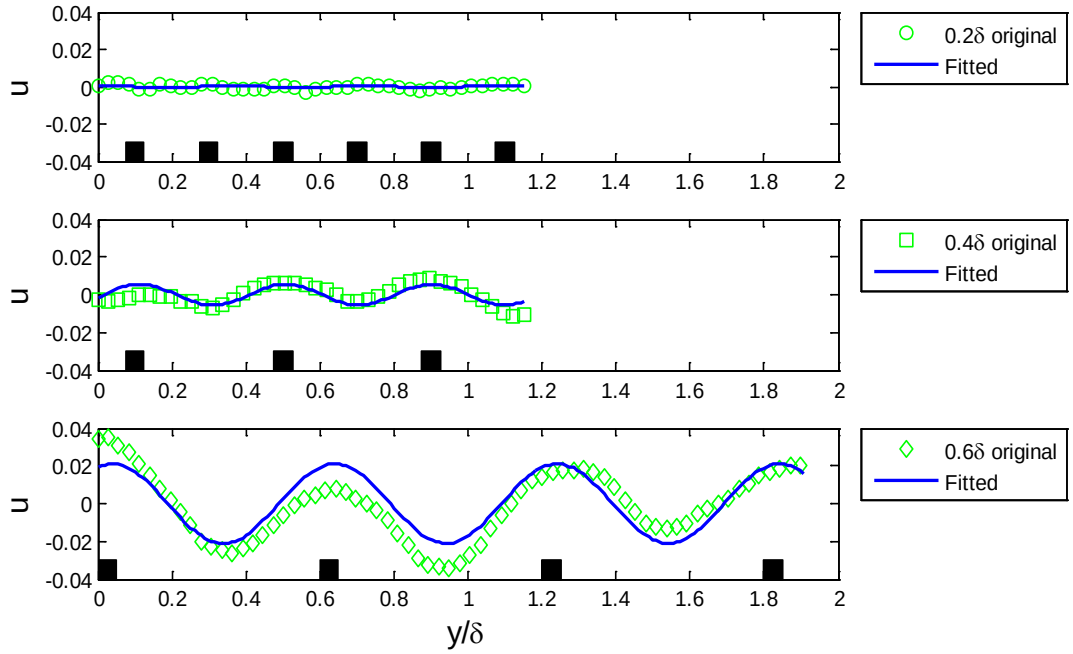

Figure 3. 4 Fitted spanwise fluctuation of streamwise velocity at x/δ=7. Green represents original data. Blue represents the fitted curve. Black rectangle shows the spanwise location of the cylinders, height not in scale.

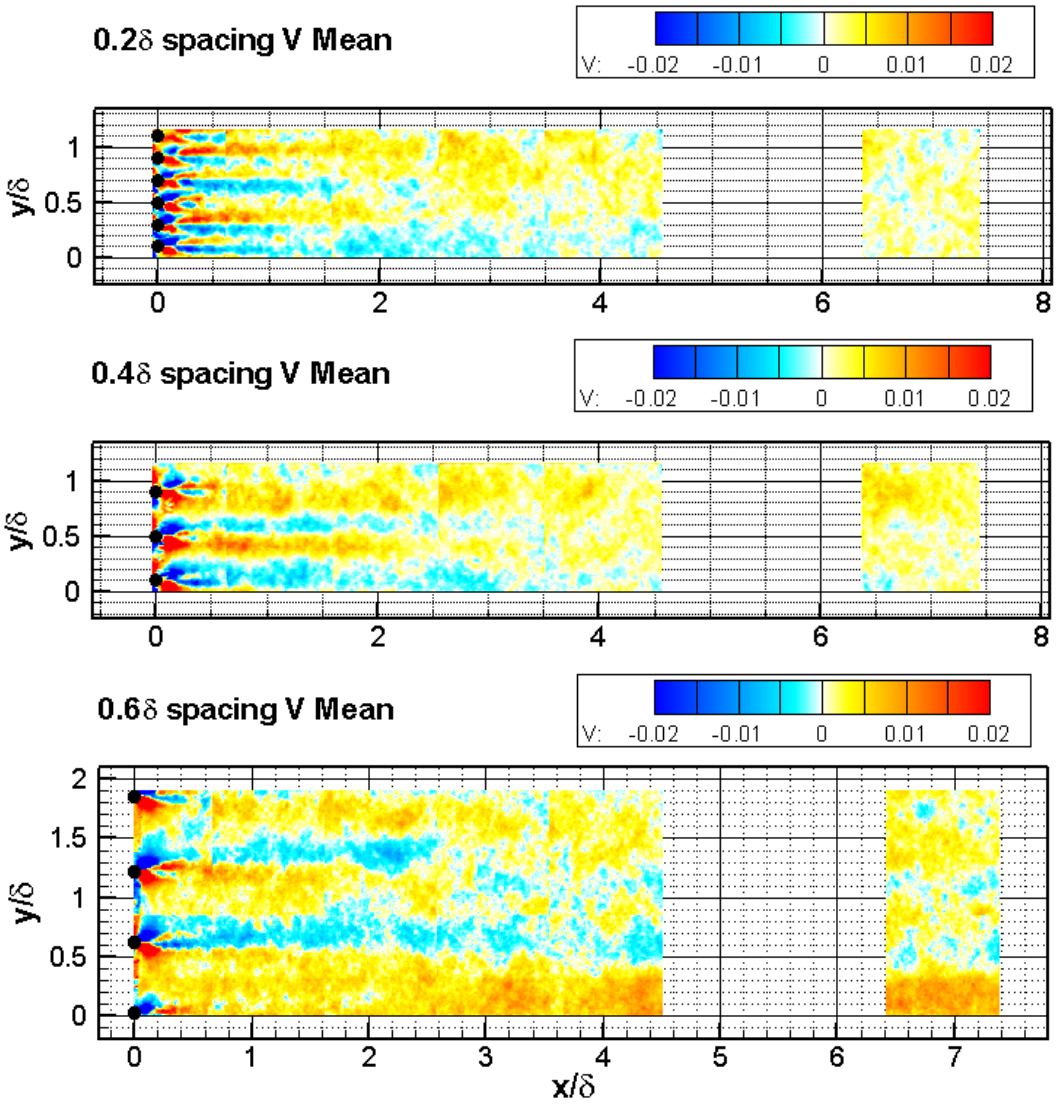

Figure 3. 5 Averaged spanwise velocity downstream of the cylinder array with 0.2δ, 0.4δ and 0.6δ spacing respectively.

To show the spanwise variation of the streamwise velocity, it is extracted at $x/\delta = 7$ and fitted to a sine function using least square method before being plotted in Figure 3.4. The 0.6δ spacing case has the strongest variation among all three cases, with fitted amplitude of $0.02U_\infty$. The 0.4δ spacing case has an amplitude of $0.005U_\infty$ while the 0.2δ spacing case has only $0.0008U_\infty$. Also, the high velocity regions are always directly behind the cylinders. From these data, we can see that the perturbation is best preserved in the 0.6δ spacing case in that in this scale the spanwise organization of the wake structure remains stabilized for the longest downstream distance and the strong spanwise variation is preserved as well.

Figure 3.5 gives the averaged spanwise velocity for all three cases. As is shown, in all cases some strong spanwise velocity variation is observed directly behind each cylinder, suggesting the spanwise motion of the fluid which corresponds to the shedding behavior of the cylinder wake. For 0.2δ spacing case, the most organized variation occurs within 2δ downstream, which is the same distance over which the merged structures remain parallel. This suggests that the strongest spanwise movement happens within $x/\delta \sim 2$ and the flow structures stay coherent. At $\sim 2\delta$ downstream and $y/\delta = 0.1$ it is clear that a blue region is directed upward in the figure (toward the positive y direction), indicating a more frequent spanwise movement at this location. This might explain the weak secondary merge observed in the averaged streamwise velocity field.

For the 0.4δ spacing case, no spanwise movement is observed after the cylinder array until $x/\delta \sim 2$ where a small distortion is spotted. This distortion suggests that the cylinder wake structures or LMRs become less stable at this location. Also noticed is that at $x/\delta \sim 4$, the spanwise variation becomes indistinct, suggesting the coherence of the cylinder wakes of LMRs is weakened. This corresponds well with the fading of spanwise variation of streamwise velocity starting at $x/\delta \sim 4$ as observed in Figure 3.3.

Also, for the 0.6δ spacing case, the spanwise variation of the velocity field can be seen evolving through the entire measurement field. In the region of $3\delta \sim 4\delta$ downstream, the blue regions seem to be shifted towards the mid-spacing location, which is the same downstream location where the streamwise LMRs are merged in Figure 3.3. Therefore, spanwise movement toward the mid-spacing locations are expected to be more frequent within the streamwise location of $x/\delta = 3 \sim 4$. Further discussions will be provided using the flying data. In the far field, a distinct pattern of spanwise variation separated by 0.6δ is still observed in this case, thus the least conclusion can be made is that the wake structure in this case is more stable in the sense that the perturbation scale introduced in the flow is well sustained.

Figure 3.6 shows the wall normal component of the averaged velocity field. The most obvious behavior is the downwash directly behind each one of the cylinders indicated by the negative wall normal velocity. This is caused by the tip vortex at the free end of the cylinder and

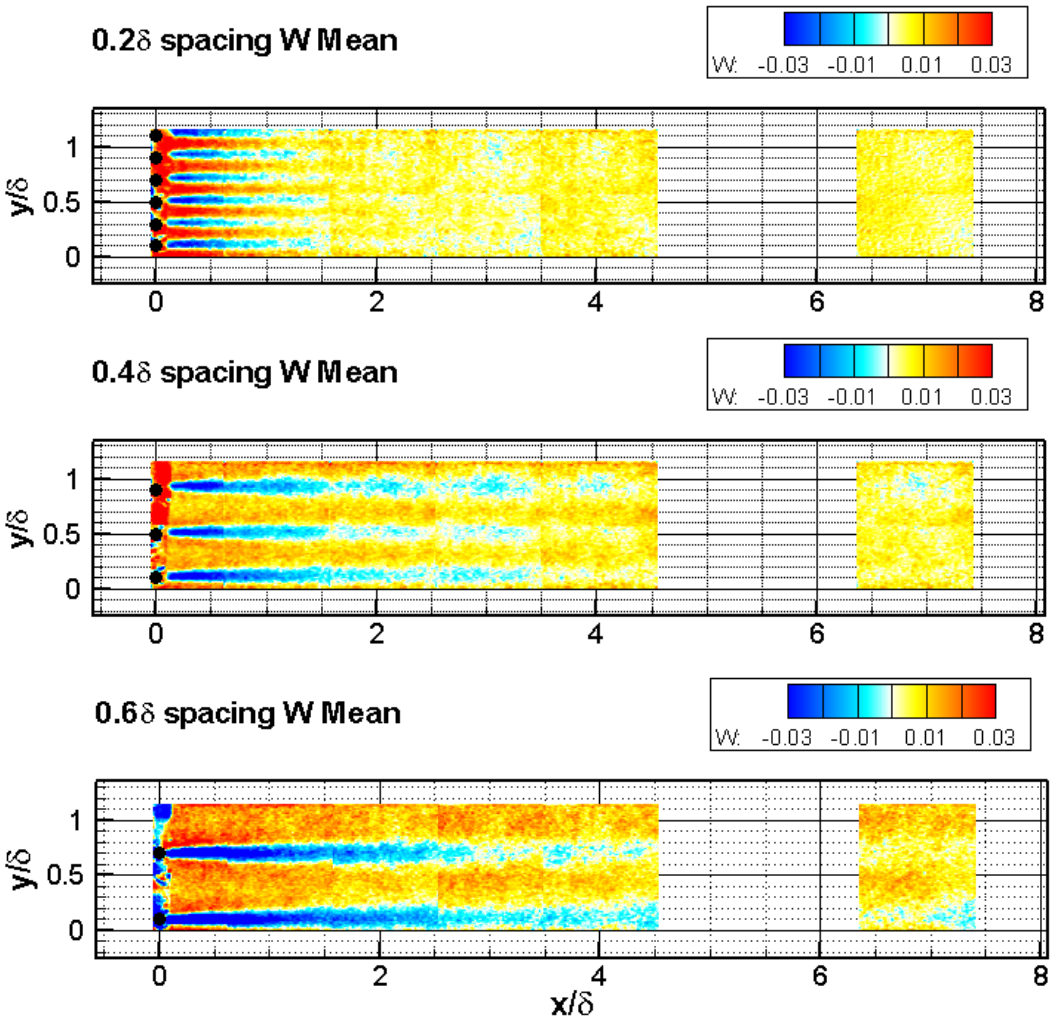

Figure 3. 6 Averaged wall normal velocity downstream of the cylinder array with 0.2δ, 0.4δ and 0.6δ spacing respectively.

due to this downwash motion, faster moving flow is brought downward towards the bottom wall. This can be used to explain the streamwise velocity contour where a region of faster moving fluid tends to develop directly behind each cylinder. For the 0.2δ spacing case, this downwash behavior last up to $\sim 1.5\delta$ just before the streamwise velocity pattern disappears. For the 0.4δ spacing case, the downwash behavior lasts up to $\sim 3.5\delta$ while the LMR patterns fade at $\sim 4\delta$ downstream. For the 0.6δ spacing case, some downwash persists throughout the measurement field. These observations might suggest that the downwash has an effect on the stability of the downstream flow structures. Further discussion will be made based on the flying data. At the mid-spacing location, an upwash movement is also observed and this motion is strongest in the 0.2δ spacing case. This might be the outcome of the base vortex system generated at the junction area where the cylinder is mounted, but since we are measuring just above the mid-height of the cylinder where upwash induced by base vortex system can be minimal, no conclusion can be made without further study.

The averaged streamwise RMS velocity is shown in Figure 3.7. It can be observed that the RMS is highest directly behind the cylinder, and this is partly due to the downwash that brings faster moving fluid toward the measurement plane. Also, since the aspect ratio of the cylinders in this study is 4, it is likely that the Kármán vortices are presents (for small aspect ratio cylinders, Kármán vortices are compressed by the tip vortices, see Sumner et al., 2004). These Kármán type vortices can induce velocity fluctuation behind the cylinder as well when the vortex is shed off the cylinder so higher RMS velocity is expected in this region.

In the 0.2δ spacing case, the highest RMS velocity regions quickly interact with their neighbors before a distinct pattern of high and low RMS velocity variation is formed. Note in this case, the lowest RMS is in the mid-spacing location and remains coherent up to $x/\delta \sim 3.5$. Beyond this location, the high RMS region begins to revert to the non-perturbed condition and in the far field at $x/\delta \sim 7$, the spanwise variation completely disappears.

In the 0.4δ spacing case, the same high RMS regions are present behind the cylinder and then expand in the spanwise direction to merge with the neighboring region creating a new high RMS region at the mid-spacing location. The same behavior is also observed in the 0.6δ spacing case, most obviously at $x/\delta \sim 3$. This is interesting because the behavior is totally opposite to that in the 0.2δ spacing case so we can tell the behavior of the downstream flow structure is different. With previous discussion on the wake structure, these high RMS regions in 0.4δ and 0.6δ spacing cases could be interpreted as frequent meandering of the wakes, rather than pairing, such that the wake structure meanders around the mid-spacing location to induce a higher RMS velocity.

Also noticeable is that the high RMS region in the mid-spacing location of the 0.4δ spacing case becomes less distinct after $x/\delta \sim 3$ compared to that of the 0.6δ spacing case,

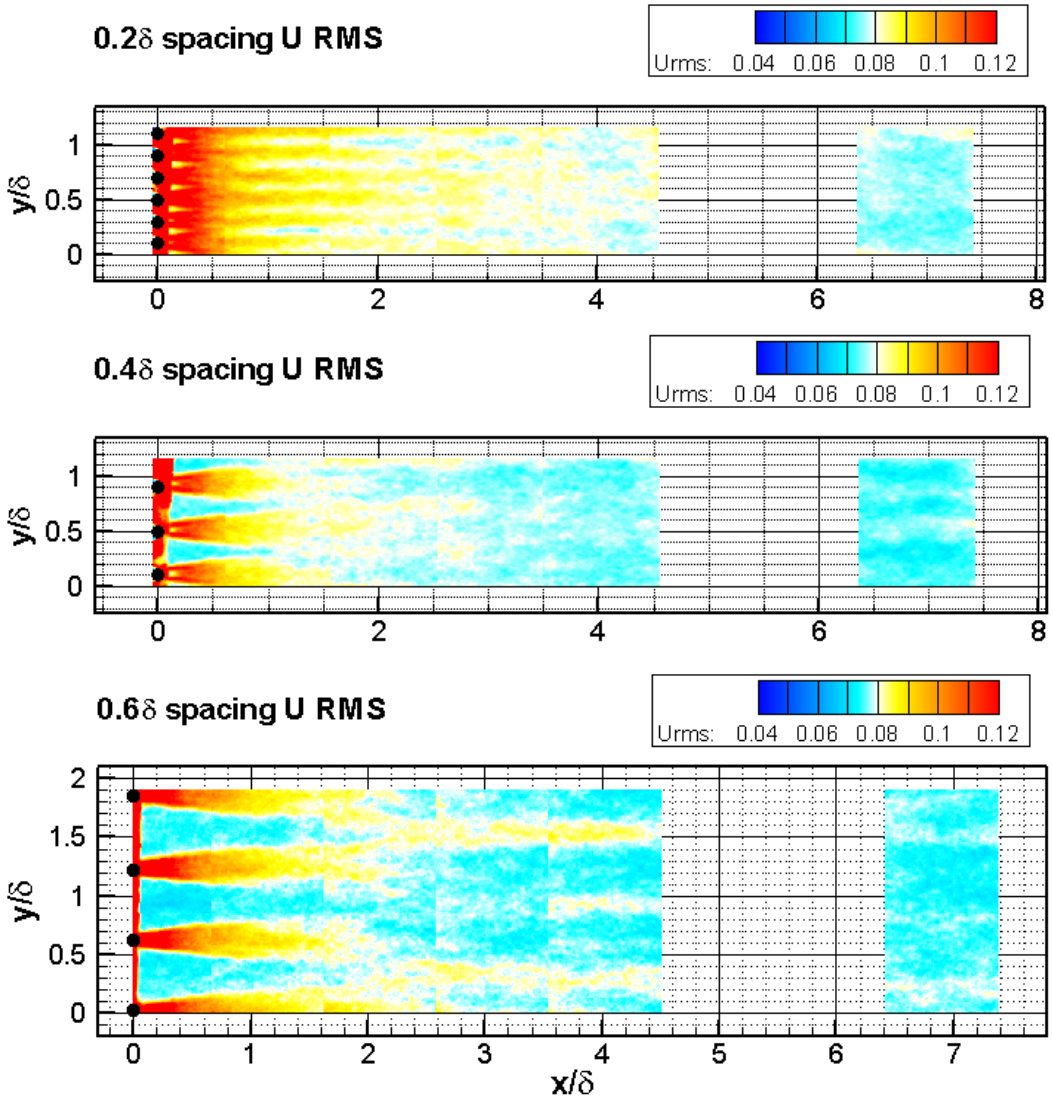

Figure 3. 7 Averaged streamwise RMS velocity downstream of the cylinder array with 0.2δ, 0.4δ and 0.6δ spacing respectively.

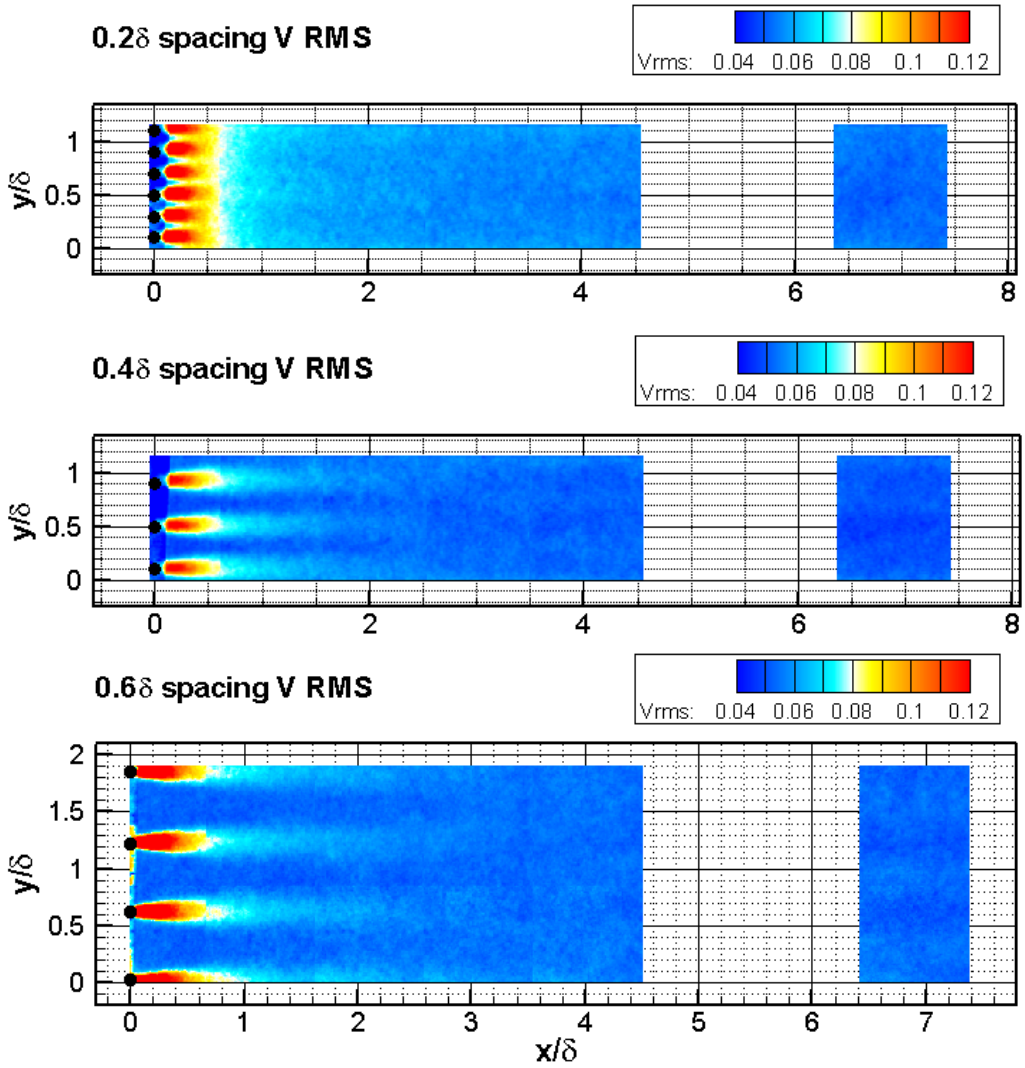

Figure 3. 8 Averaged spanwise RMS velocity downstream of the cylinder array with 0.2δ, 0.4δ and 0.6δ spacing respectively.

where in the latter case the high RMS regions extend beyond the measurement field. This can be interpolated such that in the 0.4δ case, after $\sim 3\delta$ downstream, the wake structure appears less often in the mid-spacing location while in the 0.6δ case these structures still meander around.

Figure 3.8 gives the averaged spanwise RMS velocity. It is clear that the high RMS region is directly behind the cylinder which is expected due to the Kármán type of vortex shedding. For the 0.2δ spacing case, the high RMS regions are merged together, but for 0.4δ and 0.6δ cases, there is no spanwise interaction of the high RMS region and the pattern of spanwise variations becomes more distinct as the spacing increases. It can be observed that the wake structure is more stable in 0.6δ case where the spanwise variations are preserved throughout the measurement field. These high RMS regions are stabilized in the mid-spacing location corresponding to the LMRs observed in the averaged streamwise velocity field. The wall normal component RMS velocity field appears less organized and no conclusions can be made on that.

3.3 Spanwise Scale

The low momentum region in the turbulent boundary layer has been studied for a long time and it was proved that there is a spanwise scale of these LMRs which indicates the spacing of the vortex packets in the flow. In this section, the spanwise scale of the wake structures is presented. A Fourier method is implemented as discussed in Chapter 2. With this analysis, the stability issue raised in previous discussion will be compared quantitatively between cases and zones. Note that each data case consists of 6 zones of data, measured at different downstream locations as defined in Chapter 2 section 2. The first five zones were continuously traversed downstream, referred to as zone 1, 2, 3, 4, and 5 respectively; and the far field measured at $x/\delta \sim 7$ downstream was referred to as zone 8.

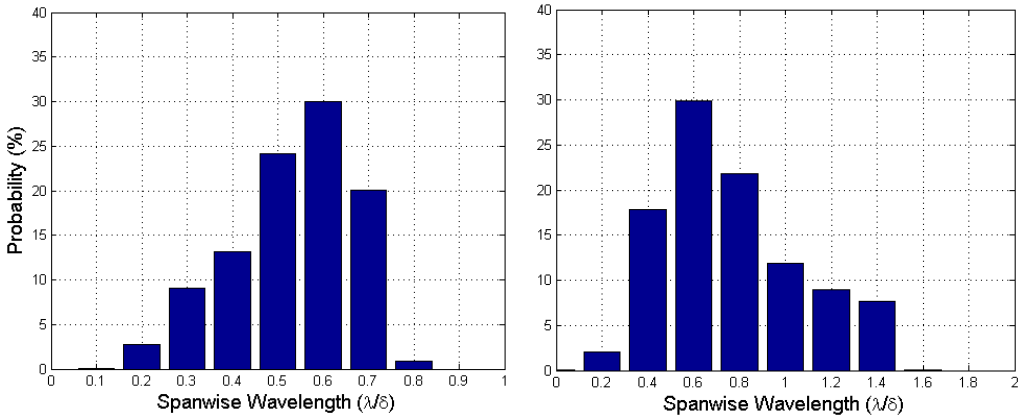

Figure 3. 9 Distribution of spanwise scales of NOCS (left) and NOCP (right)

Figure 3.9 shows dominant spanwise scales of the non-perturbed data case found in individual instances and streamwise locations for two data sets with different spanwise ranges, namely 1δ and 2δ. The resulting pdf peaks at $\sim 0.6\delta$ in both cases suggest that the most frequent spanwise spacing between two low momentum regions is $\sim 0.6\delta$. Note that both the spanwise range and the bin size of these two cases are different, with bin size chosen to be 0.1δ and 0.2δ respectively as discussed in Chapter 2. To compare the two data sets directly, the NOCS data is replotted using the bin size of 0.2δ with probability normalized by that of the 0.6δ bin. Now it can be observed that the first three bins yield a distribution similar to the NOCP case in Figure 3.10. Note that the 0.8δ bin does not match due to the limited spanwise range of the NOCS case.

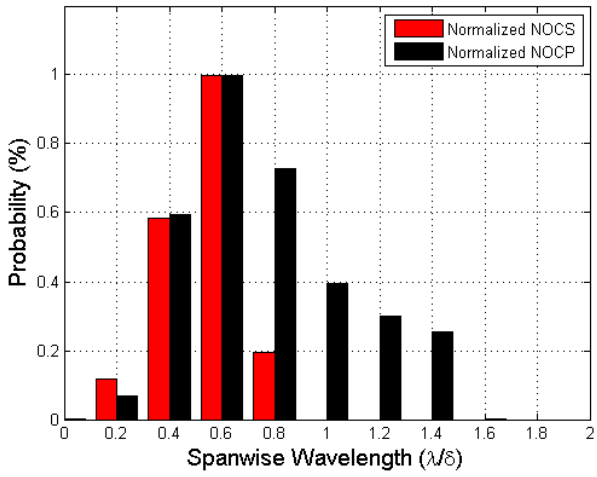

Figure 3. 10 Normalized Distribution of dominant spanwise scales using bin size of 0.2δ

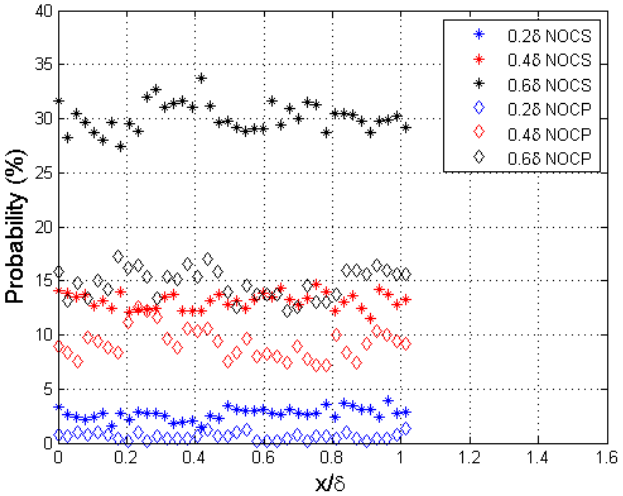

Figure 3. 11 Streamwise development of different spanwise modes

Figure 3.11 presents different spanwise modes against the streamwise location where every three streamwise data points are presented. Based on the perturbation scales used in this study, namely 0.2δ, 0.4δ and 0.6δ, these three corresponding modes are of most interest. For each specific mode, the scales in the range of $\pm 0.05\delta$ are counted, so that the percentage of NOCS in Figure 3.11 is similar to that of the same mode in Figure 3.9; yet for NOCP the percentage in Figure 3.11 is smaller due to range in which the scales are counted. Also, it is clear that since NOCP case has a wider span, the percentage of presented modes is less than that of the NOCS case. This is important if these data sets are to be compared. In subsequent discussion, the mean percentage of each mode is calculated and used for normalization.

The distribution of dominant spanwise scales for the 0.2δ spacing case is given in Figure 3.12. In zone 1, the region directly behind the cylinder, it is clear that the 0.2δ mode dominates. In zone 2, the wake structure starts to move toward the mid-spacing location and resulting in distinct low momentum regions as observed in Figure 3.3. By doing so, the local spacing between two instantaneous neighboring wakes can vary so that the dominant spanwise scale becomes less predictable. Therefore the percentage of 0.2δ mode drops significantly yet still remains above 15%, which is much greater than that of the non-perturbed case. Also it is clear that the percentage of larger scales has started to grow. Note that, in zones 2 through 5, the 0.4δ mode exceeds that of the non-perturbed case, indicating that the wake structures with 0.2δ spacing upstream have paired. From zone 3 to zone 5, the percentage of 0.2δ mode drops continuously and that of the 0.6δ and 0.7δ modes increase towards the non-perturbed condition.

From these behaviors it is obvious that the perturbation scale introduced by the cylinder is damping and the flow structure is returning toward the non-perturbed status. Finally at zone 8, it can be seen that the dominant spanwise mode distribution appears similar to that of the NOCS case, yet the percentages of smaller modes (i.e. $\lambda/\delta < 0.6$) are smaller than that of the natural case, while 0.7δ and 0.8δ modes have a greater percentage. This again suggests the pairing motion of the wakes such that structures with small spanwise scales interact and merge into new structures with bigger spanwise scales. Based on this discussion and previous velocity contours, it can be concluded that for 0.2δ spacing case, the flow structure downstream of the cylinder array is not stable in that the 0.2δ mode mostly disappears by $x/\delta \sim 2$ (zone 2) due to strong spanwise interaction and remains somewhat different to the non-perturbed condition in the far field at $x/\delta \sim 7$.

The same results are presented in Figure 3.13 to show the streamwise development of each mode. Note that the percentage of 0.2δ mode starts at almost 100%, this is reasonable as the scale is very small such that all flow organizations in the incoming flow will be broken down to this scale. After that, there is a local minimum at $x/\delta \sim 0.4$, which corresponds to the location

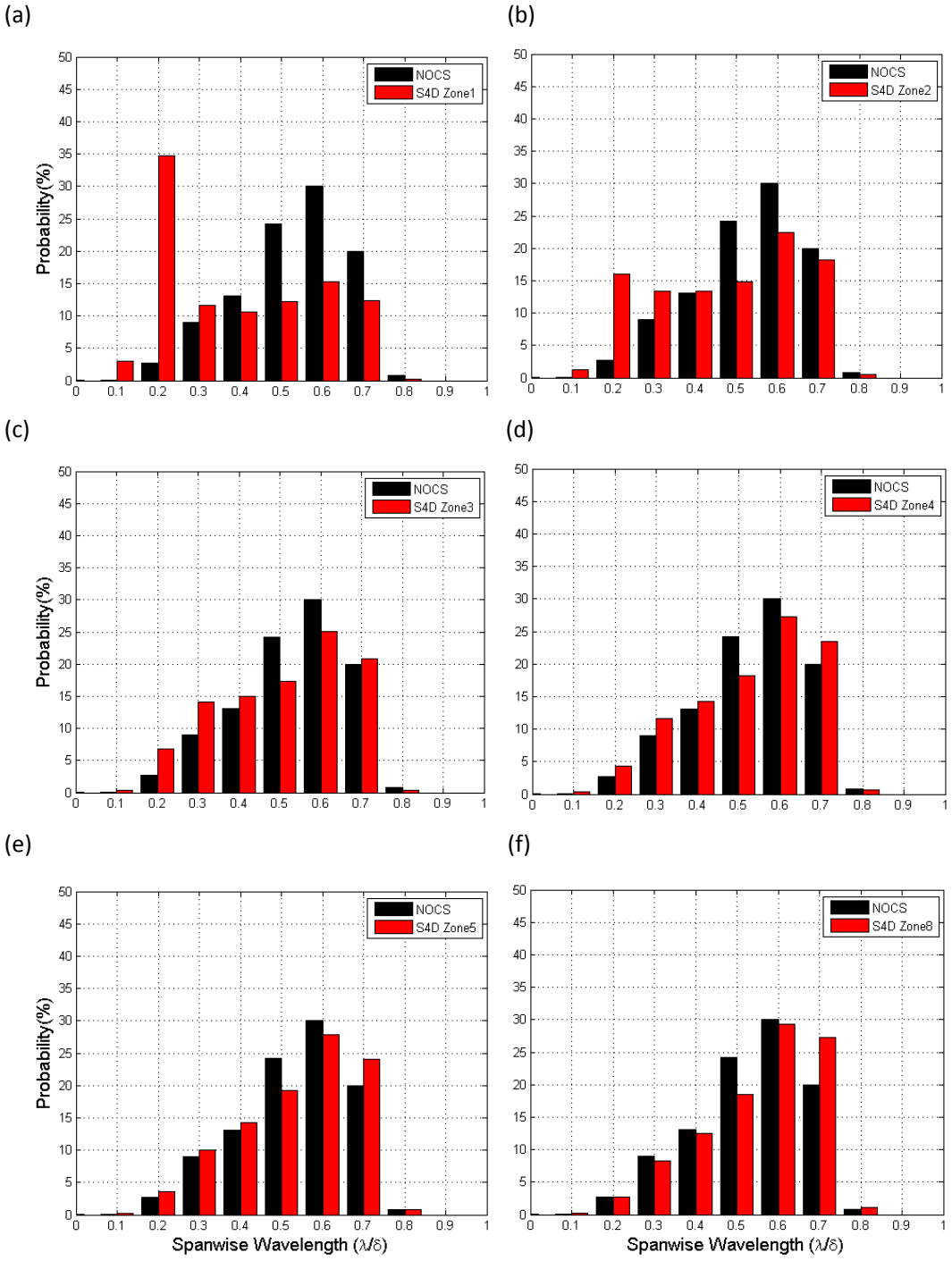

Figure 3. 12 Distribution of the dominant spanwise scale of 0.2δ spacing case (red) for (a) zone 1; (b) zone 2; (c) zone 3; (d) zone 4; (e) zone 5; (f) zone 8 respectively, with NOCS case (black).

where the pairing motions of the wake structure take place. When the pairing happens, there are various spanwise movements so that the specific 0.2δ mode is less frequent. From $x/\delta\sim0.5$ to $x/\delta\sim1$ the percentage of 0.2δ mode rises as the wake structure pairs into new LMRs and stays relatively stable in this region. After $x/\delta\sim1$, the 0.2δ mode just gradually decreases toward the non-perturbed condition.

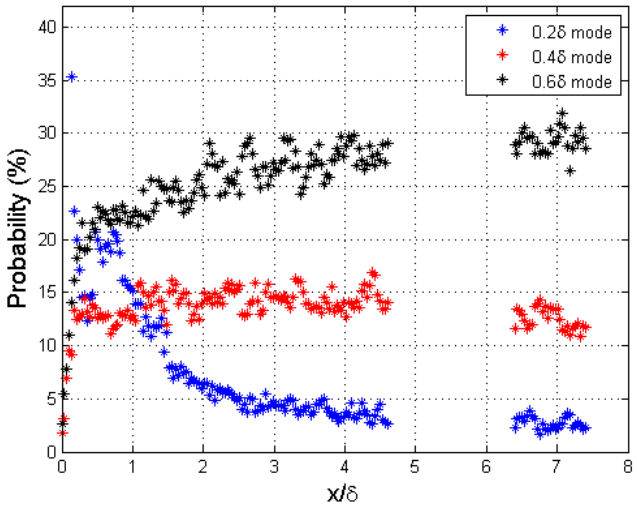

Figure 3. 13 Streamwise development of different spanwise modes for 0.2δ spacing case.

For 0.4δ and 0.6δ mode, they both start off with almost zero percentage and then increase. One interesting observation is the peak of 0.4δ mode at $x/\delta\sim0.4$, the same location of the local minimum for 0.2δ mode. This suggests that while the wake structures interact with neighbors the 0.4δ mode become more frequent. After that, from $x/\delta\sim0.5$ to $x/\delta\sim1$, while the wake merges into new LMRs separated by 0.2δ, a local minimum of 0.4δ mode is observed before it increases. Another observation is the difference between the percentage of 0.4δ and 0.6δ mode respectively at $x/\delta\sim4.5$ and $x/\delta\sim6.5$, such that the 0.4δ mode decreased and the 0.6δ mode increased. The difference suggests that the flow is continuously returning toward the non-perturbed status between $x/\delta\sim4.5$ and $x/\delta\sim6.5$. In the far field at $x/\delta\sim7$, the percentage of all three modes appear nearly identical with those in Figure 3.11.

The distribution for the 0.4δ case is shown in Figure 3.14. The 0.4δ mode dominates zone 1, same as the cylinder spacing and its percentage is slightly smaller than that of the perturbation mode in the 0.2δ spacing case. Note also that the 0.2δ mode is elevated compared with the non-perturbed case. By zone 2, the 0.4δ mode drops sharply as this is the region just before the major spanwise movement happens in individual fields so that the scale would be more disperse. It is supported by looking at the percentage of both smaller and bigger modes in zone 2 such that, other than 0.2δ mode, they are all bigger than their counterparts in

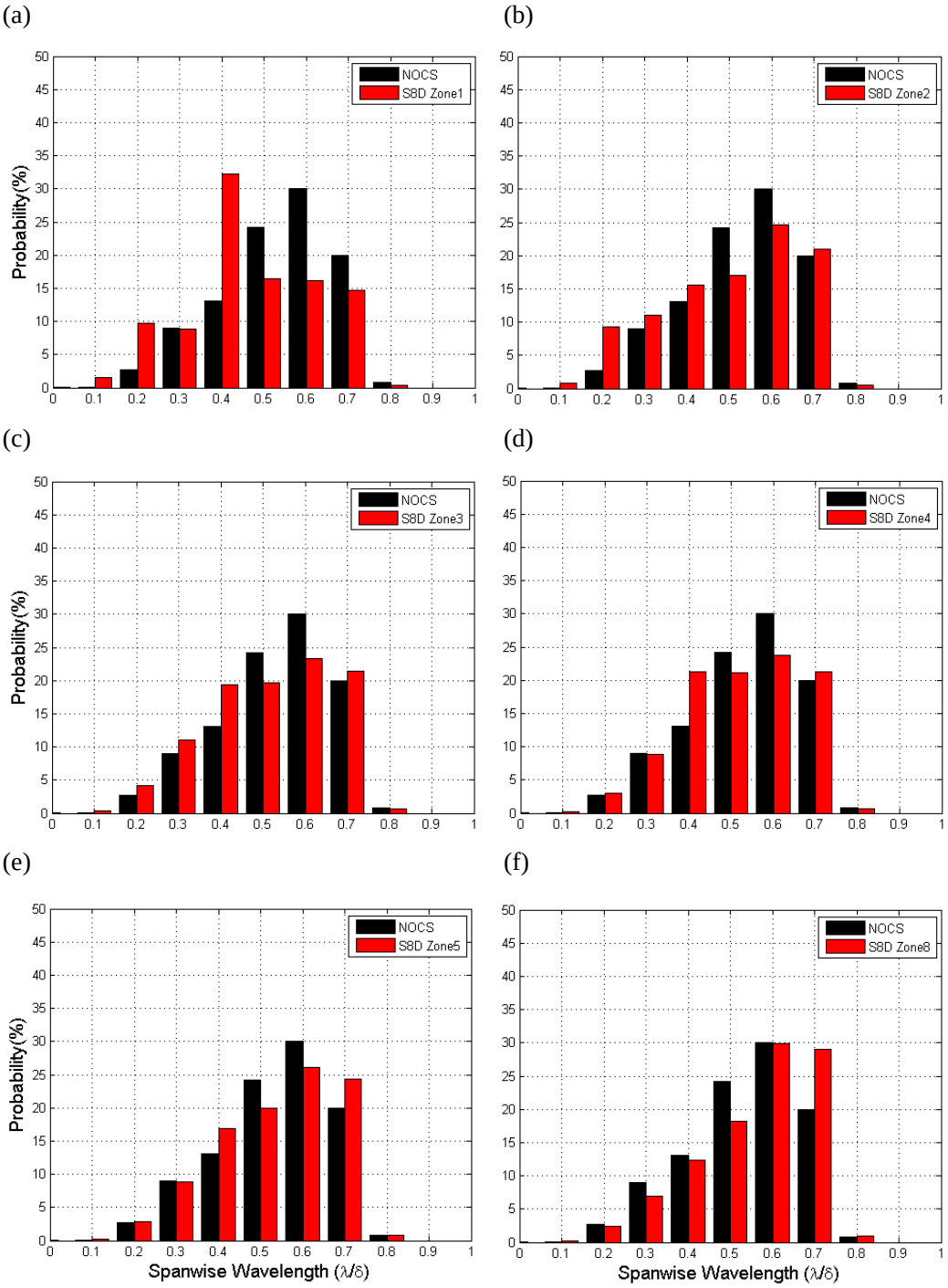

Figure 3. 14 Distribution of the spanwise scale for 0.4δ spacing case, (a) zone 1; (b) zone 2; (c) zone 3; (d) zone 4; (e) zone 5; (f) zone 8 respectively, with NOCS case (black).

zone 1.

Different from the 0.2δ case is that the percentage of the 0.4δ mode increases from zone 3 to zone 4 which corresponds to the LMRs in the mid-spacing location observed in the mean field starting at $x/\delta\sim2$, as shown in Figure 3.3. This is consistent with previous observation where the strongest spanwise movement happens at $x/\delta\sim2$ and then the cylinder wakes frequently settle in the mid-spacing location and maintain a spanwise spacing of $\sim0.4\delta$ as evolving downstream.

In zone 5, the 0.4δ mode still has a high percentage compared to the non-perturbed case, yet it returns to the non-perturbed case in zone 8. In zone 8, the percentage of 0.4δ mode is almost the same as that in the non-perturbed case, which is interesting because in the mean field a spanwise variation of the streamwise velocity is still present. This is interpreted a more repeatable spanwise location of the 0.4δ mode related to the cylinder locations. Also, it is difficult to resolve larger spanwise modes for this field of view, but it is interesting that the 0.7δ mode is significantly higher in the perturbed case.

Based on these observations, it can be concluded that, in this case, the 0.4δ mode is more organized in the flow compared to the non-perturbed case due to the cylinder array but not more frequent. This suggests that, by inserting the cylinder array, we are changing the behavior of the organizations of the cylinder wake and by increasing the spacing of the cylinder array, the stability of the downstream flow structure is also improved.

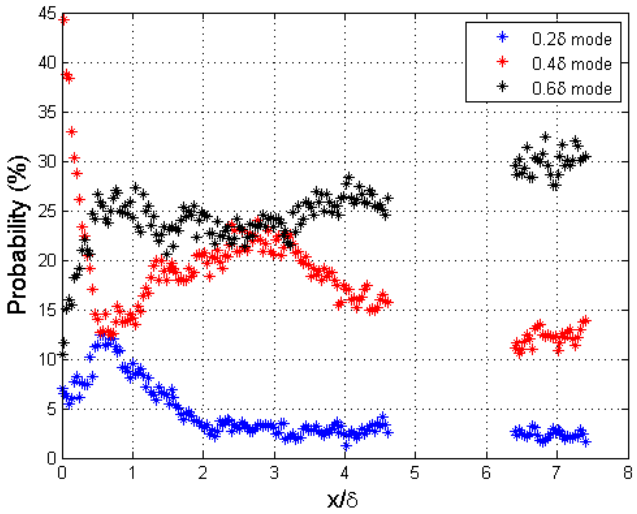

Figure 3. 15 Streamwise development of different spanwise modes for 0.4δ spacing case.

Figure 3.15 presents the same data against their streamwise development. The 0.4δ mode starts at $\sim55\%$ followed by a local minimum before $x/\delta\sim0.7$ where strong spanwise movements begin. After that, there is a rise of the 0.4δ mode, which corresponds to the LMRs

stabilizing in the mid-spacing location. The percentage starts to drop beyond $x/\delta\sim3$ before returning to the non-perturbed status seen in the far field at $x/\delta\sim7$. The 0.2δ mode peaks at $x/\delta\sim0.7$, which is the same location of the local minimum of 0.4δ mode; moreover, there is a local peak of the 0.6δ mode at the same location. This suggests the spanwise movement of the wake structures where the meandering motion disrupts the perturbation scale so that both bigger and smaller scales become more frequent.

Further, for the 0.4δ and 0.6δ mode, the difference between their percentages at $x/\delta\sim4.5$ and $x/\delta\sim6.5$ is also observed such that the 0.4δ mode decreased and the 0.6δ mode increased. This again suggests that the organization of flow structures is returning to the non-perturbed case. As a matter of fact, the percentage of all three modes appears identical to that of Figure 3.11. To better show this observation, the percentage of 0.2δ, 0.4δ and 0.6δ mode for S4D and S8D are plotted with the NOCS case in Figure 3.16. The percentage of 0.6δ mode in the figure is identical, but smaller and bigger modes have a different percentage compared to the non-perturbed case, this might suggest the spanwise pairing and merging behavior of structures in both 0.2δ and 0.4δ cases, although conclusions can only be made after examinations of the instantaneous data with swirling structures.

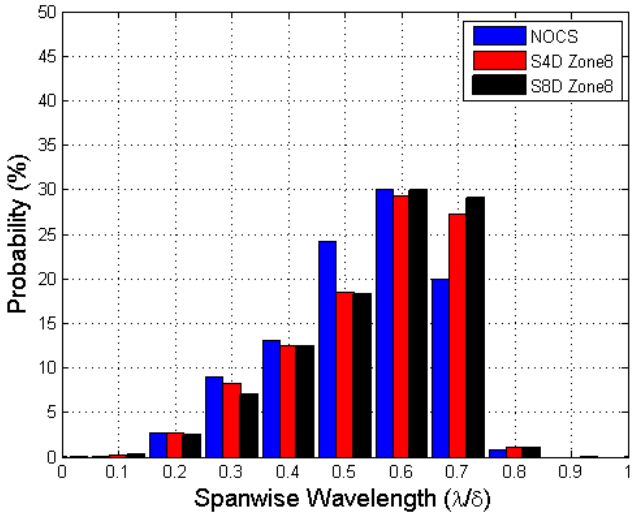

Figure 3. 16 Comparison of distribution of dominant spanwise scales of S4D and S8D cases in the far field at x/δ~7 with NOCS.

For the 0.6δ spacing case (Figure 3.17), the P12D data set is used so the spanwise range is two times bigger which is $\sim2\delta$. The most significant signature of these figures is that the percentage of the 0.6δ mode remains at a high level in all zones. Its percentage drops only at zone 2 and zone 3 where major spanwise movement is present based on the observation of the averaged field. In zone 8, its percentage is only $\sim10\%$ smaller than that of the zone 1 and still

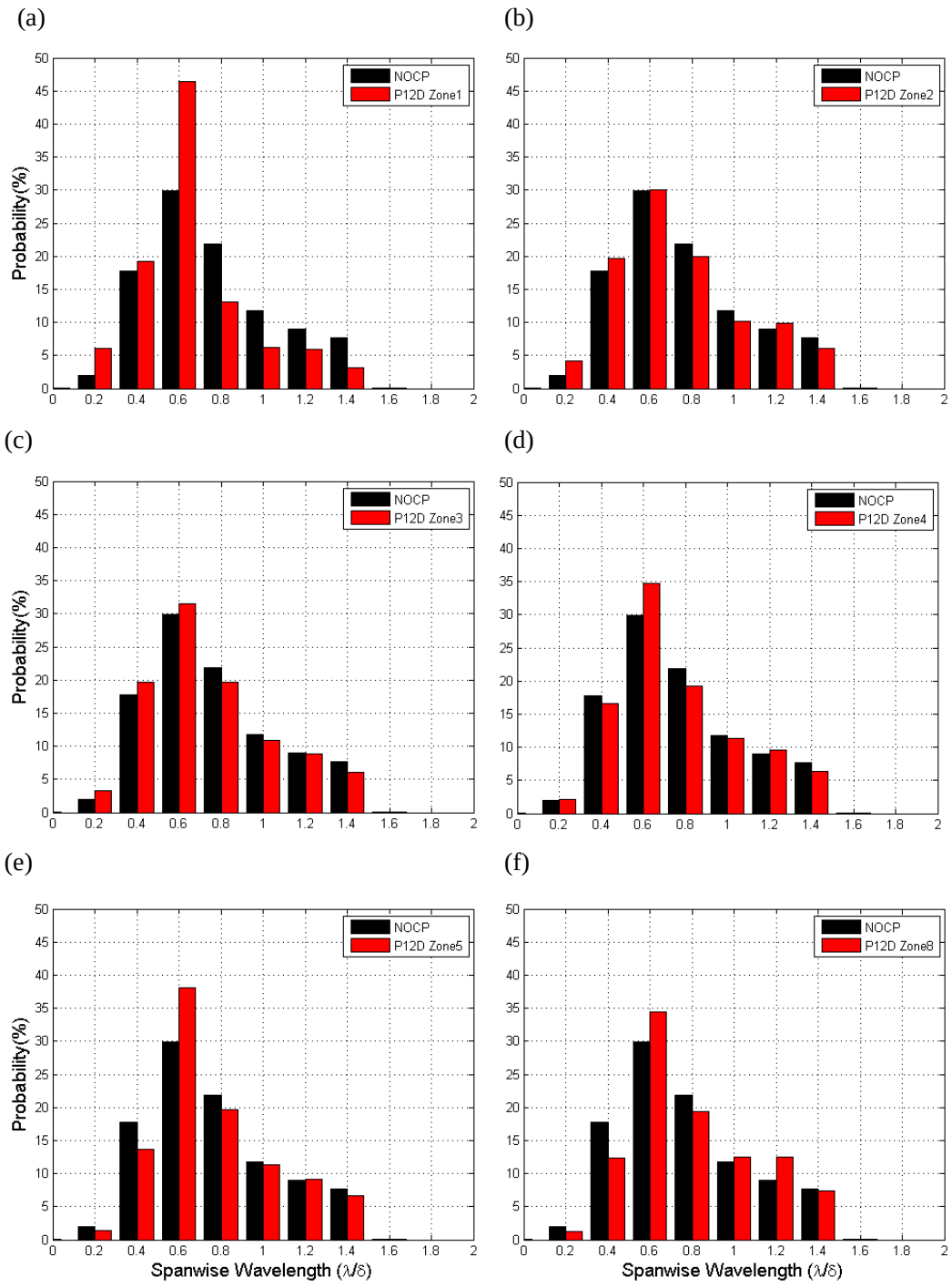

Figure 3. 17 Distribution of the spanwise scale for 0.6δ spacing case, (a) zone 1; (b) zone 2; (c) zone 3; (d) zone 4; (e) zone 5; (f) zone 8 respectively, with NOCP case (black).

higher than that of the non-perturbed case, which indicates that the perturbation introduced by the cylinder array is well sustained and organized throughout the measurement fields; that is to say, the dominant wake structure is most stabilized in this case.

Another interesting observation is that the distribution of the scales retains a shape similar to the non-perturbed case throughout the streamwise domain, which might suggest that the 0.6δ spacing perturbation has only a minor disruption of the flow structure. This makes sense as the 0.6δ mode is dominant in the non-perturbed flow of this study so perturbing this mode would be expectedly more efficient. Also noticeable is that the 1.2δ mode appears somewhat higher than the non-perturbed case. This is expected to be the result from instances where two cylinder wakes move toward opposite spanwise directions where the spacing between the wakes increases to 1.2δ. Further discussion on this point will be provided using the flying data.

Figure 3.18 gives the streamwise development of these modes. It is clear that the 0.2δ mode is not important in this case. The 0.6δ mode starts off with a high percentage of $\sim$90% and comes to a local minimum at $x/\delta\sim1$, corresponding to the location just before the presence of strong spanwise movement. Then it approaches a steady state at $x/\delta\sim3$ and remains at the same level until the far field. Also noted is that the 0.4δ mode has a local maximum at $x/\delta\sim1$ and this can be explained by the spanwise meandering of the cylinder wake.

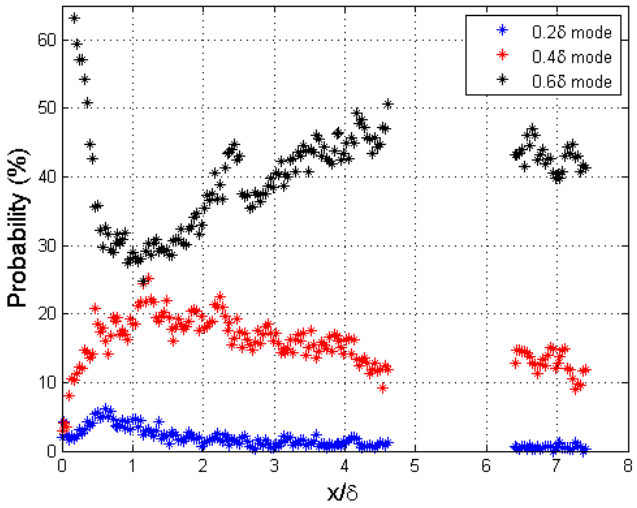

Figure 3. 18 Streamwise development of different spanwise modes for 0.6δ spacing case.

Different from the previous two cases, for 0.4δ and 0.6δ mode, no significant difference between their percentages at $x/\delta\sim4.5$ and $x/\delta\sim6.5$ is observed here, indicating that the flow structure is stable throughout these locations.

In Figure 3.19, the characteristic mode is defined as the same mode as the perturbation scale, e.g. 0.2δ mode for the 0.2δ spacing case. All data are normalized by the mean value of the

corresponding percentage in the non-perturbed case as shown in Figure 3.11 so that 1 means the percentage of the mode is the same as that in the non-perturbed flow.

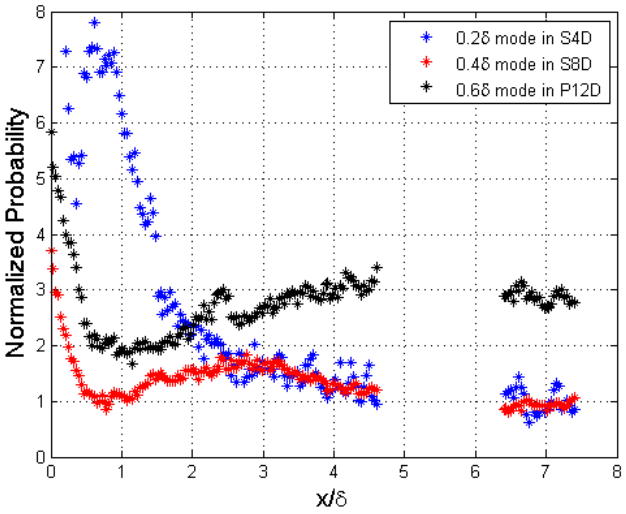

Figure 3. 19 Streamwise development of the characteristic modes.

It is obvious that in the far field, the normalized probability of 0.2δ and 0.4δ modes reverts to 1, suggesting that the importance of these modes is nominally the same as that in the non-perturbed case. However, for the 0.6δ case, the 0.6δ mode dominates about 3 times more often than the non-perturbed case, suggesting that the downstream LMRs remain coherent at the perturbation scale up to the far field at $x/\delta\sim7$ downstream. Also, by looking at the local minimum of each mode at $x/\delta < 7$, the 0.2δ mode reaches the minimum first but then develop to a local peak at $x/\delta\sim1$ while the other two modes gradually go to the local minimum. This again indicates the strong spanwise movement of wake structures for the 0.2δ case and the relatively mild meandering for the other two cases. These observations all together lead to the conclusion that by increasing the spanwise spacing of the cylinder array, the flow structure is more stabilized.

The detailed mechanism of the stability issue is not clear as of yet, but efforts will be made to answer that question by looking at the flow structures using instantaneous data fields in the next chapter.

Chapter 4

Results and Discussion: Instantaneous Results

In this chapter, the instantaneous results are discussed (see Table 3.1 for list of data sets). All instantaneous data are captured using the Stereo-PIV setup. The flying data has about 40 runs for each set where each set has approximately 28 consecutive fields. In the following discussion, the flying data is discussed, and efforts will be made to answer the stability issue raised in the previous chapter by tracking the flow structures in selected runs. All parameters are normalized by the freestream velocity U_∞ and the boundary layer thickness δ.

4.1 Non-perturbed case

In this section, the FNOC data is presented providing a Lagrangian description of the movement of flow structures. Two selected runs are given in Figure 4.1 and Figure 4.2 for both streamwise velocity and wall normal velocity with 2d swirling strength (λ_{ci}). Every third field is shown to avoid overlapping. The streamwise velocity is computed relative to the averaged mean velocity ($0.37m/s$) without the cylinders so white contours are equivalent to $0.37m/s$. The wall normal component is calculated on an absolute scale so white contours are equivalent to zero normal velocity.

Figure 4.1 represents the most common (more than 60% of all runs) organization of the flow structures where two LMRs are observed. The first thing to notice is that these LMRs are long lasting that they persist over a range greater than $\sim 8\delta$ which is consistent with previous studies, e.g. Marusic & Hutchins (2007a), Gao (2011) and Lee & Sung (2011). Although some references reported smaller streamwise scale of these LMRs, e.g. Balakumar & Adrian (2007) and Dennis & Nickels (2011b), those measurements were carried out in the outer region of the turbulent boundary layer where the large scale coherent structures were less frequent. The spanwise spacing between these structures is varying in the range of $0.4\sim0.7\delta$ due to the spanwise movement of the LMRs. Also, by plotting the swirling structures, it is easily observed that they are well aligned along the sides of the LMRs. This is consistent with previous studies

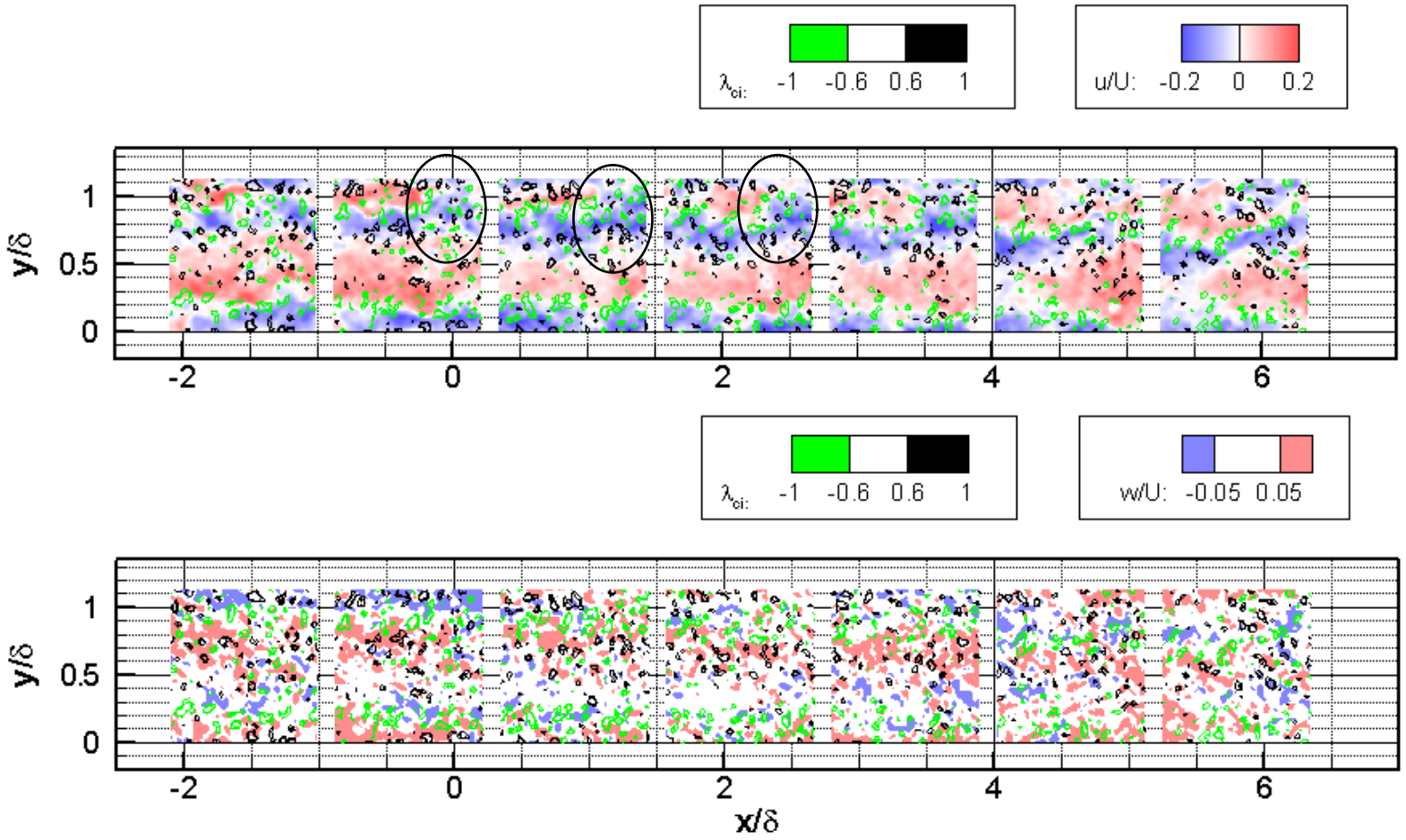

Figure 4.1 A single run of FPIV instants of streamwise and wall normal velocity with 2d swirling strength for non-perturbed flow, representing the most common organization. Large black ellipses indicate the position of possible spanwise interactions.

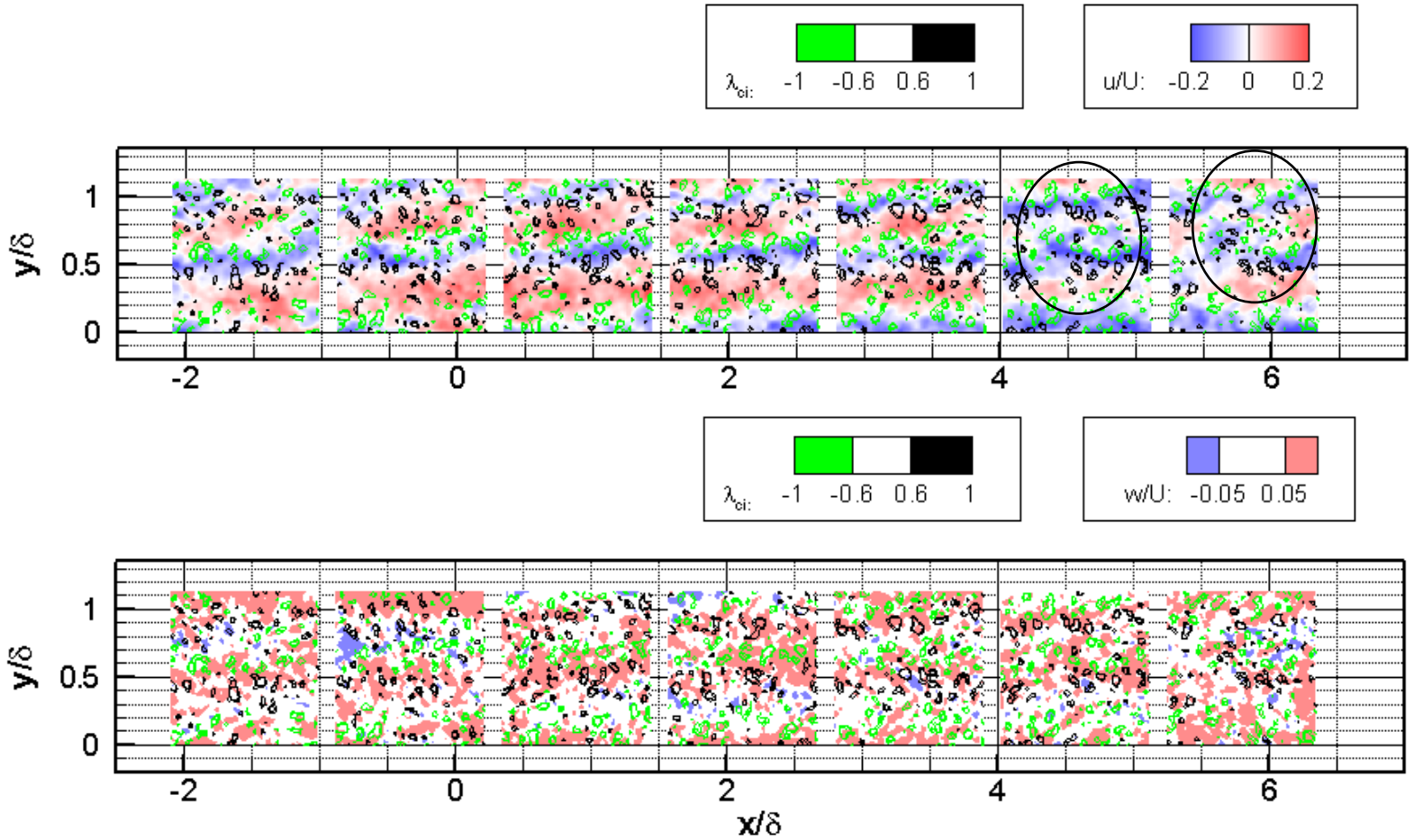

Figure 4.2 A single run of FPIV instants of streamwise and wall normal velocity with 2d swirling strength for non-perturbed flow, representing a less frequent organization. Large black ellipses indicate the locations of possible spanwise interactions.

that the LMRs are induced by coherent hairpin vortices roughly aligned in the streamwise direction so the legs of these hairpin vortices are expected on both sides of the LMRs appearing as counter-rotating swirls.

Considering the hairpin model, previous studies have also shown that Q2 events are frequently observed in these slow moving regions such that a positive wall-normal velocity is induced where the forward-leaning hairpin vortex is present. This is proved by the wall-normal velocity contours in Figure 4.1. In between the counter rotating swirl structures, a positive wall-normal velocity region is often observed in the same organization as the low streamwise velocity, and they moves laterally in the same fashion. These signatures together confirm the streamwise organization expected for coherent vortex packets.

Figure 4.2 gives an example that occurs less frequently (about 20% of all runs) in the field of views where three LMRs are present. These packets persist over a range of $\sim 8\delta$ as well and the spanwise scale is approximately 0.5δ with minor spanwise movement in the order of $\sim 0.1\delta$. Positive wall normal velocity regions are also observed in these slow moving regions, same as the counter rotating swirl structures on both sides, indicating the organization of coherent vortex packets. By comparing Figure 4.1 and Figure 4.2, the difference of the population of the swirling structures is obvious such that Figure 4.2 shows denser contour circles. This makes sense in that Figure 4.2 has three LMRs and these LMRs are induced by hairpin vortices; consequently, more swirls (legs of the hairpin vortices) are expected.

In some other runs, the LMRs are not distinct in the fields but when there are distinct LMRs, the spanwise location and spacing between them varies. These LMRs appear randomly at certain spanwise location so the velocity variation smooth out when the fields are averaged; this explains why the averaged velocity field appears uniform as shown in Figure 3.1.

By the nature of streamwise velocity contour and the swirling structures, some minor interactions between adjacent LMRs are visible. The spanwise interaction is indicated by the mixing of the black and green swirl structures (marked by large black ellipses) in Figure 4.1 and Figure 4.2. For example, at $x/\delta \sim 0$ and $x/\delta \sim 2.5$ in Figure 4.1 at $y/\delta \sim 0.9$, a mixture of black (positive) and green (negative) swirls is observed and this is not obvious in further downstream fields, suggesting a possible splitting of the LMRs. This is also supported by the fact that the LMR in the mid-span is continuously moving towards the negative y direction, causing the spanwise spacing between the two LMRs to become smaller. On the other hand, in Figure 4.2, the interaction is not observed until $x/\delta \sim 4.5$ suggesting a possible merging behavior. In this case, the spanwise spacing remains the same until the merging starts where the spanwise spacing becomes smaller. Thus, it can be concluded that the merging or splitting behavior of the structures happens over relatively a large time scale and the change of status is mild, but this will be changed by putting in the cylinder array.

4.2 0.2δ spacing case

Figure 4.4 and Figure 4.5 give two selected representative runs of the F4D case. It is easily observed for both cases that the streamwise velocity is decreased significantly (shown by strong blue contours). This suggests that the cylinder array has greatly affected the structures in the flow at the measurement height.

In Figure 4.4, the incoming flow appears to have two LMRs comparable to Figure 4.1, and the swirl structures are well aligned in the streamwise direction on both sides of the LMRs. Immediately downstream of the cylinders, the streamwise velocity is greatly decreased, and neighboring wake structures appears to interact. Consequently, the number of the swirl structures increases, and their size becomes more diverse. This suggests that the cylinder array has introduced a strong perturbation to the flow and the incoming vortex packets are broken down to smaller scales. These smaller scale flow structures immediately interact with neighboring structures so that the pattern remains disorganized up to $x/\delta \sim 2$. Then these structures start to reorganize themselves towards the status similar to the incoming flow, i.e. two independent LMRs are observed after $x/\delta \sim 2$, and their spanwise spacing and location are similar to that of the incoming flow. The spanwise movement of the swirl structures suggests the same which explains the weak secondary merging behavior observed in the averaged field in Figure 4.1. This process is shown also in Figure 4.3 as part of enlarged Figure 4.4.

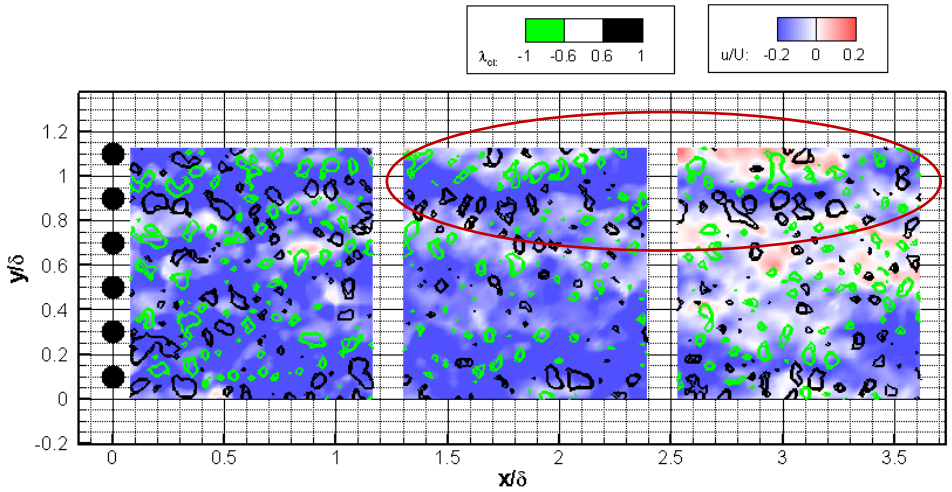

Figure 4. 3 Spanwise interactions and reorganization of the wake structures. Reorganized LMR is marked by the large red ellipse.

By looking at the wall-normal component, some downwash behavior is observed immediately behind each cylinder. These movements tend to bring faster moving fluid towards

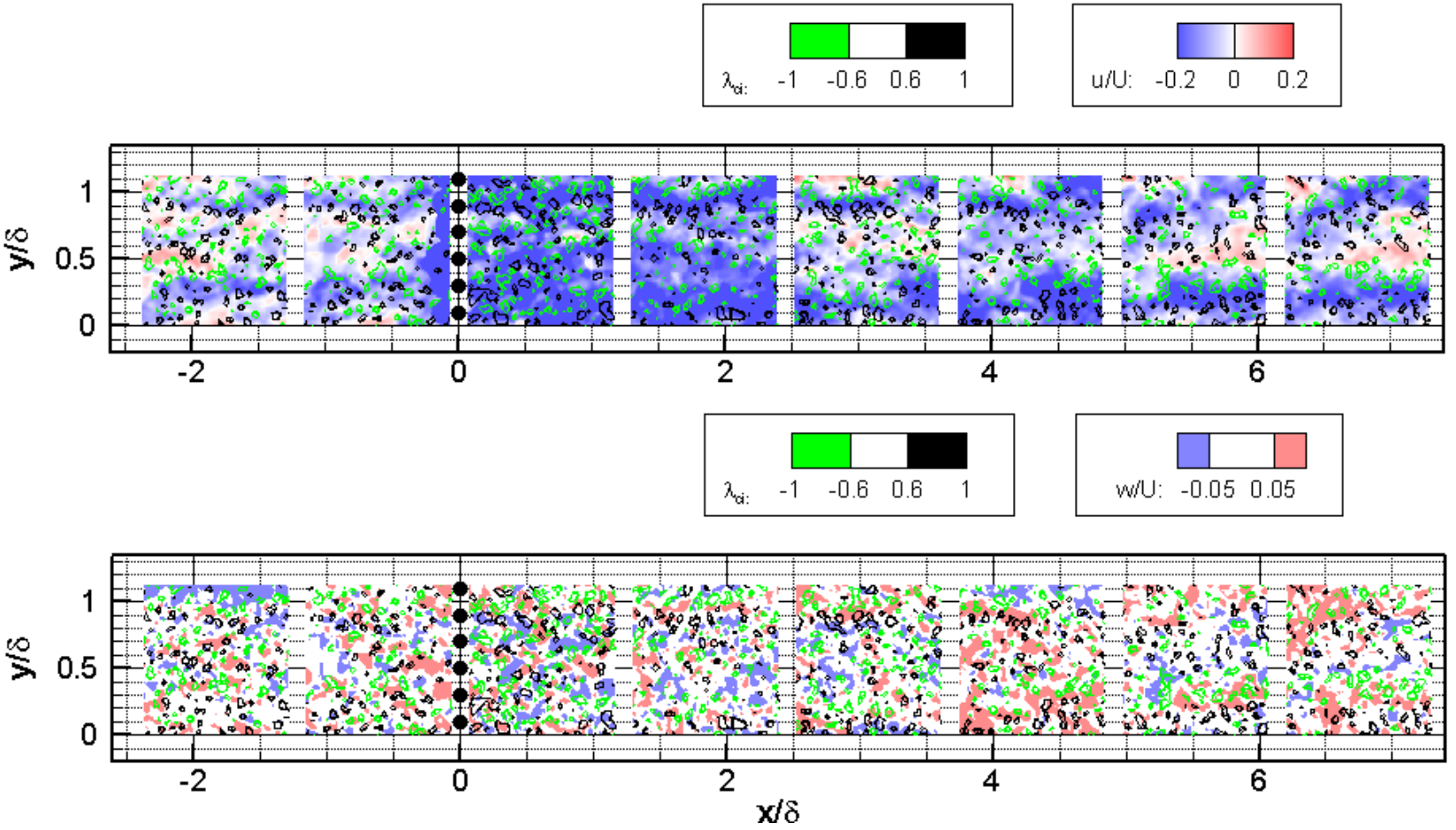

Figure 4.4 A single run of F4D case; streamwise and wall normal velocities are shown in blue and red contours; 2d swirling strength is shown in green and black contour lines.

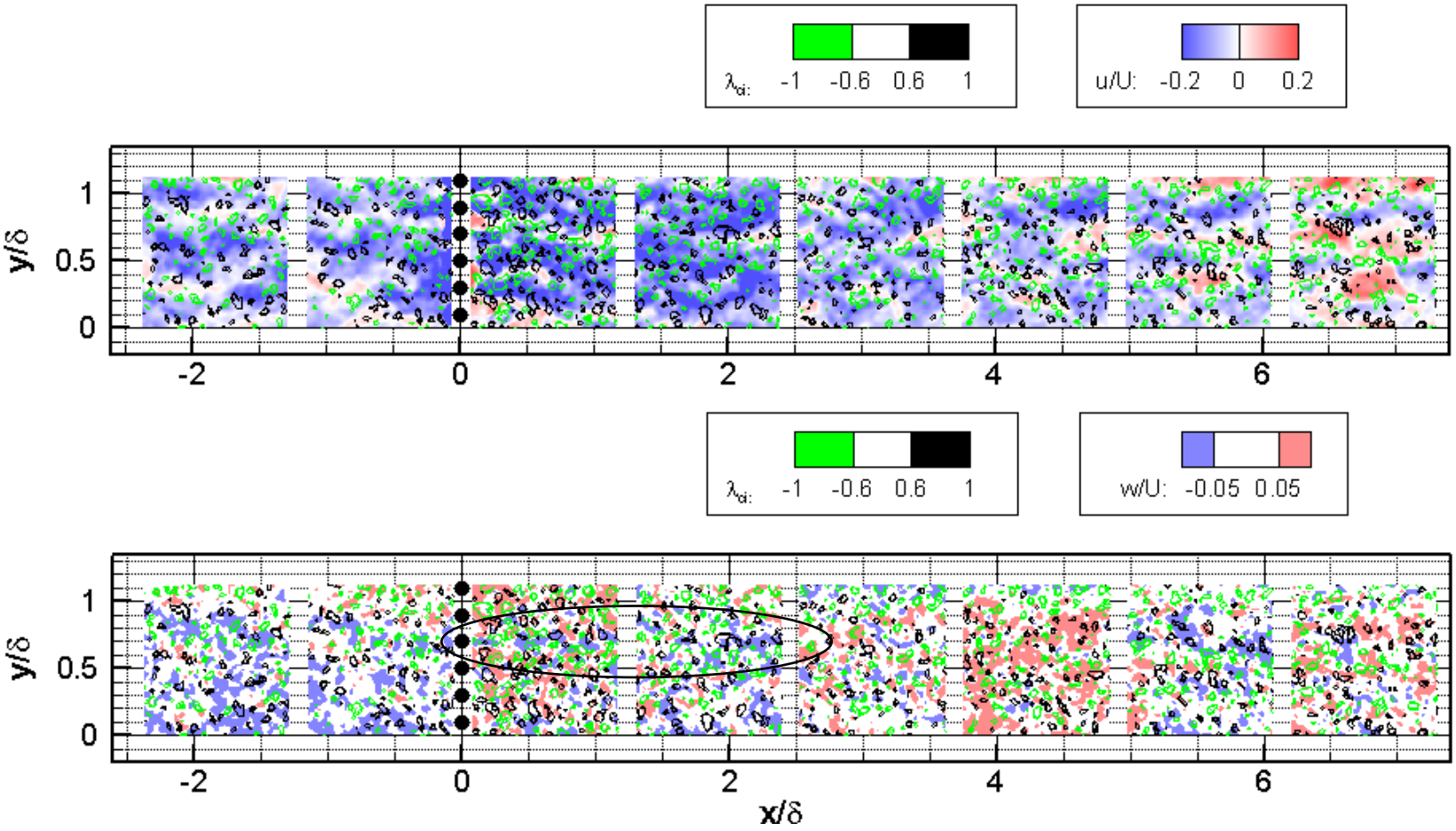

Figure 4.5 A single run of F4D case; streamwise and wall normal velocities are shown in blue and red contours; 2d swirling strength is shown in green and black contour lines. The downwash observed in wall normal component is marked by the large black ellipses.

the measurement plane inducing a higher streamwise velocity. In Figure 4.5 for example, a streak of downwash is present at $y/\delta \sim 0.6$ and a higher streamwise velocity is observed at the same location. This suggests that the downwash from the tip of the cylinders might affect the behavior of the wake structures; in this case, due to the fact that the spacing of the cylinders is small and the spanwise interaction of the wake structures are most dominant, the downwash does not seem to have a profound influence on the fluids at measurement height.

For Figure 4.5, although there are likely three slow moving zones of the streamwise velocity, the swirl structures are not well organized compared to Figure 4.4. So in this case, the individual cylinder wakes appear more clear and each one of them is tilted towards the mid-spacing location with visible spanwise interaction identified by the mixing of green and black swirl structures. The number of the swirl structures is also increased after the cylinder array and they reorganizes at $x/\delta \sim 2$. This is consistent with Figure 4.4 and previous observations. After this location, the slow moving structures remain somewhat coherent and the final organization is again well correlated with the incoming flow with a translation in the spanwise direction of -0.1δ which is half the spacing.

Note that the LMRs become more distinct in the far field ($x/\delta \sim 7$) of both runs, and the swirls are better aligned in the streamwise direction. One important observation is that the structures in the far field correlate well with the incoming flow, so it can be concluded that the incoming condition affects the downstream structures. Consequently, the behavior of the structures in the far field is expected to be similar to those in the incoming flow; that is the reason why the averaged far field velocity maps and the distribution of dominant spanwise modes appear similar to the non-perturbed flow.

4.3 0.4δ spacing case

Three selected runs from the F8D data set are presented in Figures 4.6, 4.8 and 4.9 respectively. With larger spacing of the cylinders, the blockage introduced by the array is decreased. Figure 4.6 is chosen to represent the case where the incoming flow is rather uniform such that the low momentum structures are not observed as independent streamwise streaks. The swirling structures also suggest that there are no strong coherent packets in the flow. In this case, three cylinder wakes are distinct immediately after the cylinder array. Although they are seen to be tilted towards the mid-spacing location, no obvious interactions are observed in the near field ($x/\delta < 0.5$) because the swirls (green and black contour lines) are well aligned on each side of the cylinder wake. After $x/\delta \sim 1$, some mixing of green and black swirl structures can be observed throughout the span, suggesting a stronger spanwise interaction. At $x/\delta \sim 2$, two independent LMRs are observed at the mid-spacing locations (marked by large red ellipses)

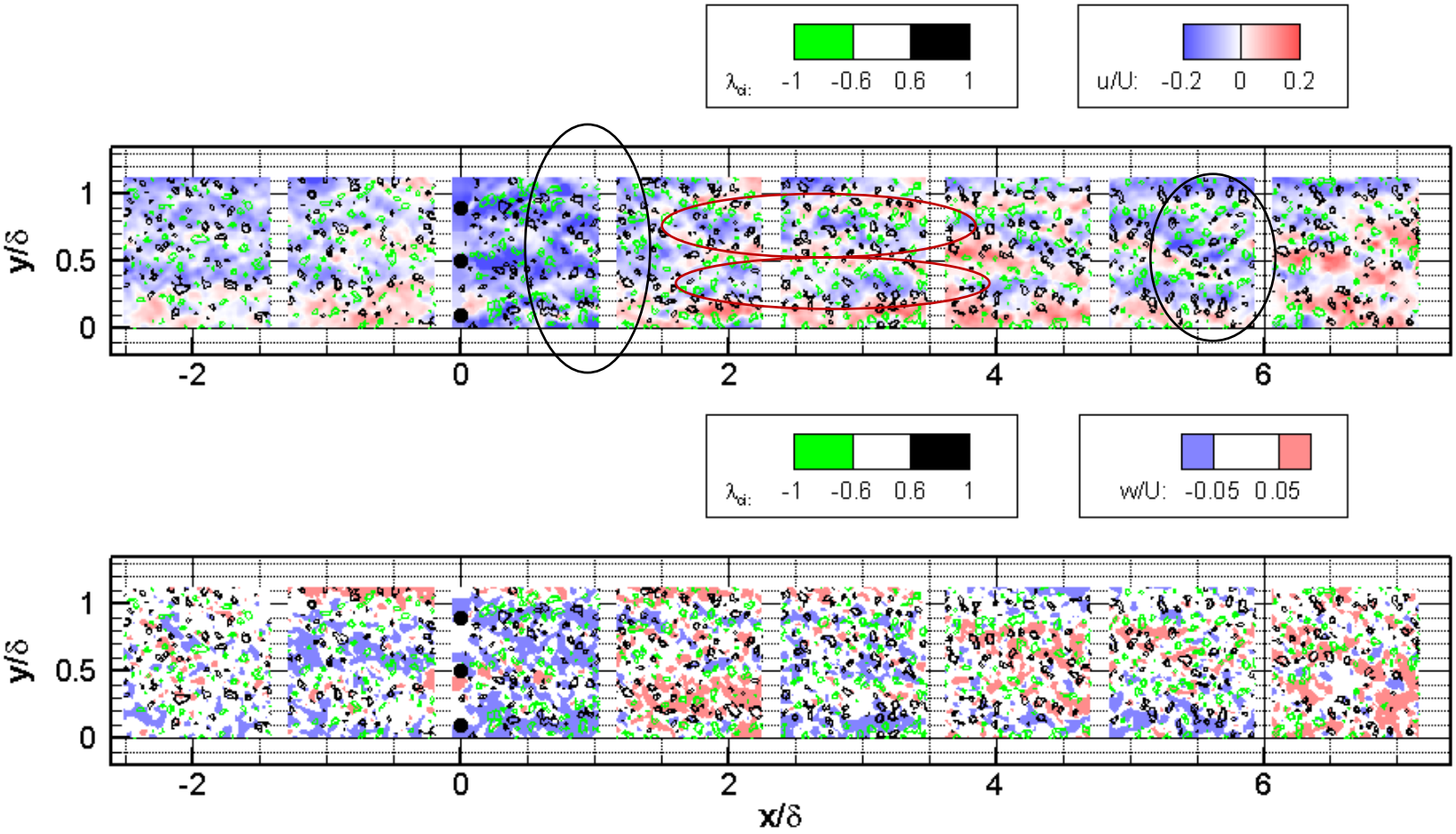

Figure 4.6 A single run of F8D case; streamwise and wall normal velocities are shown in blue and red contours; 2d swirling strength is shown in green and black contour line. Large black ellipses indicate the locations of strong spanwise interactions, and red ellipses indicate the LMRs merged from cylinder wakes.

associated with counter rotating swirl structures. By closely examining the trace of the green and black swirls, it is evident that the new LMRs are merged from the cylinder wake structures (as indicated in Figure 4.7, which is enlarged from Figure 4.6). Beyond $x/\delta\sim2$, these two LMRs maintain a relatively stable spacing of $\sim0.4\delta$ with small scale spanwise movement ($\sim0.1\delta$) before a strong interaction seen at $x/\delta\sim5.7$. In the far field, the flow structures become indistinct (similar to the upstream condition) and the organizations do not correlate well which is different from the 0.2δ case.

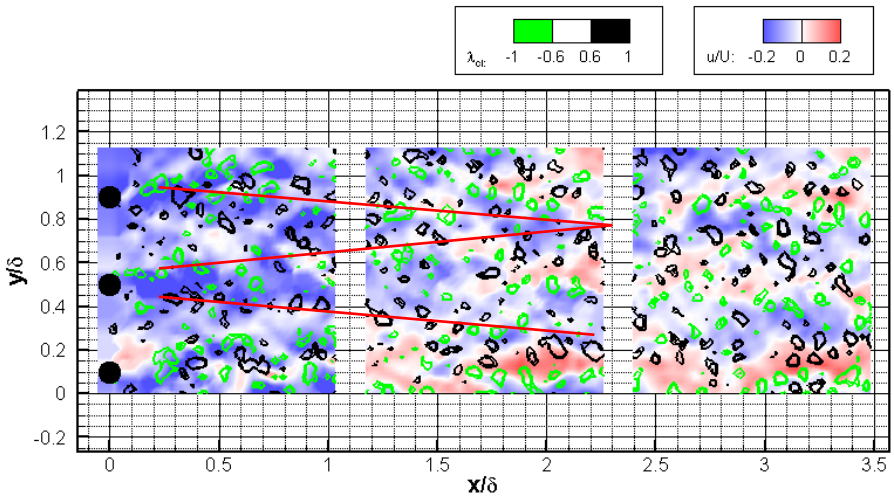

Figure 4. 7 Merging signatures observed for 0.4δ case. The development of cylinder wakes are marked by red lines.

From the wall-normal component, downwash can be seen directly behind each cylinder, and the location coincides with that where higher streamwise velocity is present. In this case, since the downwash lasts longer than that in the 0.2δ case, it continuously brings faster moving fluid to the measurement height. In consideration of continuity, the slow moving cylinder wakes are expected to move aside towards the mid-spacing location.

In Figure 4.8, two LMRs are present in the incoming flow hitting the mid-spacing location. In this case, the wake of the middle cylinder is attracted towards the mid-spacing location immediately by the lower LMR and then meander throughout the measurement field. The spanwise spacing between the LMRs is approximately 0.8δ (two times the cylinder spacing of 0.4δ) because the top two cylinder wakes are not moving towards the same direction. The wall normal component does not seem to dominate the overall behavior because the upstream LMRs interact with the cylinder wake immediately downstream of the array.

Figure 4.9 represents the case where the incoming LMR approaches the cylinder directly. Immediately downstream of the cylinder array, the LMR overlaps the cylinder wake, and remains strongly coherent throughout the measurement field. Directly behind the cylinder, some possible

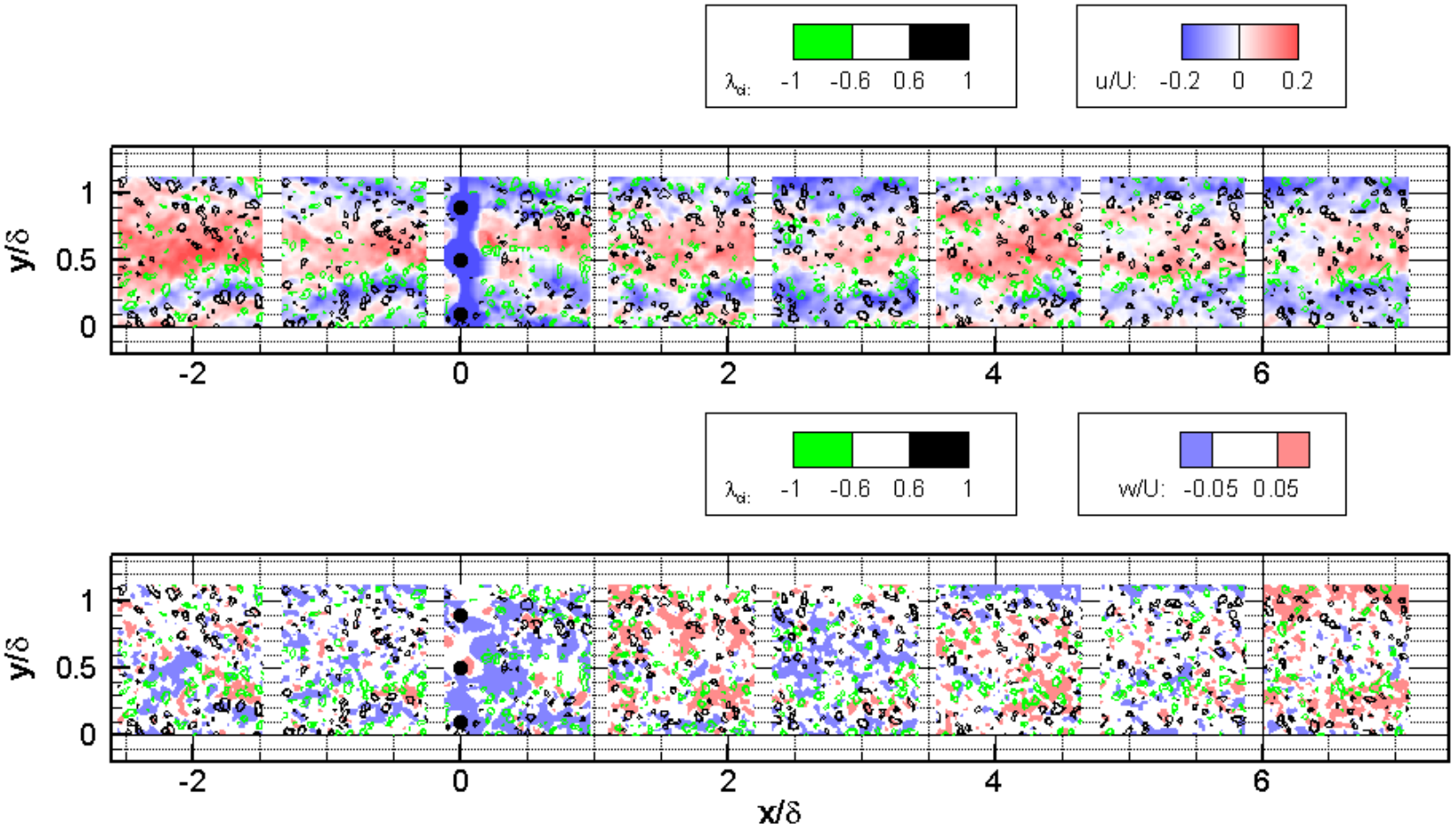

Figure 4.8 A single run of F8D case; streamwise and wall normal velocities are shown in blue and red contours; 2d swirling strength is shown in green and black contour lines.

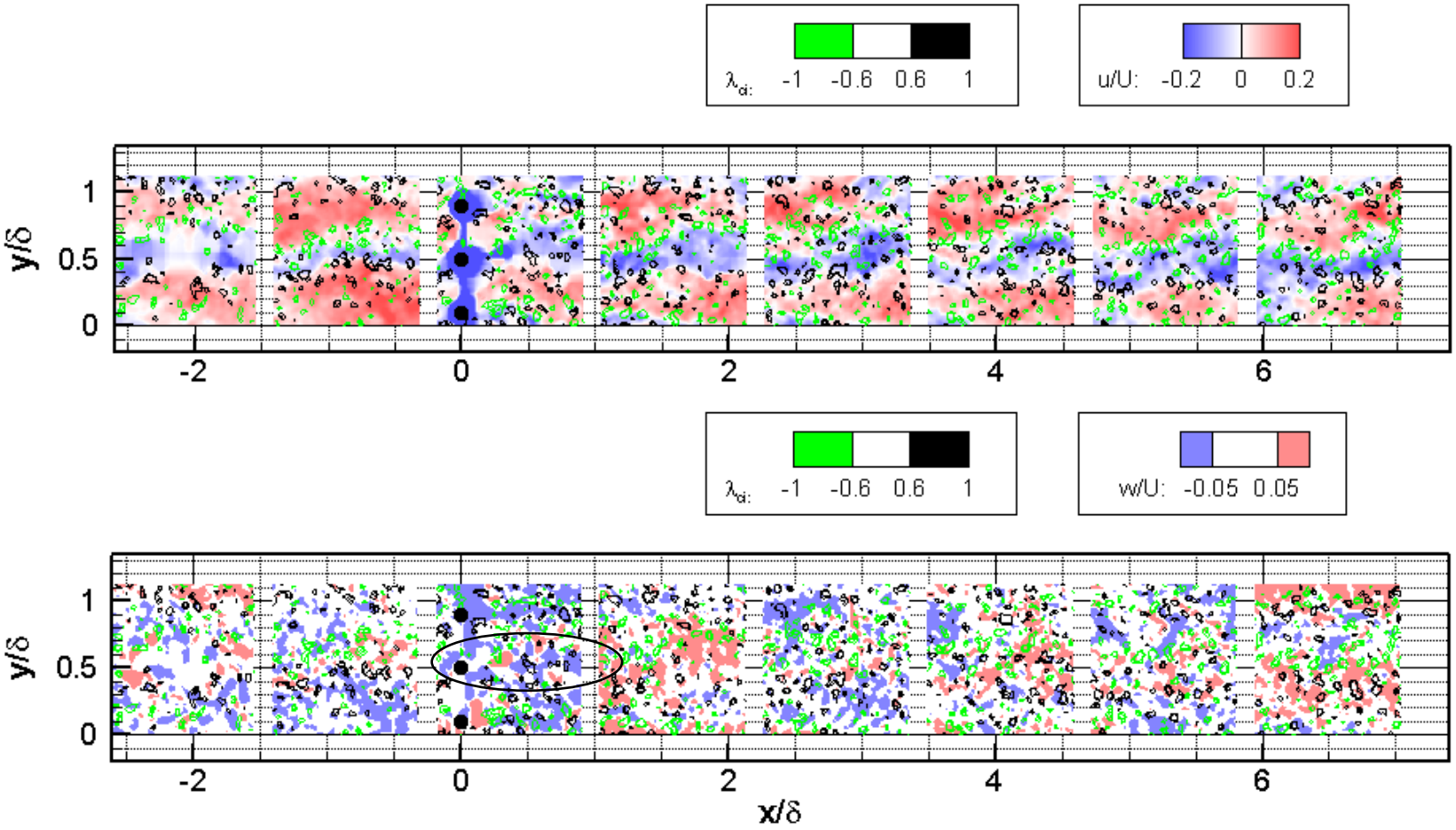

Figure 4.9 A single run of F8D case; streamwise and wall normal velocities are shown in blue and red contours; 2d swirling strength is shown in green and black contour lines. The downwash direct behind the middle cylinder is marked by the large black ellipse.

downwash behavior is observed (as marked by the large black ellipse), and it is associated with the higher streamwise velocity. This can be possibly used to explain the disorientation of the cylinder wake and the consequent spanwise movement towards the negative spanwise direction in the order of $\sim 0.1\delta$. Further, at the top of the first two fields, a streak of black swirl contours lines and some slow moving fluid is observed, suggesting another LMR just outside the field. The spacing between the two LMRs is therefore estimated $\sim 0.6\delta$. This situation is comparable to Figure 4.8 where the slow moving region comes at the mid-spacing location. After the cylinder array, the wake of the top cylinder is tilted towards positive y direction and the black swirls are aligned with those of the incoming LMR. These black swirls remain coherent at the same spanwise location throughout the measurement field.

By examining the other runs in this data set, the data can be roughly grouped into three types of scenarios. First, if the incoming flow does not have distinct low momentum structures, it is likely that the cylinder wakes maintain a strong periodicity within $x/\delta \sim 0.5$, and the downwash behavior plays a dominant role in the wake structure development in terms of its tilting direction. In this scenario, the spanwise spacing of the LMRs is frequently $\sim 0.4\delta$ after the merging of cylinder wakes at the mid-spacing location around $x/\delta \sim 2$ and then reverts to a similar status of the incoming flow in the far field after $x/\delta \sim 6$. The mechanism for this scenario is illustrated in Figure 4.10.

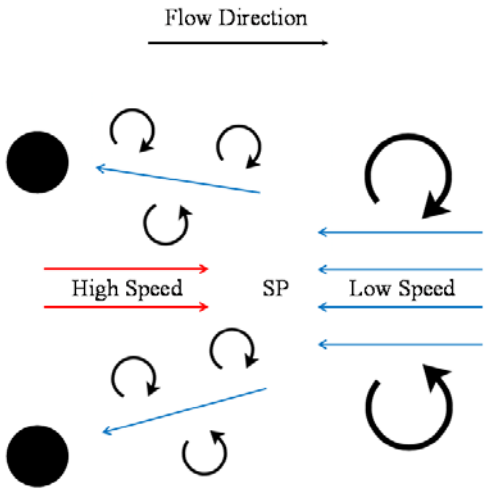

Figure 4. 10 Idealized mechanism for wake merging when no obvious packets are present in the incoming flow.

Second, if there are obvious low momentum structures coming at the mid-spacing location of the cylinder array, it is common that the cylinder wakes immediately interact with the upstream LMRs merging into new ones maintain at the mid-spacing location with minor spanwise movements. In this scenario, the spanwise spacing is expected approximately to be

either 0.4δ or 0.8δ, depending on the direction each individual cylinder wake is merged. Different from the first scenario, the downwash in this situation does not seem to dominate the behavior of the downstream LMRs as they are strongly coherent with the incoming flow structure. The mechanism for this scenario is illustrated in Figure 4.11.

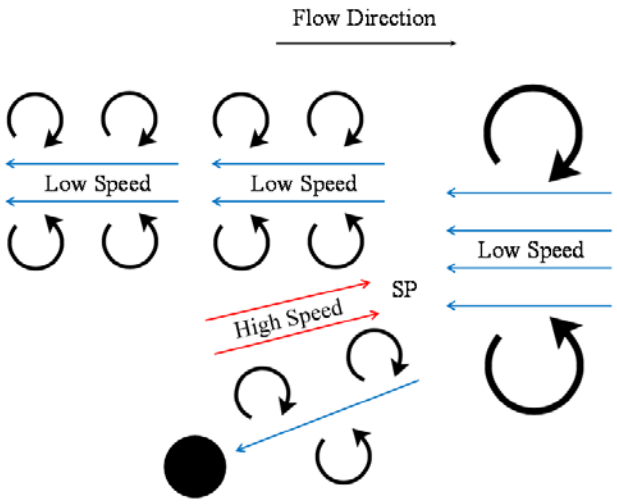

Figure 4. 11 Idealized mechanism for wake packet interaction when the packet in the incoming flow is hitting the mid-spacing location.

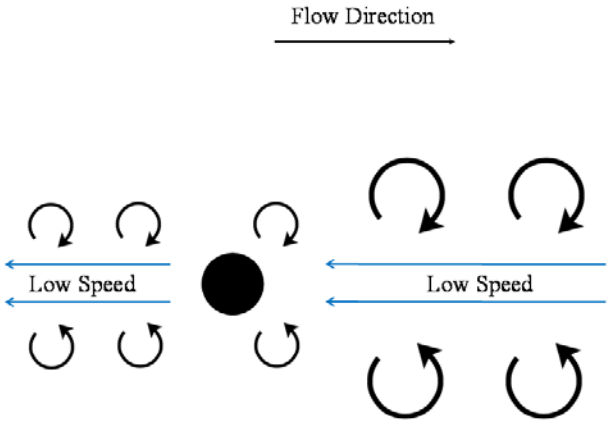

Figure 4. 12 Idealized mechanism for wake packet interaction when the packet in the incoming flow is hitting the cylinder.

Finally, if these low momentum structures in the upstream flow are hitting the cylinder directly, the LMRs will carry on after the cylinder array with small scale meandering motion in the order of $\sim 0.1\delta$, as shown in Figure 4.12. Although a spanwise merging behavior is observed in some cases, it is not common for this scenario. When thinking of the incoming flow, based on

the results from Chapter 2, the most frequent dominant spanwise scale is $\sim 0.6\delta$, so for this 0.4δ spacing data set, a mix of the second scenario and third scenario is expected to be frequent, i.e. one LMR hits the cylinder and the other hits the mid-spacing location; and so is observed in Figure 4.9. Therefore, the one coming at the mid-spacing location will induce scenario two where the LMR goes through and stays relatively stable at the same location; further, the one coming at the cylinder will induce scenario three where the wake structure moves toward the mid-spacing location. Consequently, the dominant spanwise modes in $2 < x/\delta < 6$ are most likely to be $\sim 0.4\delta$ or $\sim 0.8\delta$ yet due to the span limit, $\sim 0.7\delta$ might be reported more frequently. This is consistent with Figure 3.14 where 0.4δ and 0.7δ bins remain higher than the non-perturbed case until zone 5. At $5.5 < x/\delta < 6$, when the spanwise spacing of the LMRs is 0.4δ, a spanwise interaction is highly possible as observed in Figure 4.6 and when that happens, the spanwise scale is expected to grow. Thus in the far field, the 0.4δ mode is expected to be less frequent and the larger modes, i.e. 0.7δ and 0.8δ mode, are expected more frequently. This is also supported by Figure 3.14.

4.4 0.6δ spacing case

The case for 0.6δ spacing is depicted in Figures 4.13, 4.14 and 4.15 respectively for selected runs. With larger spacing, the relative position between the incoming LMRs and cylinders are important in determining the downstream structures so the aforementioned three scenarios also apply here. Figure 4.13 represents the first scenario where no strong coherent packets are present in the incoming flow. This is identified by the rather disorganized swirling structures. In this case, the wake structures dominate the flow immediately after the cylinder array and spanwise movement is observed. Before $x/\delta \sim 2$, there is no obvious merging signature but beyond this point, a spanwise interaction is indicated by the mixing of two pairs of counter rotating swirl structures. At $x/\delta \sim 3$, a distinct LMR (marked by large red ellipse) is formed at the mid-spacing location through merging (as marked by the red lines) and remains in the same location throughout the measurement field. By looking at the wall-normal velocity field, two downwash signatures are observed directly behind the cylinders (marked by large black ellipses) and they correspond to the high streamwise velocity region. Therefore, in this scenario, the downwash seems to be critical for the movement of cylinder wake structures and this is consistent with the previous case. Note that at the top of the fields beyond $x/\delta \sim 3$, there is another obvious LMR formed at $y/\delta \sim 1$ which is approximately a mid-spacing location; thus the spanwise spacing between the two LMRs is $\sim 0.6\delta$. These two LMRs are associated with counter rotating swirls but not with positive wall-normal velocities, therefore it is unlikely that the LMRs here are related to coherent vortex packets and consequently these structures are not

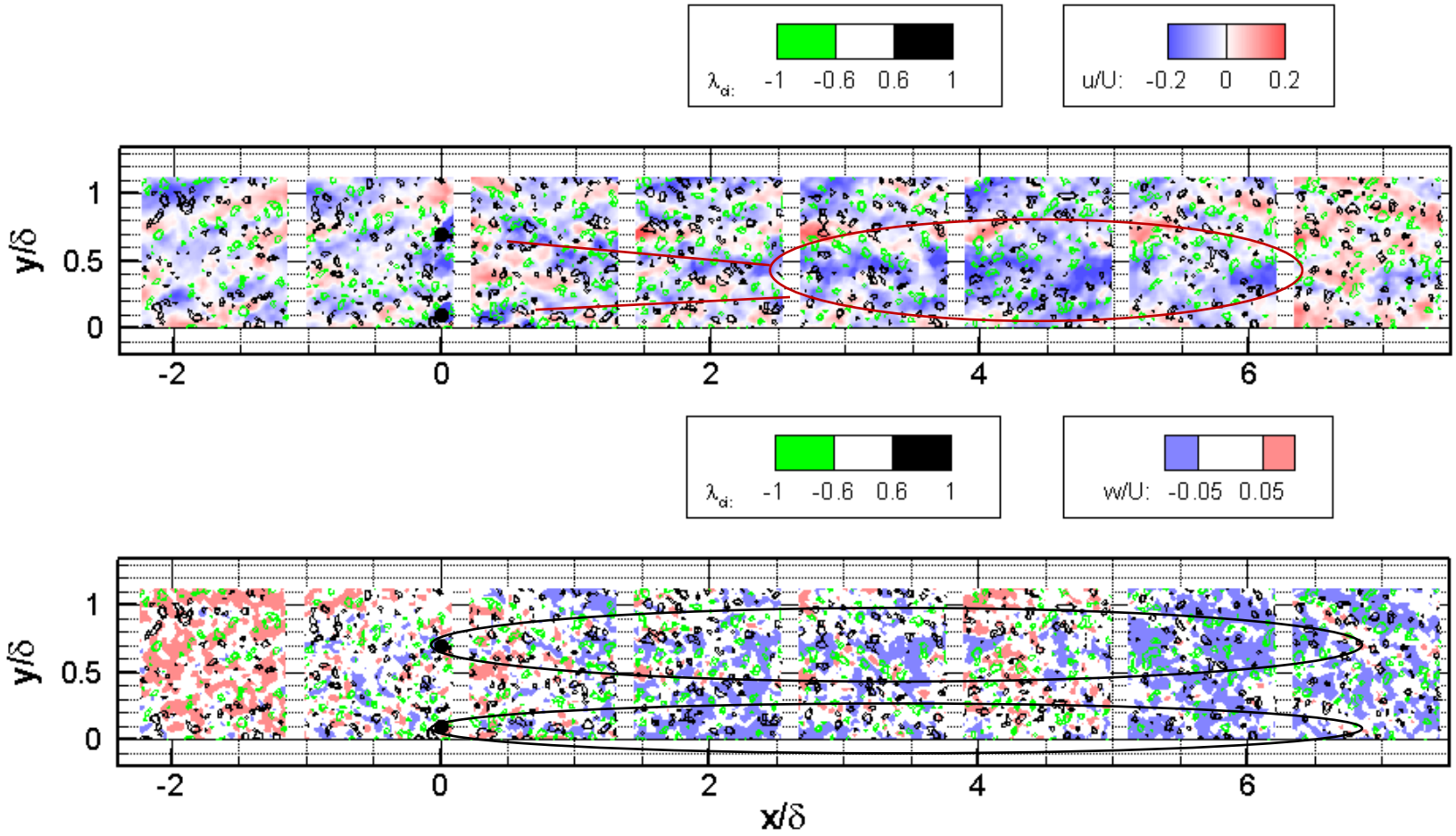

Figure 4.13 A single run of F12D case; streamwise and wall normal velocities are shown in blue and red contours; 2d swirling strength is shown in green and black contour lines. Red lines indicate the spanwise movement of cylinder wakes, and the LMR at mid-spacing location is marked by the red ellipse. The large black ellipses indicate the downwash observed in the wall normal component.

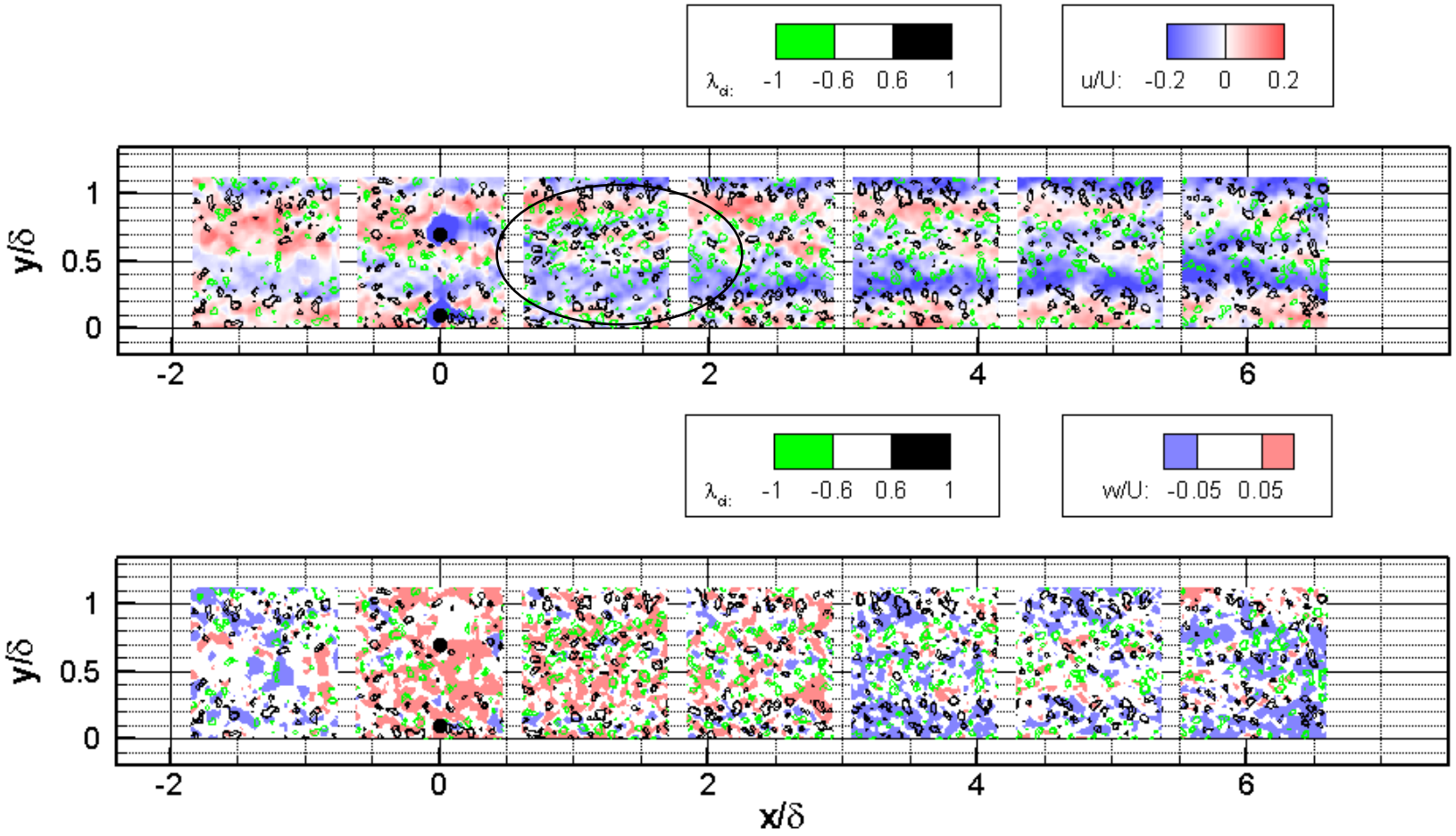

Figure 4.14 A single run of F12D case; streamwise and wall normal velocities are shown in blue and red contours; 2d swirling strength is shown in green and black contour lines. The black ellipse indicates the location where the cylinder wake is merged into the packet from the incoming flow.

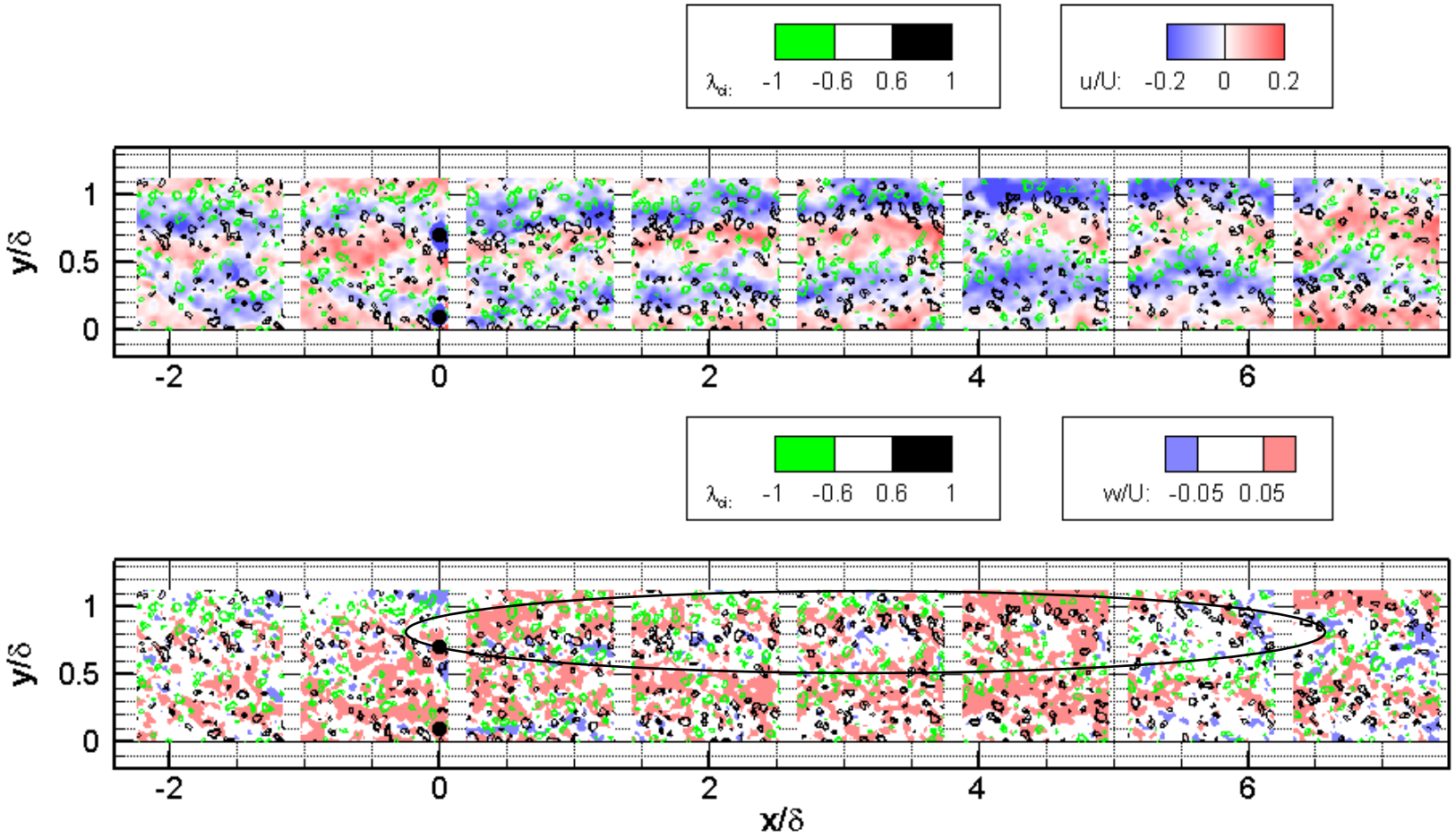

Figure 4.15 A single run of F12D case; streamwise and wall normal velocities are shown in blue and red contours; 2d swirling strength is shown in green and black contour lines. The large black ellipse indicates the downwash observed in the wall normal component.

expected to last long; in fact, these two LMRs become less dominant in the far field. Based on this discussion, the probability of 0.6δ mode in the far field should be lower compared to previous zones and this is in good agreement with Figure 3.17.

Figure 4.14 corresponds to scenario two where the vortex packet is hitting the mid-spacing location. So the cylinder wakes interact with the packet immediately after the array at roughly $x/\delta \sim 0.5$ which is confirmed by the mixing of the swirling structures (marked by black ellipse). Beyond this location, these low momentum structures settle at the mid-spacing location and remain coherent throughout the measurement fields without further strong spanwise interaction. Also, by looking at the wall-normal component, it is evident that these LMRs are well associated with positive normal velocities so it is clear that these structures are induced by vortex packets and therefore coherent.

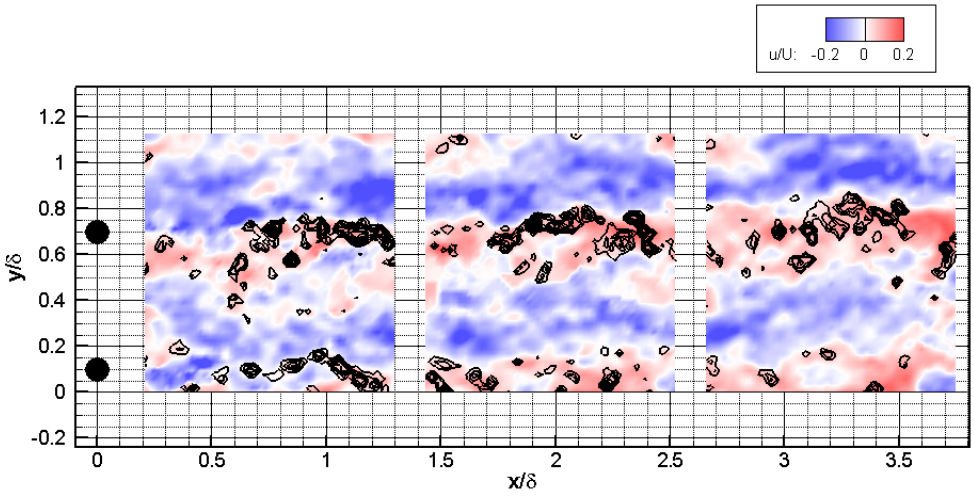

Figure 4. 16 Reynolds stress for faster streamwise velocity and negative wall normal velocity with threshold of $0.63u_{RMS}w_{RMS} \sim 3.15u_{RMS}w_{RMS}$

Finally, Figure 4.15 gives the third scenario where the packets are hitting directly at the cylinders. Though the location is slightly off, the opposite movement of green and black swirl structures just upstream of the cylinders still suggests that the vortex packet is obstructed by the cylinders. After the cylinder array, two wake structures are strong and distinct. No spanwise interaction is observed and they move continuously toward the mid-spacing location. The spanwise spacing between them is well sustained at $\sim 0.6\delta$. By looking at the wall-normal component, a streak of downward velocity is observed directly after the cylinder (as marked by the large black ellipse) and then it moves toward the mid-spacing location. In terms of the position, it overlaps with the black swirls suggesting that they are just beside the low momentum structures. This is consistent with previous conclusion and in this case the downwash seems to be

the reason of the spanwise movement of the structure. Figure 4.16 gives further proof by plotting the Reynolds stress for faster streamwise component and negative wall normal component of the same fields from Figure 4.15. The high Reynolds stress regions are always observed on the side of the LMRs.

By closely examining the other runs in this data set, it can be concluded that the three scenarios discussed before also apply here but with less spanwise movement in all occasions. When the incoming flow is rather uniform, the wake structures move toward the mid-spacing location and the direction is associated with the downwash of wall-normal velocity. In this case, the low momentum structures become less dominant as they move to the far field at $x/\delta \sim 6$. This explains the drop of $\sim 0.6\delta$ mode from zone 5 to zone 8. When the packets in the incoming flow are hitting the mid-spacing location, the wake structures are merged immediately and the new LMRs remain at the same location without obvious spanwise movement. Consequently, the dominant spanwise spacing is expected to be $\sim 0.6\delta$. Finally, when the packets are hitting the cylinder, they are carried on by the cylinder wake and then move toward the mid-spacing location without spanwise interaction. Note that in this case, the direction of movement is highly associated with the wall-normal velocity, so it is equally possible that the wake structures move toward the same spanwise direction verses the opposite direction. This will lead to different dominant spanwise spacing to $\sim 0.6\delta$ and $\sim 1.2\delta$ respectively so these two modes are expected to be more frequent than the non-perturbed case, which is true according to Figure 3.17. Since the dominant natural spanwise mode is $\sim 0.6\delta$, this mode is expected to be enhanced by considering the second and third scenarios.

Chapter 5

Summary and Recommendations for Future Work

The objective of the current study was to manipulate the coherent vortex packets in a turbulent boundary layer by inserting a small scale cylinder array of different spacing with height $H/\delta = 0.2$ and to study the stability of the downstream flows. Both fixed location data and flying data were acquired, and a major effort was made to study the spanwise scales of the packets and wake structures downstream of the cylinder array.

5.1 Summary

For the non-perturbed flow, long streamwise low-momentum regions (LMRs) were observed at measurement height $z^+ = 296$ associated with counter-rotating swirl structures on each side indicating the existence of coherent vortex packets. These packets were found to persist over a streamwise distance of $\sim 8\delta$, and their spanwise location was random, leading to a uniform averaged field. The spanwise spacing of the packets varied but the 0.6δ mode was dominant which was consistent with previous study by Hutchins et al., (2005). From the flying data, some spanwise interactions of the packets were observed but the process was mild and it happened over a large time scale. One important observation was that, for a single run, the packets within the field of view were often associated with some random distortion, and rather than meandering in the spanwise direction, the distortion of the packet was preserved as it evolved downstream. Similar behavior was also observed in all perturbed cases.

The coherent packets were altered by inserting the cylinder array. Three cases with different cylinder spacing were studied: 0.2δ, 0.4δ and 0.6δ. From the averaged streamwise velocity field for all three cases, clear patterns of spanwise variation was observed in the flow downstream of the cylinders such that low speed regions were observed to shift to the mid-spacing locations. For the 0.2δ case, these low speed regions were formed at $x/\delta \sim 0.5$ and remained parallel to the neighboring regions until $x/\delta \sim 2$. These regions started to disappear after $x/\delta \sim 2$ and the entire field reverted to the non-perturbed condition in the far field at

$x/\delta\sim7$. For the 0.4δ case, these low speed regions in the mid-spacing location were formed further downstream at $x/\delta\sim2$ and remained organized, although the amplitude of the spanwise variation was reduced in the far field at $x/\delta\sim7$. For the 0.6δ case, these regions were formed at $x/\delta\sim3$ and remained distinct at $x/\delta\sim7$, indicating that this organization was the most stable one of the three perturbed cases. Also, downwash behaviors were observed in the averaged wall-normal velocity field. Regions of downwash appeared directly behind each cylinder and retained the same spanwise location. The difference was that for the 0.2δ case, clear downwash patterns disappeared at $x/\delta\sim1.5$, while the same patterns lasted until $x/\delta\sim4$ in the 0.4δ case. In the 0.6δ case, these downwash regions lasted throughout the measurement field and continuously brought faster moving fluid toward the measurement plane which explained the spanwise variation of streamwise velocity observed in the far field at $x/\delta\sim7$ for the 0.6δ case.

In the flying data sets, different runs for each case were examined. For the 0.2δ case, the incoming flow was greatly obstructed and the streamwise velocity was significantly decreased immediately downstream of the cylinder array. Also, more vortical structures were introduced, as judged by the increased population of the swirls compared with that in the incoming flow. The downstream flow structures were much disorganized within $x/\delta\sim0.5$, thus the spanwise velocity became more significant and strong spanwise interactions were observed in this range. Combined with the spanwise mode analysis, splitting motions were believed to be present within $x/\delta\sim0.5$, and then these structures reorganized themselves through merging and pairing motions from $x/\delta\sim0.5$ to $x/\delta\sim2$. The final organization of the downstream LMRs beyond $x/\delta\sim3$ were well correlated with the incoming flow condition judged by the location and number of the low-momentum regions in the flying data, which explained why the averaged field reverted to non-perturbed condition. Consequently, the downstream flow was not stable due to its dependence on the incoming flow. In this case, strong spanwise motions dominated the flow immediately downstream of the cylinder array and therefore the downwash effect was less important in affecting the behaviors of the cylinder wakes.

For the 0.4δ case, the behavior of the wake structures was highly variable, but based on the relative spanwise location of the packets in the incoming flow, the behavior was grouped into three types of scenarios, namely, relatively uniform incoming flow, packets in the mid-spacing location and packets hitting the cylinders. For the first scenario, there were no obvious coherent structures in the incoming flow, and the wake structures remained distinct immediately after the cylinder array. Unlike the 0.2δ case, no obvious spanwise interactions were observed in this 0.4δ case. The spanwise motions further downstream at $x/\delta\sim2$ appeared to be caused by the downwash effect which brought faster moving fluid to the measurement plane and forced the slow moving wake structures to move laterally toward the mid-spacing location. In the far field at $x/\delta>6$, some structures became unstable and interacted with neighboring ones. In the second

scenario, the packets passed through the way at the mid-spacing locations and remained coherent. These packets interacted immediately with the neighboring cylinder wakes and the wake structures merged into the existing packets in the mid-spacing location. In the third scenario, packets hitting the cylinder were enhanced by the cylinder wake structure and remained strongly coherent in the downstream with a tendency to move to the mid-spacing location what was induced by the downwash.

Due to the natural spanwise spacing of the packets, combinations of the second and third scenario were most frequent; and since the downstream structures tended to move toward the mid-spacing location in both cases, the stability of the downstream structures was enhanced.

The 0.6δ case was important and interesting as the spanwise mode introduced by the cylinder array was the same as the natural spanwise spacing. The downstream flow behaviors were also grouped into the three scenarios mentioned above, and for each scenario, the behavior of the packets and LMRs were analogous. The most important difference was that, by considering the natural dominant spanwise mode, the relative location of spanwise neighboring packets to the cylinders would be the same so that the downstream development of the packets and/or LMRs was in phase, and consequently the structures were more organized as opposed to the 0.4δ case where the second and third scenarios occurred more often in combinations such that the development of neighboring LMRs was out of phase, leading to a less stable organization. Finally, it can be concluded that the perturbation introduced with the same spanwise mode of the non-perturbed flow enhanced the dominant natural spanwise mode. The organization of LMRs (or packets) was most stable in this case.

5.2 Future work

From the current data, it is obvious that the wall-normal component in the flying data sets is still somewhat noisy, most likely due to the vibration of the moving traverse in flying experiments. Thus the experimental set up might be improved in the future by redesigning the connection of the interface box and the traverse. Also, flying experiments could be potentially fully automated to acquire more runs for each case. Further, all of the current measurements were performed at $z^+ = 296$, yet the downstream structures of the cylinder array were highly three-dimensional. Therefore, measurements at different heights would be desirable to further understand the flow structure. Volumetric measurement techniques could be helpful if applied to the study.

Following the previous discussions, it would be useful to complete the data set with a cylinder array of larger spanwise spacing ($> 0.6\delta$) to confirm that the 0.6δ perturbation matching the dominant natural mode induced results in optimal packets stabilization. Also, the

downstream wakes and LMRs were proved to be affected by the downwash generated from the cylinder tips, and previous studies showed that the downstream flow structures are dependent on the cylinder height; however, the cylinder height in the current study was limited to $H/\delta = 0.2$. Therefore, it would be interesting to use cylinder arrays with different height to study whether an optimal height is present where the downwash/upwash recirculation and the vortex shedding are balanced resulting in a most stabilized downstream flow organization. A thorough understanding of these effects can lead to practical applications in different flows with proper scaling and consequently become beneficial for real world engineering cases.

Bibliography

Adrian, R. J. (2007), "Hairpin Vortex Organization in Wall Turbulence," *Physics of Fluids*, 19.

Adrian, R. J., and Liu, Z. C. (2002), "Observation of Vortex Packets in Direct Numerical Simulation of Fully Turbulent Channel Flow," *JOURNAL OF VISUALIZATION*, 5, 9-19.

Adrian, R. J., Meinhart, C. D., and Tomkins, C. D. (2000), "Vortex Organization in the Outer Region of the Turbulent Boundary Layer," *Journal of Fluid Mechanics*, 422, 1-54.

Baker, C. J. (1980), "The Turbulent Horseshoe Vortex," *Journal of Wind Engineering and Industrial Aerodynamics*, 6, 9-23.

Balakumar, B. J., and Adrian, R. J. (2007), "Large- and Very-Large-Scale Motions in Channel and Boundary-Layer Flows," *Phil. Trans. R. Soc. A*, 365, 665-681.

Christensen, K. T., and Adrian, R. J. (2001), "Statistical Evidence of Hairpin Vortex Packets in Wall Turbulence," *Journal of Fluid Mechanics*, 431, 433-443.

Corke, T. C., Guezennec, Y., and Nagib, H. M. (1981), "Modification in Drag of Turbulent Boundary Layers Resulting from Manipulation of Large-Scale Structures," *NASA CR-3444*.

Dennis, D. J. C., and Nickels, T. B. (2011a), "Experimental Measurement of Large-Scale Three-Dimensional Structures in a Turbulent Boundary Layer. Part 1. Vortex Packets," *Journal of Fluid Mechanics*, 673, 180-217.

Dennis, D. J. C., and Nickels, T. B. (2011b), "Experimental Measurement of Large-Scale Three-Dimensional Structures in a Turbulent Boundary Layer. Part 2. Long Structures," *Journal of Fluid Mechanics*, 673, 218-244.

Dillon-Gibbons, C. J., Wong, C. Y., Chen, L., and Soria, J. (2007), "Cylinder Wake - Boundary Layer Interaction in the near Field," *16th Australasian Fluid Mechanics Conference*, 1475-1480.

Doorne, C. W. H. v. (2003), "Stereoscopic Piv and Visualisations on Transition in Pipe Flow," *PhD Thesis, Delft University of Technology*.

Elsinga, G. E., Adrian, R. J., van Oudheusden, B. W., and Scarano, F. (2010), "Three-Dimensional Vortex Organization in a High-Reynolds-Number Supersonic Turbulent Boundary Layer," *Journal of Fluid Mechanics*, 644, 35-60.

Elsinga, G. E., Kuik, D. J., van Oudheusden, B. W., and Scarano, F. (2007), "Investigation of the Three-Dimensional Coherent Structures in a Turbulent Boundary Layer with Tomographic-Piv," *45th AIAA Aerospace Sciences Meeting and Exhibit*.

Ganapathisubramani, B., Longmire, E. K., and Marusic, I. (2003), "Characteristics of Vortex Packets in Turbulent Boundary Layers," *Journal of Fluid Mechanics*, 478, 35-46.

Gao, Q. (2011), "Evolution of Eddies and Packets in Turbulent Boundary Layers," *PhD Thesis, University of Minnesota Twin Cities*.

Head, M. R., and Bandyopadhyay, P. (1981), "New Aspects of Turbulent Boundary Layer Structure," *Journal of Fluid Mechanics*, 107, 297-338.

Hoyas, S., and Jimenez, J. (2006), "Scaling of the Velocity Fluctuations in Turbulent Channels up to Re-Tau=2003," *Physics of Fluids*, 18.

Hutchins, N., Ganapathisubramani, B., and Marusic, I. (2005), "Spanwise Periodicity and the Existence of Very Large Scale Coherence in Turbulent Boundary Layers," *Proc. Turbulence and Shear Flow Phenomena IV*.

Hutchins, N., and Marusic, I. (2007), "Evidence of Very Long Meandering Features in the Logarithmic Region of Turbulent Boundary Layers," *Journal of Fluid Mechanics*, 579, 1-28.

Jacobi, I., and McKeon, B. J. (2011), "New Perspectives on the Impulsive Roughness-Perturbation of a Turbulent Boundary Layer," *Journal of Fluid Mechanics*, 677, 179-203.

Jimenez, J. (1998), "The Largest Scales of Turbulent Wall Flows," *Center for Turbulence Research Annual Research Briefs*, 137-154.

Kim, K. C., and Adrian, R. J. (1999), "Very Large-Scale Motion in the Outer Layer," *Physics of Fluids*, 11, 417-422.

Lee, J. H., and Sung, H. J. (2011), "Very-Large-Scale Motions in a Turbulent Boundary Layer," *Journal of Fluid Mechanics*, 673, 80-120.

Marusic, I., and Hutchins, N. (2005), "Experimental Study of Wall Turbulence: Implications for

Control," *Transition and Turbulence Control*, 207-246.

Marusic, I., and Hutchins, N. (2007), "Study of the Log-Layer Structure in Wall Turbulence over a Very Large Range of Reynolds Number," *Flow Turbulence and Combustion*, 81, 115-130.

Ortiz-Dueńas, C., Ryan, M. D., and Longmire, E. K. (2011), "Modification of Turbulent Boundary Layer Structure Using Immersed Wall-Mounted Cylinders," *Proc. Turbulence and Shear Flow Phenomena VII*.

Park, C. W., and Lee, S. J. (2002), "Flow Structure around a Finite Circular Cylinder Embedded in Various Atmospheric Boundary Layers," *Fluid Dynamics Research*, 30, 197-215.

Park, C. W., and Lee, S. J. (2003), "Flow Structure around Two Finite Circular Cylinders Located in an Atmospheric Boundary Layer: Side-by-Side Arrangement," *Journal of Fluids and Structures*, 17, 1043-1058.

Pujals, G., Cossu, C., and Depardon, S. (2010), "Forcing Large-Scale Coherent Streaks in a Zero-Pressure-Gradient Turbulent Boundary Layer," *Journal of Turbulence*, 11, 1-13.

Robinson, S. K. (1991a), "Coherent Motions in the Turbulent Boundary-Layer," *Annual Review of Fluid Mechanics*, 23, 601-639.

Robinson, S. K. (1991b), "The Kinematics of Turbulent Boundary Layer Structure," *NASA Technical Memorandum 103859*.

Ryan, M. D. (2011), "Planar and Volumetric Measurements Downstream of Cylinders Immersed in a Turbulent Boundary Layer," *Master Report, University of Minnesota Twin Cities*.

Ryan, M. D., Ortiz-Duenas, C., and Longmire, E. K. (2011), "Effects of Simple Wall-Mounted Cylinder Arrangements on a Turbulent Boundary Layer," *Aiaa Journal*, 49, 2210-2220.

Schofield, W. H., and Logan, E. (1988), "Viscous Flow around Two and Three Dimensional Wall Mounted Obstacles," *AIAA, ASME, SIAM, and APS, National Fluid Dynamics Congress, 1st*, 1742-1748.

Simpson, R. L. (2001), "Junction Flows," *Annual Review of Fluid Mechanics*, 33, 415-443.

Sumner, D., Heseltine, J. L., and Dansereau, O. J. P. (2004), "Wake Structure of a Finite Circular Cylinder of Small Aspect Ratio," *Experiments in Fluids*, 37, 720-730.

Theodorsen, T. (1952), "Mechanism of Turbulence," *Proc. Second Midwestern Conf. of Fluid Mechanics*.

Tomkins, C. D. (2001), "The Structure of Turbulence over Smooth and Rough Walls," *PhD Thesis, University of Illinois at Urbana-Champaign*.

Tomkins, C. D., and Adrian, R. J. (2003), "Spanwise Structure and Scale Growth in Turbulent Boundary Layers," *Journal of Fluid Mechanics*, 490, 37-74.

Wark, C. E., Naguib, A. M., and Nagib, H. M. (1990), "Effect of Plate Manipulators on Coherent Structures in a Turbulent Boundary-Layer," *Aiaa Journal*, 28, 1877-1884.

Westerweel, J., Dabiri, D., and Gharib, M. (1997), "The Effect of a Discrete Window Offset on the Accuracy of Cross-Correlation Analysis of Digital Piv Recordings," *Experiments in Fluids*, 23, 20-28.

Wieneke, B. (2005), "Stereo-Piv Using Self-Calibration on Particle Images," *Experiments in Fluids*, 39, 267-280.

Williamson, C. H. K. (1996), "Vortex Dynamics in the Cylinder Wake," *Annual Review of Fluid Mechanics*, 28, 477-539.

Zhou, J., Adrian, R. J., Balachandar, S., and Kendall, T. M. (1999), "Mechanisms for Generating Coherent Packets of Hairpin Vortices in Channel Flow," *Journal of Fluid Mechanics*, 387, 353-396.